ABSTRACT

Title of Document:	ANALYSES OF ADVANCED CONCEPTS IN MULTI-STAGE GYRO-AMPLIFIERS AND STARTUP IN HIGH POWER GYRO-OSCILLATORS.
	Oleksandr V. Sinitsyn, Doctor of Philosophy, 2005
Directed By:	Professor V. L. Granatstein, Department of Electrical and Computer Engineering

Gyrotrons are well recognized sources of high-power coherent electromagnetic radiation. The power that gyrotrons can radiate in the millimeter- and submillimeter-wavelength regions exceeds the power of classical microwave tubes by many orders of magnitude. In this work, the author considers some problems related to the operation of gyro-devices and methods of their solution. In particular, the self-excitation conditions for parasitic backward waves and effect of distributed losses on the small-signal gain of gyro-TWTs are analyzed. The corresponding small-signal theory describing two-stage gyro-traveling-wave tubes (gyro-TWTs) with the first stage having distributed losses is presented. The theory is illustrated by using it for the description of operation of a Ka-band gyro-TWT designed at the Naval Research Laboratory. Also, the results of nonlinear studies of this tube are presented and compared with the ones obtained by the use of MAGY, a multi-frequency, self-consistent code developed at the University of Maryland. An attempt to build a large signal theory of gyro-TWTs with tapered geometry and magnetic field profile is made and first results are obtained for a 250 GHz gyro-TWT.

A comparative small-signal analysis of conventional four-cavity and three-stage clustered-cavity gyroklystrons is performed. The corresponding point-gap models for these devices are presented. The efficiency, gain, bandwidth and gain-bandwidth product are analyzed for each scheme. Advantages of the clustered-cavity over the conventional design are discussed.

The startup scenarios in high-power gyrotrons and the most important physical effects associated with them are considered. The work presents the results of startup simulations for a 140 GHz, MW-class gyrotron developed by Communications and Power Industries (CPI) for electron-cyclotron resonance heating (ECRH) and current drive experiments on the "Wendelstein 7-X" stellarator plasma. Also presented are the results for a 110 GHz, 1.5 MW gyrotron currently being developed at CPI. The simulations are carried out for six competing modes and with the effects of electron velocity spread and voltage depression taken into account.

Also, the slow stage of the startup in long-pulse gyrotrons is analyzed and attention is paid to the effects of ion compensation of the beam space charge, frequency deviation due to the cavity wall heating and beam current decrease due to cathode cooling. These effects are modeled with a simple nonlinear theory and the code MAGY.

ANALYSES OF ADVANCED CONCEPTS IN MULTI-STAGE GYRO-AMPLIFIERS AND STARTUP IN HIGH POWER GYRO-OSCILLATORS.

By

Oleksandr V. Sinitsyn.

Dissertation submitted to the Faculty of the Graduate School of the
University of Maryland, College Park, in partial fulfillment
of the requirements for the degree of
Doctor of Philosophy
2005

Advisory Committee:
Professor V. L. Granatstein, Chair
Doctor G. S. Nusinovich
Professor T. M. Antonsen, Jr.
Professor I. D. Mayergoyz
Professor D. Boyd

Dedication

To my dear parents.

Acknowledgments

I owe my gratitude to all the people who have helped me in preparation of this dissertation and who have made my graduate school experience one of the most special periods of my life.

First, I would like to thank my academic advisor, Professor Victor Granatstein, for giving me an invaluable opportunity to work on challenging and very interesting projects over the past five years.

Second, I owe a tremendous gratitude to my co-advisor, Dr. Gregory Nusinovich. He always made himself available for help and advice and there has never been an occasion when I have knocked on his door and he has not found time for me. It has been a pleasure to work with and learn from him.

Thanks are due to Professor Thomas Antonsen, Professor Isaak Mayergoyz and Professor Derek Boyd for agreeing to serve on my dissertation committee and for spending their time for reviewing the manuscript.

I would like to especially thank Dr. Alexander Vlasov for his help with simulation codes and his useful suggestions and discussions.

I would also like to acknowledge help and support from some of the staff members. Dorothea Brosius' help with the software is highly appreciated, as is the computer hardware support from Edward Condon and traveling help from Janice Schoonover.

I owe my deepest thanks to my family – my parents and my brother who have always stood by me and guided me through my career, and have pulled me through against all the odds. Words cannot express the gratitude I owe them.

Table of Contents

List of Figures

Introduction

Gyrodevices or gyrotrons are known as high-power sources and amplifiers of millimeter and submillimeter waves. In gyrodevices, electrons gyrating in an external magnetic field interact with electromagnetic waves (EM-waves). The power radiated by gyrotrons at these wavelengths both in continuous-wave and pulsed regimes exceeds the power of classical microwave tubes (klystrons, magnetrons, traveling-wave tubes, backward-wave oscillators, etc.) by many orders of magnitude. Such advantage of gyrodevices is based on the remarkable physics of their operation. In order to realize a coherent radiation of electrons, classical microwave tubes require microwave structures with elements smaller than the operation wavelength. For example, traveling-wave tubes and backward-wave oscillators are based on the principle of Cherenkov synchronism between electrons and slow waves, which are excited in periodic slow-wave structures and whose phase velocity is close to the electron velocity. The period of these structures should be smaller than the wavelength. The distance between electrons and walls of these structures should also be much smaller than the wavelength, because slow waves are localized near the structure walls due to their imaginary transverse wavenumbers. All these factors result in the miniaturization of the interaction space with the frequency growth. Correspondingly, the power that can be handled by such structures decreases very rapidly.

Contrary to the classical devices, electrons in gyrodevices can resonantly interact with fast waves, which, in principle, can propagate even in free space. This

means that the interaction can take place in smooth-wall metal waveguides and does not require the periodic variation of the waveguide wall that is necessary for the support of slow waves. Fast waves have real transverse wavenumbers, which means that the waves are not localized near the walls of the microwave structure. Correspondingly, the interaction space can be extended in the transverse direction, which makes the use of fast waves especially advantageous for millimeter and submillimeter wave generation, since the use of large waveguide or cavity cross sections reduces wall losses and breakdown restrictions, as well as permits the passage of larger electron beams with higher power.

A configuration of the simplest gyrotron is shown in Fig. I.1. In this figure, a magnetron-type electron gun is shown on the left. The voltage applied to the anode creates the electric field at the cathode. This field has both perpendicular and parallel
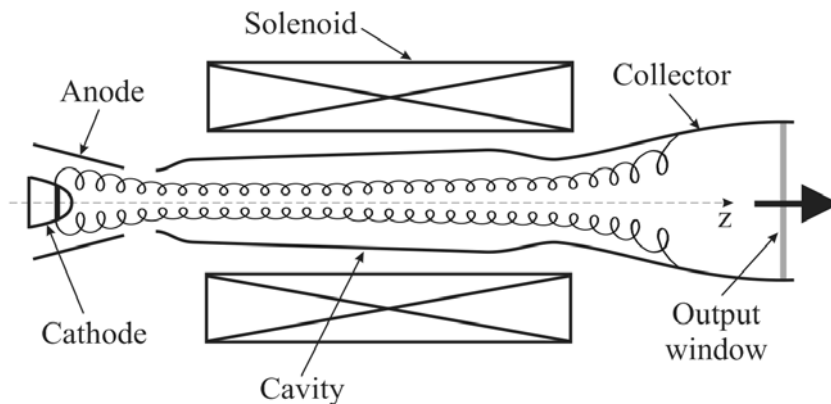
Fig. I.1. Typical gyrotron configuration.

components with respect to the lines of the magnetic field produced by solenoids. Thus, electrons emitted from the cathode acquire both orbital and axial velocity components. Then, the electrons move toward the cavity in the growing magnetic field, in which the electron flow undergoes the adiabatic compression and the orbital

momentum increases. In the region of the uniform magnetic field, the electrons interact with the eigen-mode of the resonator and transform part of their kinetic energy into the microwave energy. Then, the spent beam exits the cavity, undergoes decompression in the decreasing magnetic field and settles on the collector. The latter also functions as an oversized output waveguide, which directs the outgoing radiation toward the output window shown on the right.

The coherent cyclotron radiation in gyrotrons is caused by the cyclotron maser instability. This instability was discovered in the late 1950s by several scientists working independently [1]-[4]. Then, in the 1960s, it was experimentally verified in a number of studies [5]-[8]. In the early 1970's, electron cyclotron maser experiments driven by intense relativistic electron beams were reported [9]-[11]. However, a practical gyrotron oscillator configuration was invented and developed in the U.S.S.R. [12]. Some details of the Soviet gyrotron program of that period can be found in Refs. [13]-[17]. The first U.S. gyrotron oscillator was developed at the Naval Research Laboratory (NRL) [18]. Since then, gyrodevices have dominated the millimeter-wave region at the megawatt power level and successfully entered the submillimeter wavelengths. They can be used in numerous scientific, military and industrial applications such as plasma heating and diagnostics in controlled fusion reactors, material processing and radar systems. The growth of satellite-based digital communications technology also opens great opportunities for these devices.

The development of gyro-devices has been supported by extensive theoretical research. The linear theory of the interaction between electromagnetic waves and electrons either rotating in an external homogeneous magnetic field or moving along

trochoidal trajectories in crossed external electric and magnetic fields was developed by Gaponov in 1961 [19]. The nonlinear theory of interaction at arbitrary cyclotron harmonics between electrons moving periodically with a constant axial velocity and an electromagnetic wave was published by Yulpatov in 1967 [20] (see also Ref. 8). Since these publications were almost unknown to the Western community, the theory of gyro-travelling-wave tubes (gyro-TWTs) operating at the fundamental and higher cyclotron harmonics was renewed at the end of 1970's by Chu et al [21],[22]. Later, a rather general approach to the nonlinear theory of gyro-TWTs was made by Ginzburg et al [23]. A generalization of this theory to the case of interaction of the electron beam with electromagnetic waves propagating in waveguides was given by Fliflet [24]. A single comprehensive monograph on gyrotrons addressed to a general audience was presented recently by Nusinovich [25]. Also, during the last decade, various numerical codes appeared, which are widely used for the analysis and design of gyro-devices. One of the most powerful tools of nowadays is the self-consistent, multifrequency code MAGY [26] developed at the University of Maryland and the Naval Research Laboratory (NRL). Advances in the code development are reviewed in [27].

During the extensive experimental and theoretical studies, various types of gyrodevices emerged. They can be divided into two groups, oscillators and amplifiers, each consisting of several configurations. The key members of this large family and their classical linear beam counterparts are shown in Fig. I.2. The most well-known gyrotron oscillators are gyromonotrons and gyro-backward-wave oscillators (gyro-BWOs). Gyroklystrons (GKLs), gyro-traveling-wave tubes (gyro-
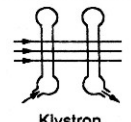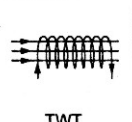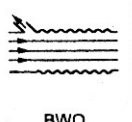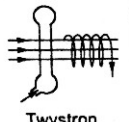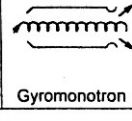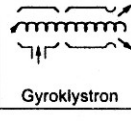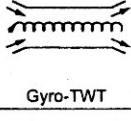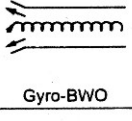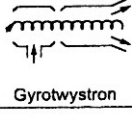
Linear Beam Device	Monotron	Klystron	TWT	BWO	Twystron
Type of Gyrotron	Gyromonotron	Gyroklystron	Gyro-TWT	Gyro-BWO	Gyrotwystron

Fig. I.2. Schematics of linear beam devices and corresponding gyrodevices.

TWTs) and gyrotwystrons form the group of gyrotron amplifiers. More detailed layouts of the devices considered in this work will be shown in the corresponding sections of the manuscript.

For a long period of time gyroklystrons were considered to be the major type of gyroamplifiers. They are capable of high-gain and high-efficiency operation, however they possess a rather narrow bandwidth, which can be a critical factor in communication systems and Doppler radars. High-gain gyro-TWTs can offer much larger bandwidth but their operation can be prone to parasitic self-excitation of various kinds. In particular, a parasitic excitation of backward waves can occur in gyro-TWTs with a long interaction region [28]-[30].

There exist various means for solving these problems and improving the performance of the gyroamplifiers. The stability problem in gyro-TWTs can be solved in at least two ways. The first one is to introduce distributed losses in one or several stages of the device [29]-[31]. The presence of losses deteriorates the start oscillation conditions and, hence, the stable operation can be achieved. The second way is to use multi-stage devices, in which interaction sections are separated by drift regions where the wave propagation is impossible. The stability of such

configurations can be achieved by decreasing the length of each stage, i.e. making it shorter than is necessary for the backward wave excitation.

The bandwidth of narrow-band GKLs can be significantly increased by detuning of cavities' eigenfrequencies, which is referred in the literature as stagger tuning [32]-[34]. The use of so-called clustered cavities in GKLs allows for improving of both efficiency and bandwidth of these devices [35]-[37].

High-power millimeter-wave gyrotrons are capable of continuous-wave (CW) operation at megawatt (MW) power levels [38], [39]. They are mainly used as sources for electron cyclotron resonance heating (ECRH), electron cyclotron current drive (ECCD), stability control and diagnostics of magnetically confined plasmas for energy generation in controlled fusion reactors. To handle ohmic losses of such power in cavity walls, these gyrotrons must operate at very high-order modes, which form a dense spectrum. To excite the desired mode and to drive it into the regime of MW-level operation with high efficiency requires careful consideration of startup scenario through which the operating parameters of the device are brought to their nominal values [40].

In this work, the author considers some of the described problems related to gyroamplifiers and the startup scenario problem for gyrotron oscillators. The manuscript is organized as follows. The next section contains a simple formalism necessary for understanding the basic principles of a gyrodevice operation. In Chapter 1, the theory of two-stage gyro-TWTs with distributed losses in the first section is presented. The first two sections of this chapter introduce the reader to the basic device configurations and theoretical tools for their analysis. In particular, the method

of non-linear gyro-averaged equations and the corresponding linear theory are reproduced. The third section contains the linear analysis of the effect of distributed losses on the device bandwidth and efficiency and also on the conditions for the parasitic backward wave excitation. Also, in this section, the results of the studies by using the nonlinear theory are shown and compared with the ones obtained by the use of the accurate numerical code MAGY. For this purpose, a concrete Ka-band gyro-TWT designed at NRL is considered.

In Section 4, an attempt to build a nonlinear theory of the gyro-TWT with tapered waveguide radius and external magnetic field is made by the author. The results of the gain and bandwidth analysis for a 250 GHz gyro-TWT with tapered parameters are presented.

Chapter 2 contains the results of a comparative analysis of two gyroklystron configurations. The first one is a regular four-cavity GKL, while the second one is a clustered-cavity GKL with the same number of resonators. In the first section of this chapter, both configurations are shown and principles of their operation are discussed. The second section of this chapter reproduces the point-gap model formalism, which was used for the analysis of both devices. Results of efficiency and gain studies of the schemes are presented in Section 3.

In Chapter 3, the startup scenarios for two high-power millimeter-wave gyrotrons are considered. In particular, the 140-GHz MW-class gyrotron developed by Communications and Power Industries (CPI) for electron plasma heating and current drive experiments on the "Wendelstein 7-X" stellarator is analyzed. The second device under analysis is a 110 GHz 1.5 MW gyrotron presently being under

development at CPI. The calculations are done with the code MAGY for six competing modes and for short and long rise-times of the voltage pulse. Also, in the last section of this chapter, the slow stage of the startup scenario is considered, where attention is paid to the effects of ion compensation of the beam space charge and beam current decrease due to cathode cooling. These effects are modeled within a simple nonlinear theory.

Finally, the manuscript ends with a Summary and references.

I.1: Principles of operation of gyro-devices. Choice of parameters

As known, electrons can radiate when they exhibit some kind of an oscillatory motion in external magnetic or electric fields, which can be either constant or periodic (in the literature this type of radiation mechanism is referred to as bremsstrahlung). For efficient interaction, the Doppler-shifted frequency of the radiated wave should be close to the frequency of electron oscillations, Ω, or its harmonic:

$$\omega - k_z v_z \approx s\Omega \qquad (I.1)$$

Here ω is the frequency and k_z is the axial wavenumber of the EM-wave, whose electric field $\vec{E}$ can be represented as $\vec{E} = \mathrm{Re}\left\{\vec{E}(\vec{r})\exp(i(\omega t - k_z z))\right\}$. Also, in (I.1), v_z is the axial velocity of electrons and s is the number of the harmonic of the electron oscillation frequency Ω. In gyro-devices, the oscillatory motion of electrons is induced by constant magnetic field produced by solenoids or magnets. In this case Ω is the electron cyclotron frequency:

$$\Omega = eH_0 c / \mathcal{E}, \qquad (I.2)$$

where e is the electron charge, H_0 is the magnitude of the magnetic field, c is the speed of light and $\mathcal{E}$ is the electron energy. To make the radiation process efficient, the electrons must be forced to radiate EM-waves in phase, i.e. coherently. Electrons can radiate in phase when they are gathered in compact bunches. Such bunches can be formed in the process of interaction between the RF field and electrons initially uniformly distributed in phase of gyration. The electron bunching in gyro-devices is caused by the relativistic effect – relativistic dependence of electron mass on energy.

9

Now, let us consider the mechanism of the interaction in some more detail. As follows from (I.2), changes in the electron energy $\delta\mathcal{E}$ bring to the changes in the cyclotron frequency $\delta\Omega$ and electron axial velocity δv_z. These changes have opposite signs and, in principle, can compensate for each other. To analyze the phase slippage during the interaction time T, one may introduce the transit angle of electron gyration with respect to the Doppler shifted wave frequency,

$$\Theta = (\omega - k_z v_z - s\Omega)T \tag{I.3}$$

and represent this angle as the sum of the kinematic phase shift

$$\Theta_{kin} = (\omega - k_z v_{z0} - s\Omega_0)T, \tag{I.4}$$

which is proportional to the initial cyclotron resonance mismatch, and the dynamic shift

$$\Theta_{dyn} = (-k_z \delta v_z - s\delta\Omega)T. \tag{I.5}$$

The changes in the cyclotron frequency in accordance with (I.2) can be found as $\delta\Omega = -\Omega_0(\delta\mathcal{E}/\mathcal{E}_0)$. To evaluate the changes in the axial velocity, one may use the fact that the radiation of one photon not only reduces the electron energy by $\delta\mathcal{E} = \hbar\omega$, but also changes the axial momentum, p_z, by $\delta p_z = \hbar k_z$ [41]. Correspondingly, the changes $\delta\mathcal{E}$ and δp_z are related by

$$\delta\mathcal{E} = v_{ph}\delta p_z, \tag{I.6}$$

where $v_{ph} = \omega/k_z$ is the phase velocity of the wave. This expression shows that in the case of electron deceleration by a forward wave ($k_z > 0, v_{ph} > 0$) the electron axial momentum decreases. Correspondingly, when electron is decelerated by a backward wave ($k_z < 0, v_{ph} < 0$), its axial momentum increases.

10

Since the axial momentum is equal to $m\gamma v_z$, where $\gamma = \mathcal{E} / mc^2 = (1 - v^2 / c^2)^{-1/2}$

is the normalized energy or the Lorentz factor, the changes in it can be represented as

$\delta p_z = m(\gamma_0 \delta v_z + v_{z0} \delta\gamma)$. Using (I.6), the change in the axial velocity can be given as

$$\delta v_z = \frac{\delta\gamma}{\gamma_0} \left(\frac{c^2}{v_{ph}} - v_{z0} \right).$$ (I.7)

Substituting this expression into the definition for Θ_{dyn} (I.5) and using the cyclotron

resonance condition (I.1), one may obtain the following expression for the dynamic

phase shift:

$$\Theta_{dyn} = 2\pi N s \frac{\delta\gamma}{\gamma_0} \frac{1-h^2}{1-h\beta_{z0}}.$$ (I.8)

Here $h = k_z c / \omega = c / v_{ph}$ is the normalized axial wavenumber and $2\pi N = \Omega_0 T$, where

N is the umber of electron orbits in the interaction space. It can be noticed that for the

particular choice of $h = 1$, i.e. when the phase velocity is equal to the speed of light,

the dynamic shift is equal to zero for arbitrary energy changes. This is the case when

the changes in the electron cyclotron frequency exactly compensate the ones in the

axial velocity. So, if the cyclotron resonance condition is initially fulfilled in such a

system, then it will be automatically fulfilled later for arbitrary large changes in the

electron energy. This remarkable effect is known as the *autoresonance* [42], [43].

One of the major concerns for practically all sources of coherent radiation is

their efficiency. The real efficiency of any source should be evaluated by calculating

the efficiency of one electron and averaging it over all initial distributions of electrons

in the coordinate and momentum space. Let us briefly consider the results of the

analysis of the single-particle efficiency. Expression (I.6) can be rewritten in the form

11

$$p_{z0} - p_z = \frac{\mathcal{E}_0 - \mathcal{E}}{v_{ph}}, \qquad (I.9)$$

which allows determining the optimum phase velocity necessary for the complete stoppage of electron axial motion and extraction of its kinetic energy, i.e. making $p_{z,final} = 0$ and $\mathcal{E}_{final} = mc^2$. One may easily find from these conditions

$$\frac{v_{ph,opt}}{c} = \beta_{ph,opt} = \frac{\gamma_0 - 1}{\gamma_0 \beta_{z0}}. \qquad (I.10)$$

The electron orbital momentum, $p_\perp$, which can be represented as

$$p_\perp^2 = p_{\perp 0}^2 + m^2 c^2 (1 - h^2)(\gamma_0 - \gamma)^2 - 2m^2 c^2 \gamma_0 (\gamma_0 - \gamma)(1 - h\beta_{z0}) \qquad (I.11)$$

by the use of the general relation $\mathcal{E}^2 = m^2 c^4 + c^2(p_\perp^2 + p_z^2)$ and (I.9), also becomes equal to zero for $h = 1/\beta_{ph,opt}$. So, the condition (I.10) is the condition for the complete electron deceleration, which is the case of single-particle efficiency equal to 100%. In practice, the electron beam parameters are often given in terms of the beam voltage V_b, which is related to γ_0 as $V_b = (\gamma_0 - 1)(mc^2/e)$, and the orbital-to-axial velocity ratio, $\alpha = v_{\perp 0}/v_{z0}$. So, (I.10) can be rewritten as [44]

$$\beta_{ph,opt} = \left[\frac{(\gamma_0 - 1)(1 + \alpha^2)}{\gamma_0 + 1} \right]^{\frac{1}{2}}. \qquad (I.12)$$

As mentioned, gyro-devices belong to the class of fast-wave devices, in which $\beta_{ph} > 1$. Therefore, the interaction with fast waves is optimal (in the sense of single-particle efficiency) when the velocity ratios are large enough:

$$\alpha^2 > \frac{2}{\gamma_0 - 1}. \qquad (I.13)$$

In order to estimate the magnitude of the external magnetic field, the kinematic phase shift given by (I.4) should be considered. It should provide the displacement of an electron bunch into the decelerating phase, i.e. $\Theta_{kin} \sim \pi$. This yields the following estimate for the initial cyclotron frequency:

$$\Omega_0 \sim \frac{\omega}{s}(1 - h\beta_{z0})\left(1 - \frac{1}{2Ns}\right).$$ (I.14)

The term $1/2Ns$ in this expression characterizes the mismatch of the cyclotron resonance with respect to the Doppler-shifted wave frequency. This mismatch is inversely proportional to the cyclotron harmonic number, s, and the number of electron orbits, N. The number of electron orbits is proportional to the interaction length and can be chosen in accordance with (I.8). As follows from this expression, the changes in the electron energy are of the order of

$$\frac{\delta\gamma}{\gamma_0} \sim \frac{1}{sN}\frac{1 - h\beta_{z0}}{1 - h^2}$$ (I.15)

when the dynamic phase shift is of the order of 2π. The number of orbits in this expression can be large when the operation is close to autoresonance (in this case the terms sN and $1-h^2$ compensate each other). For the energy changes of the order of the initial kinetic energy, $\mathcal{E}_0 - mc^2$, this means

$$|1 - h^2| << \frac{1 - h\beta_{z0}}{1 - \gamma_0^{-1}}.$$ (I.16)

It follows from applying of (I.15) to (I.11) in the case of $N >> 1$ that the term $m^2c^2(1 - h^2)(\gamma_0 - \gamma)^2$ in (I.11) is small, and, therefore, the orbital momentum is approximately equal to

$$p_\perp \approx p_{\perp 0} \left\{ 1 - \frac{2}{\beta_{\perp 0}^2}(1 - h\beta_{z0})\left(1 - \frac{\gamma}{\gamma_0}\right) \right\}^{1/2} . \tag{I.17}$$

When $\beta_{ph} > \beta_{ph,opt}$, the decelerating electron loses its orbital momentum prior to stopping its axial motion. In this case, the single-particle efficiency, which is defined as $\eta_{sp} = |\delta\mathcal{E}| / (\mathcal{E}_0 - mc^2)$, can be found for the final value of $p_\perp = 0$:

$$\eta_{sp} = \frac{\beta_{\perp 0}^2}{2(1 - h\beta_{z0})(1 - \gamma_0^{-1})} . \tag{I.18}$$

The wave electric field can be evaluated by using the general equation for the electron energy,

$$\frac{d\mathcal{E}}{dt} = -e(\vec{v} \cdot \vec{E}) , \tag{I.19}$$

which gives estimates for the changes in electron energy during the interaction time T: $|\delta\mathcal{E}| \sim ev_\perp ET$. The synchronous electric field E_s has a structure of a rotating multipole in the case of resonance at an arbitrary cyclotron harmonic, s [45]. It can be represented as $E_s \sim (a/\lambda)^{s-1} E$, where $a = v_\perp / \Omega_0$ is the Larmor radius. The total length of the electron trajectory in the interaction space can be estimated as $2\pi a N$ if the orbital-to-axial velocity ratio is large. Therefore,

$$|\delta\mathcal{E}| \sim e(a/\lambda)^{s-1} E 2\pi a N . \tag{I.20}$$

By substituting this expression into (I.15) and using the cyclotron resonance condition (I.1), one may get [46]

$$\frac{eE}{mc\omega\gamma_0}\left(\frac{a}{\lambda}\right)^{s-1}\beta_{\perp 0} \sim \frac{1}{2\pi(sN)^2}\frac{(1 - h\beta_{z0})^2}{1 - h^2} . \tag{I.21}$$

This expression shows that the wave amplitude required for electron deceleration is inversely proportional to N^2. Also, the ratio a/λ in the left-hand side of (I.21) can be written as $a/\lambda \approx s\beta_{\perp 0}/2\pi(1-h\beta_{z0})$, so the wave amplitude is inversely proportional to $\beta_{\perp 0}^s$.

So far, the electron deceleration by a wave of given amplitude has been analyzed in this section. The EM field is excited (or amplified) by an electron beam when real devices are considered. Correspondingly, the field amplitude depends on the beam parameters. This dependence can be determined by a balance equation for the simplest case of oscillations in a single cavity. The power balance equation is valid for stationary regimes. In such regimes, the microwave power withdrawn from the beam is equal to the power of the microwave losses (ohmic and diffractive) in a cavity having a finite quality factor Q:

$$\eta P_b = (\omega/Q)W. \tag{I.22}$$

Here $P_b = V_b I_b$ is the beam power, η is the device interaction efficiency , and W is the microwave energy stored in the cavity. The energy is determined as $V\left\langle |E|^2 \right\rangle/8\pi$, where V is the cavity volume, which depends on the operating wavelength and mode, and the angular brackets designate the averaging of the intensity of the field over the cavity volume.

Chapter 1: Two-Stage Gyro-TWTs

1.1: Basic device configurations

A typical configuration of a gyro-TWT is shown in Fig. 1.1. It consists of a magnetron injection gun (MIG), the interaction region, input and output windows, collector and one or more solenoids. The MIG is responsible for producing an e-beam and launching it into the interaction space, where electrons exchange their energy with an EM-wave. The signal EM-wave is fed into the tube through the input window. Having interacted with the beam and amplified it leaves the device through the output window. The exhausted electrons are accumulated at the collector. The
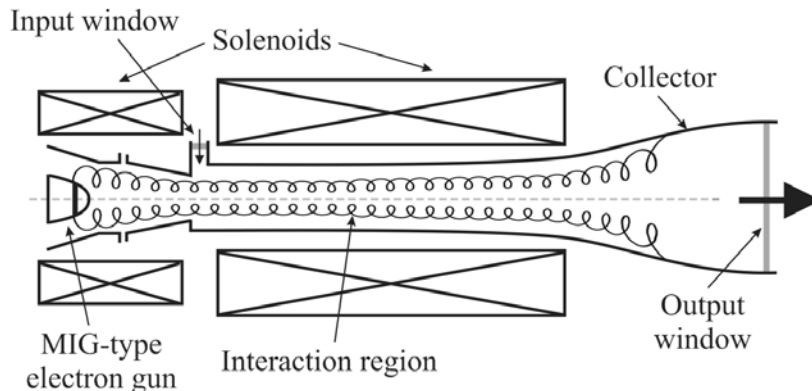
Fig. 1.1. Typical gyro-TWT configuration.

solenoid produces a strong magnetic field to support the cyclotron motion of the beam electrons. The axial motion of electrons is provided by a potential difference between the MIG emitter and the interaction region. Fig. 1.2 schematically shows the geometry of a two-stage gyro-TWT with distributed losses in the first section. In practice, losses in such devices can be realized by the use of a layer of lossy material

spread on the waveguide walls in the interaction region [29]. The use of diffraction losses in gyro-TWTs is also possible [30].
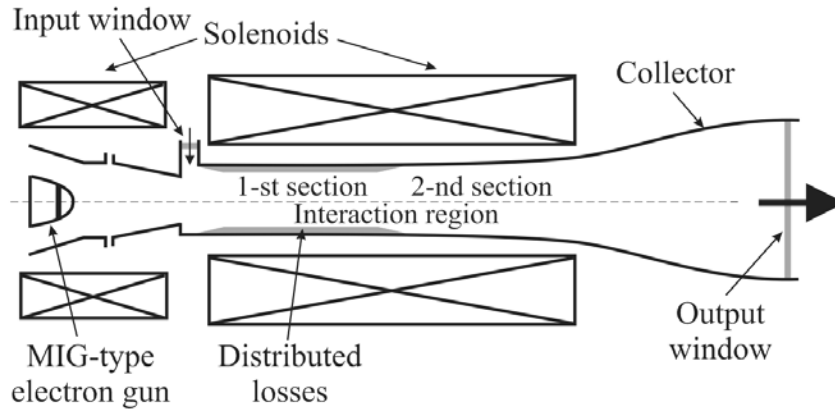
Fig. 1.2. Configuration of a two-stage gyro-TWT with distributed losses in the first section.

Fig. 1.3 demonstrates the scheme of a severed two-stage gyro-TWT. This device allows operation at different cyclotron harmonics in each section. In particular, it might prove advantageous to operate in frequency multiplication regimes. Also, by a proper choice of each section length one may solve the stability problem for such configuration.
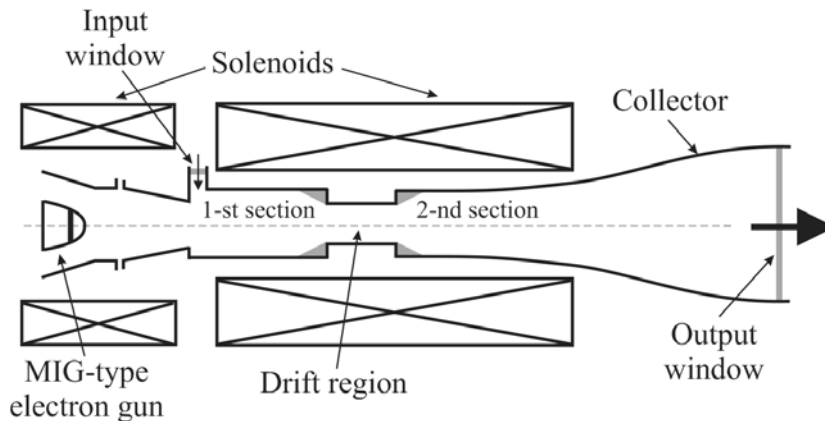
Fig. 1.3. Configuration of a two-stage severed gyro-TWT.

1.2: General formalism

1.2.1: Self-consistent set of equations for the gyro-TWT

The operation of a gyro-TWT can be described by a self-consistent set of nonlinear equations. This set consists of equations of electron motion through the waveguide field and the equation to describe wave excitation by an electron beam. The method used for deriving these equations is based on presenting the EM-field acting upon a gyrating electron as a superposition of angular harmonics of the waves that rotate around an electron guiding center. The cyclotron resonance condition allows selecting just one resonant harmonic from all the harmonic components representing the field. All others will vanish after the equation of motion has been averaged over fast gyrations. The averaged equations have a compact and general form, which greatly simplifies their analysis. This method was initially suggested by Gaponov in the linear theory of cyclotron resonance masers [19] and later used by V.K. Yulpatov for developing the nonlinear theory [20]. The detailed derivation of these equations for the gyro-TWTs can be found in Ref. 25. Here the author just reproduces the self-consistent set used for obtaining the results presented in this work:

$$\frac{dw}{d\zeta} = -2\frac{(1-w)^{s/2}}{1-bw}\operatorname{Re}(Fe^{-i\vartheta}) \tag{1.1}$$

$$\frac{d\vartheta}{d\zeta} = \frac{1}{1-bw}\{w + s(1-w)^{\frac{s}{2}-1}\operatorname{Im}(Fe^{-i\vartheta})\} \tag{1.2}$$

$$\frac{dF}{d\zeta} - i\Delta F = -I_0\frac{1}{2\pi}\int_0^{2\pi}\frac{(1-w)^{s/2}}{1-bw}e^{i\vartheta}d\vartheta_0 \tag{1.3}$$

In these equations, $w = (1-h\beta_{z0})(\gamma_0 - \gamma)/\beta_{\perp0}^2\gamma_0$ is the normalized electron energy, where $h = k_z c/\omega$ is the normalized axial wavenumber, $\beta_{z0} = v_{z0}/c$ and $\beta_{\perp0} = v_{\perp0}/c$

are, respectively, the initial electron axial and orbital velocity components normalized to the speed of light, γ is the electron energy normalized to the rest energy, and γ_0 is its initial value determined by the beam voltage, V_b: $\gamma_0 = 1 + eV_b / mc^2$. In (1.1)-(1.3) ϑ is a slowly-variable gyrophase of the resonant cyclotron harmonic s with respect to the phase of the forward $TE_{m,p}$ wave:

$$\vartheta = s(\theta - \Omega_0 \tau) - \omega t_0 + k_z \int_0^\tau (v_z - v_{z0}) d\tau' - (s \mp m)\psi .$$

Here Ω_0 is the electron cyclotron frequency, ψ is the azimuthal coordinate of the electron guiding center and m is the azimuthal index of the wave. At the entrance, this phase has an initial value $\vartheta(0) = s\theta_0 - \omega t_0 - (s \mp m)\psi$, which is uniformly distributed in all beamlets from 0 to 2π for an unmodulated electron beam. Also, in (1.1)-(1.3), $\zeta = \mu \omega z / c\beta_{z0}$ is the normalized axial coordinate, where parameter $\mu = \beta_{\perp 0}^2 (1 - h^2) / 2(1 - h\beta_{z0})$ characterizes the effect of the changes in electron energy on the cyclotron resonance conditions. The parameter $b = h\beta_{\perp 0}^2 / 2\beta_{z0}(1 - h\beta_{z0})$ characterizes the changes in the electron axial velocity with the change in electron energy and Δ is the normalized cyclotron resonance mismatch between the Doppler-shifted wave frequency $\omega - k_z v_z$ and the resonant harmonic of the electron cyclotron frequency $s\Omega_0$:

$$\Delta = (\omega - k_z v_{z0} - s\Omega_0) / \omega\mu .\qquad(1.4)$$

The normalized beam current parameter, I_0, present in the last equation is equal to

$$I_0 = 16 \frac{eI_b}{mc^3} \frac{\kappa^{2(s-2)}}{h} \frac{(1 - h\beta_{z0})^{5-2s}}{\gamma_0 \beta_{\perp 0}^{2(3-s)}} \left[\frac{s^{s-1}}{(s-1)!2^s} \right]^2 G_{cpl} \qquad(1.5)$$

19

where $\kappa^2 = 1 - h^2$ and parameter $G_{cpl} = J_{m\mp s}^2(k_\perp R_0)/(v^2 - m^2)J_m^2(v)$ describes the coupling of a beam having the radius of electron guiding centers R_0 to the field of a *TE*-wave in a cylindrical waveguide. The initial value of the normalized amplitude, F_0 is determined by the input power, P_{in} as

$$| F_0 | = 4 \left[2 \frac{e^2 P_{in}}{m^2 c^5} \frac{G_{cpl}}{h} \right]^{1/2} \frac{(s\kappa)^{s-1} \beta_{\perp 0}^{s-4}(1 - h\beta_{z0})^{3-s}}{\gamma_0 \kappa (s-1)! 2^s}. \tag{1.6}$$

The ratio $m^2 c^5/e^2$ in square brackets is a product of the fundamental constants $mc^3/e =$ 17.04 kA and $mc^2/e = 511$ kV and is equal to $8.687 \cdot 10^6$ kW. The set (1.1)-(1.3) can be supplemented by the expression for the orbital efficiency of interaction

$$\eta_\perp = \frac{1}{2\pi} \int_0^{2\pi} w d\vartheta_0, \tag{1.7}$$

which characterizes the changes in the electron orbital momentum in the process of interaction. The total electron efficiency is related to $\eta_\perp$ as

$$\eta = \eta_{sp} \eta_\perp = \frac{\beta_{\perp 0}^2}{2(1 - \gamma_0^{-1})(1 - h\beta_{z0})} \eta_\perp, \tag{1.8}$$

where η_{sp} is the single-particle efficiency discussed in the Introduction. The system of equations (1.1)-(1.3) has the following integral

$$| F |^2 - | F_0 |^2 = I_0 \eta_\perp, \tag{1.9}$$

which represents the energy conservation law for the beam-wave system.

Typical processes of the electron energy modulation, phase bunching and wave amplification are shown in Fig. 1.4. These results are obtained by integrating Eqs (1.1)-(1.3) with the following set of parameters: $s = 1$, $b = 0.1$, $\Delta = 0.5$, $I_0 = 0.1$ and $F_0 = 0.01$. Initially, the changes in the electron energy and phase are linear and
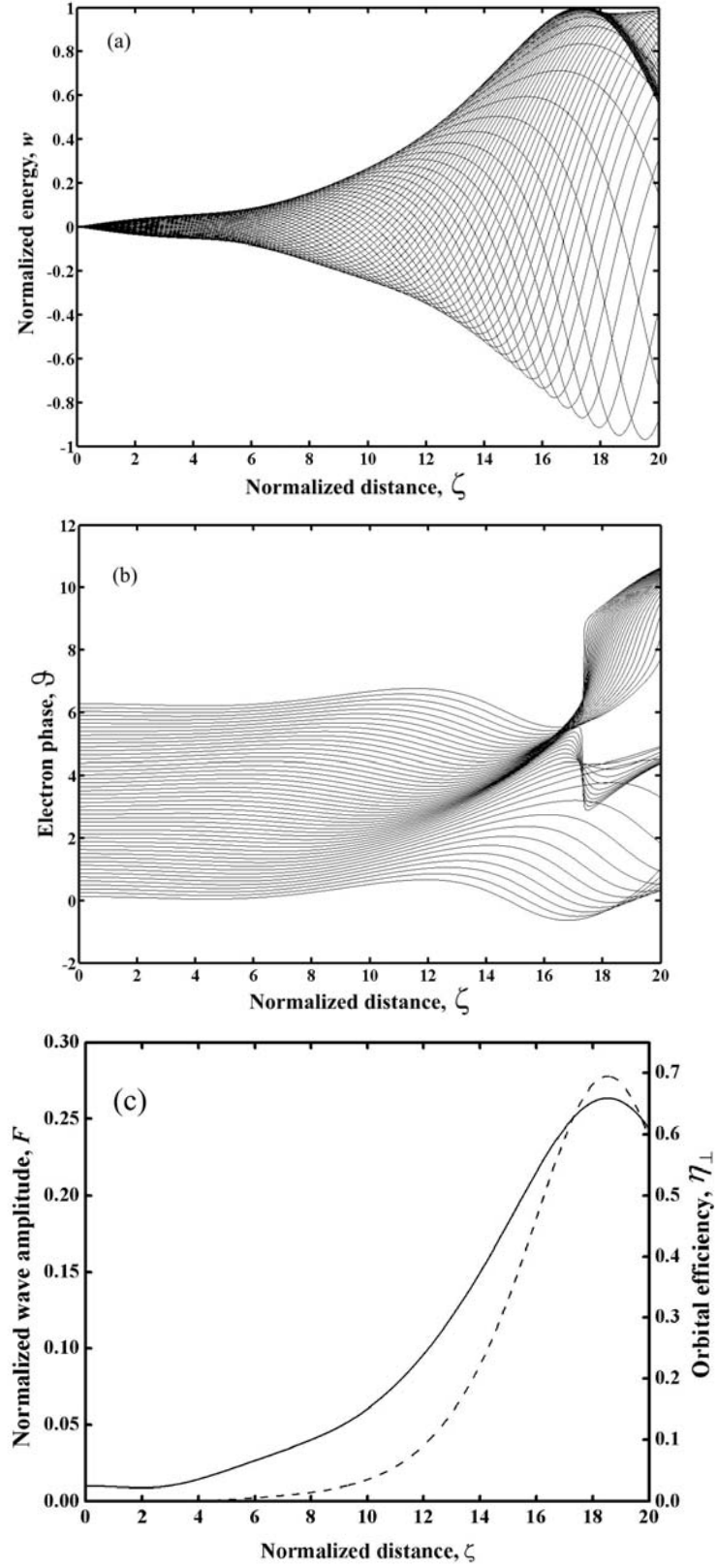
Fig. 1.4. Typical processes of (a) electron energy modulation, (b) phase bunching and (c) wave amplification.

the wave amplitude grows exponentially, which is the linear stage of interaction. Then the saturation effects become pronounced, when the changes in the electron energy and phase are significant, and the wave amplitude reaches its maximum. As follows from the comparison of Fig. 1.4(b) with Fig 1.4(c), the maximum of the wave amplitude corresponds to the shift of an electron bunch in phase on the order of π. Since for realizing the wave amplification the bunch should be formed in the decelerating phase, this shift indicates that electrons move from the decelerating phase into the accelerating one. In the latter phase, the electrons start to withdraw the EM wave energy back, thus decreasing the wave amplitude.

Equations (1.1)-(1.3) are given for an ideal electron beam with no velocity spread. In order to take into account the effect of the spread, it is expedient to normalize all dimensionless parameters to the mean values of velocity components $\overline{\beta}_\perp$ and $\overline{\beta}_z$ [47], i.e. $\overline{\mu} = \overline{\beta}_\perp^2 (1 - h^2) / 2(1 - h\overline{\beta}_z)$, $\overline{b} = h\overline{\beta}_\perp^2 / 2\overline{\beta}_z (1 - h\overline{\beta}_z)$, $\overline{\Delta} = (1 - h_z\overline{\beta}_z - s\Omega_0 / \omega) / \overline{\mu}$ and introduce the following coefficients describing the effect of the spread on these parameters:

$$k_b \equiv k_\mu = \frac{\overline{\beta}_z}{\beta_{z0}} \frac{1 - h\overline{\beta}_z}{1 - h\beta_{z0}} \left(\frac{\beta_{\perp 0}}{\overline{\beta}_\perp} \right)^2$$

$$k_F = \frac{\overline{\beta}_z}{\beta_{z0}} \left(\frac{\beta_{\perp 0}}{\overline{\beta}_\perp} \frac{1 - h\overline{\beta}_z}{1 - h\beta_{z0}} \right)^{s-2}$$

$$k_\Delta = \frac{\overline{\beta}_z}{\beta_{z0}},$$

where $k_b = k_F = k_\Delta = 1$ in the absence of the spread. Also, an additional averaging of the source term in the right-hand side of the wave excitation equation (1.3) over the

velocity distribution is necessary. Then one can rewrite equations (1.1)-(1.3) for the case with the electron velocity spread as

$$\frac{dw}{d\zeta} = -2\frac{(1-w)^{s/2}}{1-k_b\bar{b}w}\operatorname{Re}(k_F Fe^{-i\vartheta}) \tag{1.10}$$

$$\frac{d\vartheta}{d\zeta} = \frac{1}{1-k_b\bar{b}w}\left\{k_\mu w + \Delta(1-k_\Delta - k_b\bar{b}w) - \frac{h}{\mu}(k_\Delta - 1) + s(1-w)^{\frac{s}{2}-1}\operatorname{Im}(k_F Fe^{-i\vartheta})\right\} \tag{1.11}$$

$$\frac{dF}{d\zeta} - i\Delta F = -I_0\int W(\beta_{\perp 0})\frac{k_F k_b}{k_\Delta}\left\{\frac{1}{2\pi}\int_0^{2\pi}\frac{(1-w)^{\frac{s}{2}}}{1-k_b\bar{b}w}e^{i\vartheta}d\vartheta_0\right\}d\beta_{\perp 0}. \tag{1.12}$$

The velocity distribution function $W(\beta_{\perp 0})$ in (1.12) obeys the normalization condition $\int W(\beta_{\perp 0})d\beta_{\perp 0} = 1$. The expression (1.7) for the orbital efficiency takes the following form in this case:

$$\eta_\perp = \int W(\beta_{\perp 0})\frac{k_b}{k_\Delta}\left\{\frac{1}{2\pi}\int_0^{2\pi}wd\vartheta_0\right\}d\beta_{\perp 0}. \tag{1.13}$$

If distributed losses are present in the circuit, the axial wavenumber becomes complex: $k_z = k_z' + k_z''$ and so does the normalized detuning parameter: $\Delta = \Delta' + i\Delta'' = \Delta' + id$, where $d \equiv \Delta''$ is the attenuation parameter. In this case, the energy conservation law (1.9) can be written as

$$|F|^2 - |F_0|^2 = \eta_\perp I_0 - 2\int_0^\zeta \Delta''|F|^2 d\zeta'. \tag{1.14}$$

It shows that the changes in the wave intensity are determined by the power extracted from the beam and wave attenuation in the circuit.

1.2.2: Linear theory of the gyro-TWT

In the small-signal regime, the EM-wave can produce only small perturbations in electron energy and phase, hence in Eqs. (1.1)-(1.3) $w = w_{(1)}$, $\vartheta = \vartheta_{(0)} + \vartheta_{(1)}$, where $\vartheta_{(1)} \ll \vartheta_{(0)}$, the subscripts (0) and (1) denote zero- and first-order terms, respectively, and $\vartheta_{(0)} = \vartheta(0)$. Therefore, by linearizing Eqs. (1.1)-(1.3) with respect to these perturbations and introducing

$$\tilde{w} = \frac{1}{F_0} \frac{1}{2\pi} \int_0^{2\pi} w_{(1)} e^{i\vartheta_0} d\vartheta_0$$

$$\tilde{\vartheta} = \frac{1}{F_0} \frac{1}{2\pi} \int_0^{2\pi} \vartheta_{(1)} e^{i\vartheta_0} d\vartheta_0$$

$$\tilde{F} = \frac{F}{F_0}$$

one can bring these equations to the form

$$\frac{d\tilde{w}}{d\zeta} = -\tilde{F} \tag{1.15}$$

$$\frac{d\tilde{\vartheta}}{d\zeta} = (1 - b\varDelta)\tilde{w} - i\frac{s}{2}\tilde{F} \tag{1.16}$$

$$\frac{d\tilde{F}}{d\zeta} - i\varDelta\tilde{F} = -I_0\left\{i\tilde{\vartheta} + (b - \frac{s}{2})\tilde{w}\right\} \tag{1.17}$$

Assuming an $\exp(i\varGamma\zeta)$ dependence for $\tilde{w}, \tilde{\vartheta}$ and $\tilde{F}$ (where $\varGamma$ is the propagation constant in the presence of the electron beam), i.e.

$$\tilde{w} = \sum_{l=1}^{3} A_l \exp(i\varGamma_l\zeta), \quad \tilde{\vartheta} = \sum_{l=1}^{3} B_l \exp(i\varGamma_l\zeta), \quad \tilde{F} = \sum_{l=1}^{3} C_l \exp(i\varGamma_l\zeta) \tag{1.18}$$

Here the coefficients A_l and B_l can be expressed with the use of (1.15)-(1.17) via C_l as

$$A_l = i \frac{C_l}{\Gamma_l} \text{ and } B_l = (1 - \Delta b) \frac{C_l}{\Gamma_l^2} - \frac{s}{2} \frac{C_l}{\Gamma_l}.$$

With the use of (1.18), the following dispersion equation can be obtained from (1.15)-(1.17) [24], [46], [48], [49]:

$$(\Gamma - \Delta)(\Gamma^2 + I_0 b) \pm I_0 (1 - s\Gamma) = 0, \tag{1.19}$$

where the "+" sign before the second term corresponds to the equation for the forward wave and the "−" sign corresponds to the one for the backward wave.

Let us establish a relationship between our propagation constant, Γ, which is determined by (1.19), and the axial wavenumber in the presence of the beam, $k_{z,b}$. When the beam current is negligibly small ($I_0 \to 0$), equation (1.19) yields one solution $\Gamma = \Delta$ and another degenerate solution $\Gamma = 0$. The former describes the wave propagation in a 'cold' waveguide, while the latter describes the cyclotron waves in the beam. Since the detuning Δ contains the axial wavenumber in a 'cold' system, while the variable Γ contains $k_{z,b}$, the solution $\Gamma = \Delta$ simply indicates that in the absence of the beam $k_{z,b} = k_z$. In the presence of a beam, as follows from these definitions, $k_{z,b} = k_z - \beta_{\perp 0}^2 \omega (\Gamma - \Delta) / 2 v_{z0}$. (Here we assumed that the operating voltage and the axial wavenumber are not too large and, therefore, Δ can be expressed as $\Delta \approx (2 / \beta_{\perp 0}^2)(1 - h\beta_{z0} - s\Omega_0 / \omega)$). Thus, the growth-rate of the wave can be expressed via the imaginary part of Γ as $|\text{Im} k_{z,b}| = |\text{Im} \Gamma| \beta_{\perp 0}^2 \pi / \lambda \beta_{z0}$, where λ is the wavelength in free space.

The coefficients C_l in (1.18) are to be determined from the boundary conditions. Taking into account the absence of modulation of electron energies and

25

phases at the entrance, as well as the existence of an input signal wave, one may obtain:

$$\sum_{l=1}^{3} C_l = 1, \quad \sum_{l=1}^{3} \frac{C_l}{\Gamma_l} = 0, \quad \sum_{l=1}^{3} \left(1 - b\Delta - \frac{s}{2}\Gamma_l\right)\frac{C_l}{\Gamma_l^2} = 0. \tag{1.20}$$

Note that in our notations the wave amplitude is normalized to its initial value. These equations can be solved for C_l and then expressions (1.18) should be used to find the electron energy and phase and the wave amplitude at the end of the interaction region. For the case of a multi-stage gyro-TWT, the boundary conditions at the n-th stage can be written as

$$\sum_{l=1}^{3} C_l^{(n)} = \tilde{F}(\zeta_{in}^{(n)})$$

$$i\sum_{l=1}^{3} \frac{C_l^{(n)}}{\Gamma_l^{(n)}} = \tilde{w}(\zeta_{in}^{(n)}) \tag{1.21}$$

$$\sum_{l=1}^{3} \left(1 - b\Delta^{(n)} - \frac{s}{2}\Gamma_l^{(n)}\right)\frac{C_l^{(n)}}{\Gamma_l^{(n)2}} = \tilde{g}(\zeta_{in}^{(n)}),$$

where $\zeta_{in}^{(n)}$ is the normalized distance at which the n-th waveguide section begins. Equations (1.21) form a set of linear inhomogeneous algebraic equations, which can be easily solved. The coefficients of these equations depend on $\Gamma^{(n)}$, which are the roots of Eq. (1.19) for the n-th stage. The amplitude at the output,

$$\tilde{F}_{out} = \sum_{l=1}^{3} C_l^{(N)} \exp(i\Gamma_l^{(N)}(\zeta_{out}^{(N)} - \zeta_{in}^{(N)})), \tag{1.22}$$

where N is the number of the final stage, determines the gain of the device:

$$G = 20\log\left\{\left\|\tilde{F}_{out}\right\|\right\}. \tag{1.23}$$

1.3: Two-stage gyro-TWTs with distributed losses

As mentioned in the introduction, in tubes with a long interaction region a parasitic excitation of backward waves may occur. The use of distributed wall losses or diffraction losses for the suppression of such spurious oscillations was successfully demonstrated in Refs. [29] and [30]. A simple linear theory of a gyro-TWT, in which part of the waveguide has finite losses is presented in the following sections.

1.3.1: Results of the linear theory. Gain and bandwidth studies

Before the analysis of the parasitic BW suppression our study was focused on the effect of distributed losses on the gain and bandwidth of the two-stage gyro-TWT. The author was obtaining the solutions of Eq. (1.19) as functions of the real part of the normalized detuning, Δ', for finite values of the loss parameter d. In Fig. 1.5, the corresponding imaginary parts of the complex roots Γ are shown. Here Figs. 1.5 (a) and 1.5 (b) correspond to two respective magnitudes of the normalized beam current parameter, namely 0.03 and 0.3. It follows from these results that losses decrease the maximum growth rate of the wave but, at the same time, increase the range of resonance detunings, at which the wave amplification is possible. To check the validity of the linear model, we applied it to the Ka-band gyro-TWT designed at NRL [30]. This tube is driven by a 70 kV, 6 A electron beam with the orbital-to-axial velocity ratio of about 0.71. The interaction circuit is a circular waveguide of 2.72 mm radius and of the 27 cm total length. The first 22 cm of this waveguide are
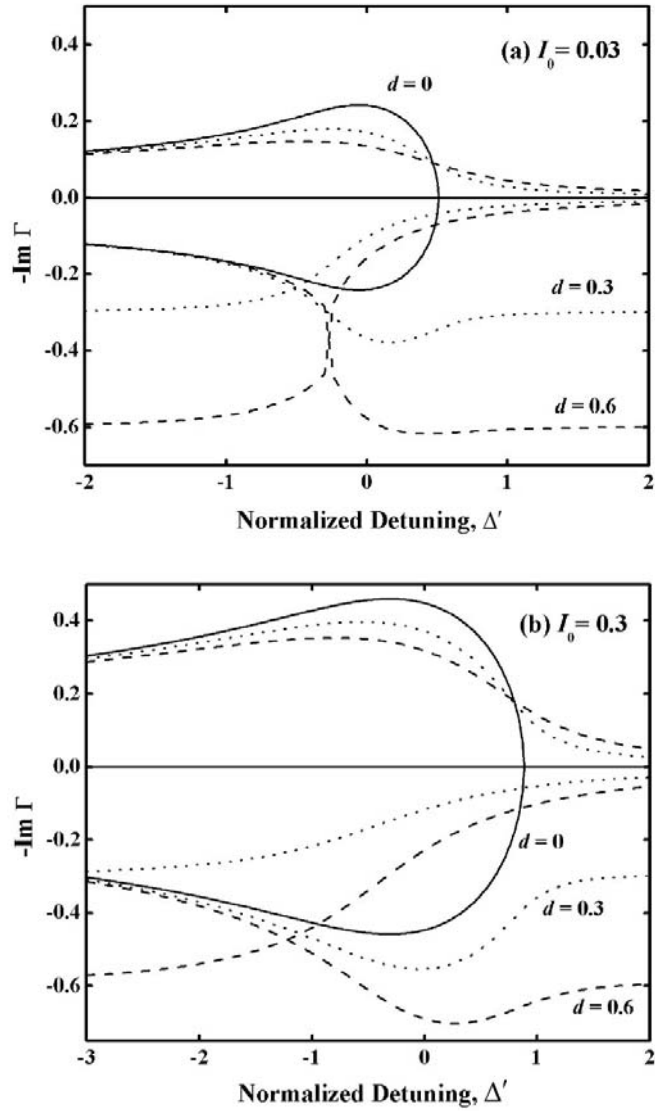
Fig. 1.5. Imaginary parts of propagation constants as functions of the normalized detuning for several values of the loss parameter d and two values of the normalized beam current parameter I_0.

characterized by cold circuit losses of 3.45 dB/cm, which correspond to the loss parameter $d \approx 0.55$ at the central frequency of 35 GHz. The last 5 cm of the waveguide are lossless. The operating mode is TE_{11}. The circuit geometry and magnetic field profiles for this tube are shown in Fig. 1.6. The resulting gain of the

tube calculated in accordance with Eq. (1.23) is shown in Fig. 1.7. As can be seen, the bandwidth at the -3 dB level is about 8% and the maximum gain is about 50 dB. For
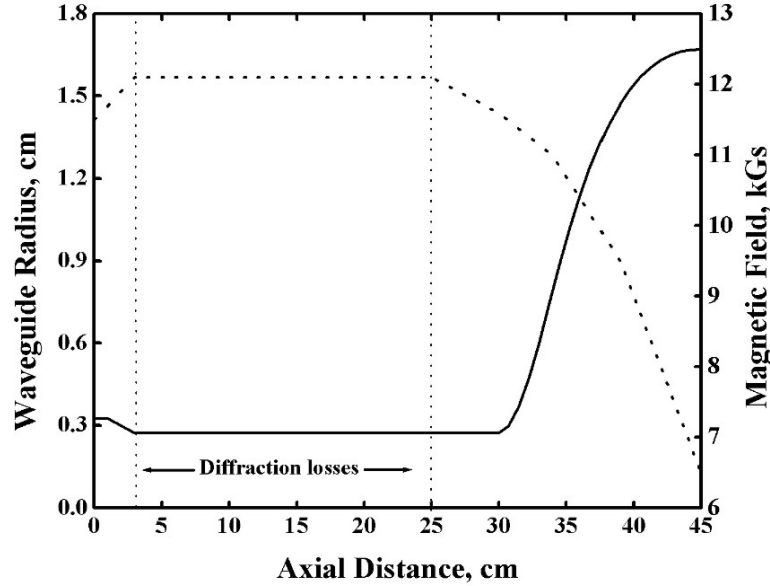
Fig. 1.6. Circuit geometry (solid) and magnetic field (dotted) profiles of the gyro-TWT designed at NRL.

the sake of comparison, also shown are the calculated design data (dashed line), which correspond to the input power value $P_{in} = 0.9$ W, being the case closest to the small-signal operation. The data were obtained by the use of self-consistent, time-dependent code, MAGY [26], which has been known to provide accurate results that are, in most cases, in a close agreement with the measurements. As can be seen, there is a good agreement between the gains calculated by the two methods. The gain found in Ref. 30 is a little smaller, possibly, first due to the effect of 4% electron velocity spread and second, because at $P_{in} = 0.9$ W one may already observe in Fig. 11 of this paper some saturation effects. The fact that the calculated bandwidth in Ref. 30 is

29
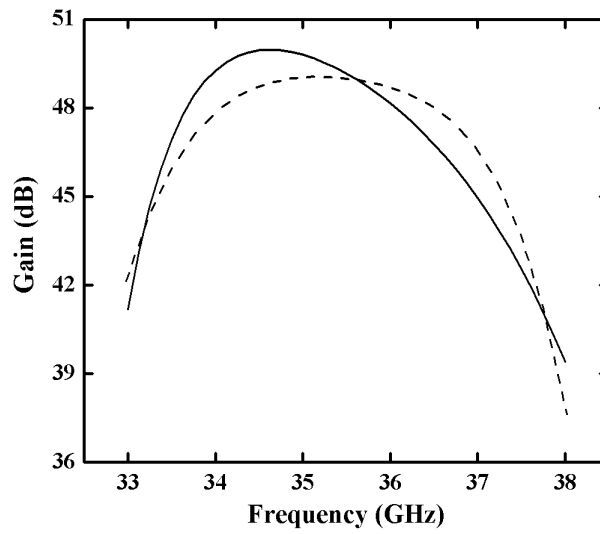
Fig. 1.7. Gain as a function of frequency for the NRL gyro-TWT. The results of Ref. [30] are shown by the dashed line.

slightly larger (about 10%) than the one obtained in our calculations can be attributed to the changes of the external magnetic field in the lossless section of the waveguide, which we ignored in our model.

1.3.2: Analysis of backward wave excitation

As already mentioned, parasitic excitation of backward waves is one of the most critical issues in the development of high-gain gyro-TWTs. Since it is preferable to have an amplifier capable of stable operation even in the absence of the signal (so-called 'zero-drive' stability), the conditions for onset of oscillations in a two-stage gyro-TWT in the absence of forward waves will be considered below. In general, the similarity of the dispersion equation for gyro-backward wave oscillators (gyro-BWO's) to that for linear BWO's allows one to study the starting conditions in gyro-BWO's by the methods that are known for conventional BWO's [50]. Such a method was used for analyzing the starting conditions in a single-stage gyro-BWO [51], [52].

We applied the same method for studying a two-stage gyro-BWO whose first section included distributed losses. As described in section 1.2.2, the values of electron energy and phase and the wave amplitude at the end of the first stage were used as initial conditions for the corresponding variables in the second stage. We were interested solely in such solutions of the dispersion equation that would render the total wave amplitude $\tilde{F}$ equal to zero at a distance ζ_{st} from the beginning of the interaction region. In other words, we expected the excitation of the BW to start from a zero-amplitude. With given values of the normalized current I_0, loss parameter d and the length of the first section $\zeta_{out}^{(1)}$ one may find a pair $(\Lambda'_{st}, \zeta_{st})$ that would satisfy this condition. Fig. 1.8 shows an example of such a search in the lossless case (dotted lines) and in the case with distributed losses in the first section of the tube (solid lines). The normalized length of the lossy section is equal to 10 and the corresponding

31
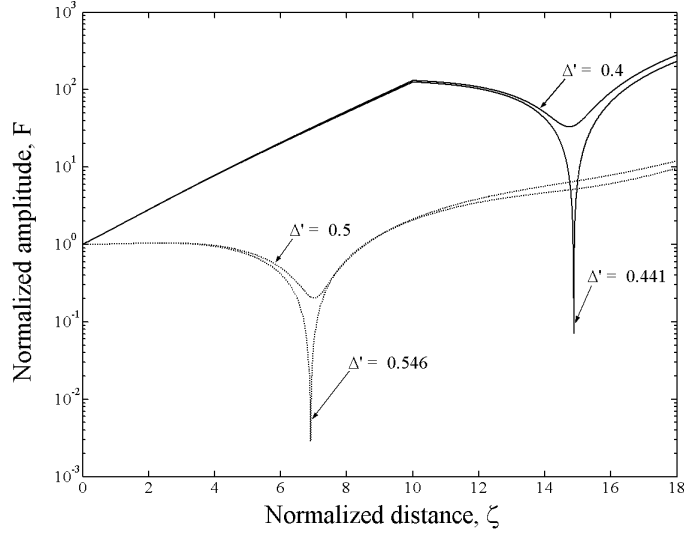
Fig. 1.8. Excitation of backward waves in the lossy (solid) and lossless (dotted) cases. The amplitude of a BW starts growing from the zero amplitude, which can be obtained by varying the detuning parameter Δ'.

loss parameter d is equal to 0.5. One may see that in the lossless case the amplitude of the backward wave starts growing when the interaction distance exceeds $\zeta_{st} \approx 6.9$ whereas in the presence of losses $\zeta_{st} \approx 14.9$. The corresponding detuning parameters are given in the figure for both cases. The curves for $\Delta' = 0.4$ and $\Delta' = 0.5$ indicate no growth of the BW and are shown as an example. For the detuning parameters corresponding to the BW solutions, one may obtain the frequency at which the oscillations occur once the magnitude of the external magnetic field and waveguide parameters are given.

The results of a more detailed analysis are presented in Fig. 1.9 as the dependences of the length of the second stage at which the self-excitation starts, on the loss parameter d for several values of the normalized current parameter I_0 and several lengths of the first stage. Solid, dashed and dotted lines correspond to the

32
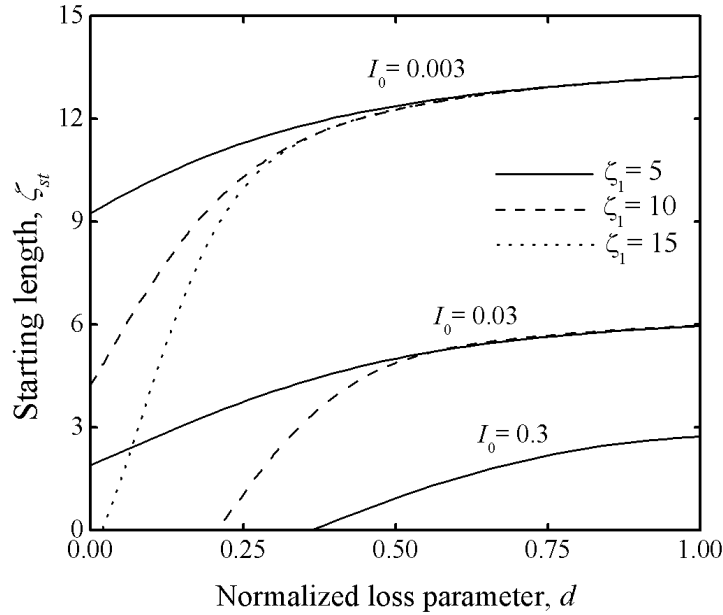
Fig. 1.9. BW self-excitation conditions: the starting length of the second section is shown as the function of the loss parameter d for several values of the normalized beam current and different lengths of the first section ζ_1, which are indicated in the figure.

normalized length of the first stage equal to 5, 10 and 15, respectively. As can be seen from this figure, the starting length of the second stage strongly depends on the length of the first stage when the losses are quite small. However, starting from the loss parameter values $d \simeq 0.5$, the length of the first stage does not play any significant role. This shows that the first stage becomes so lossy that the oscillations can appear only in the second, lossless stage.

The results illustrating the effect of losses on the self-excitation of the first section alone are shown in Fig. 1.10. Here the starting length of a single-stage gyro-BWO is shown as a function of the loss parameter for several values of the normalized current. As can be seen, for any value of the current there is a critical value of losses, above which the self-excitation is impossible at any length. This is the case when the
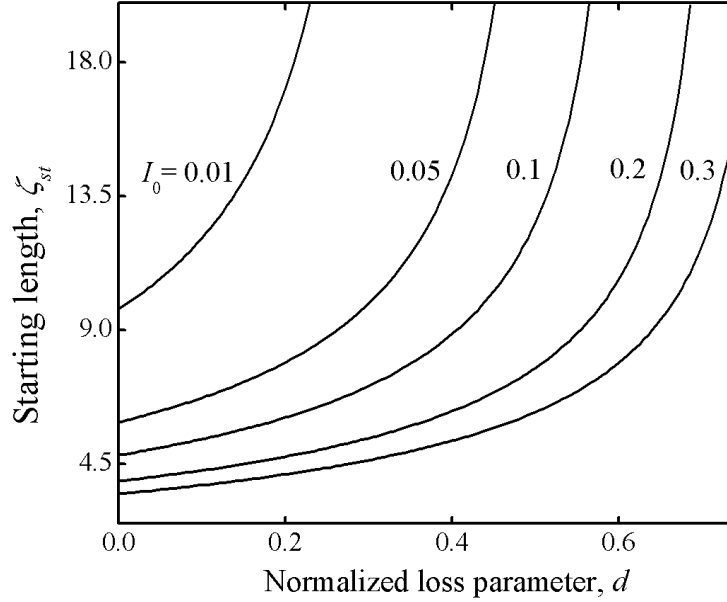
Fig. 1.10. The starting length of a lossy waveguide as the function of the loss parameter d for several values of the normalized beam current.

attenuation rate caused by losses is higher than the beam-induced growth rate of the wave.

At the next stage of our studies we applied our method to the analysis of the BW excitation in the NRL gyro-TWT. The dispersion curves for the operation TE_{11} mode and two parasitic waves are shown in Fig. 1.11, also showing the cyclotron beam lines for resonances at the first three cyclotron harmonics ($s = 1$, 2 and 3). The case of grazing for the operating wave at the fundamental resonance corresponds to the external magnetic field $B_0 = 12.08$ kG. As can be seen from this figure, the TE_{21} mode can be excited at the second harmonic closer to cut-off than other modes in the region of the backward wave interaction ($k_z < 0$). Therefore, it can be expected to be the most troublesome parasite. Indeed, the analysis of BW self-excitation conditions

showed that for this mode the normalized beam current parameter I_0 is equal to 0.0137 and the normalized lengths of the first and second waveguide sections are
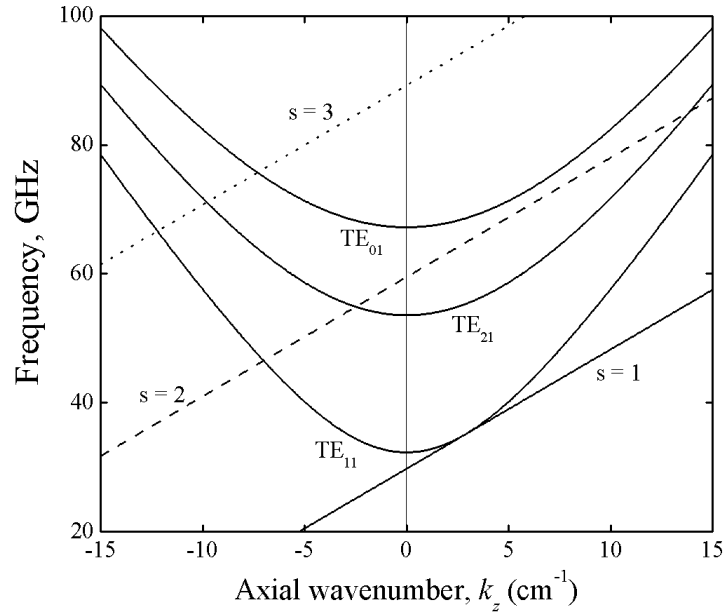
Fig. 1.11. Dispersion diagram for the operating TE_{11}-mode and spurious TE_{21} and TE_{01}-modes for the NRL gyro-TWT design.

equal to 26 and 5.92, respectively. At the same time the starting length of the second, lossless section is equal to 7.3, i.e. it exceeds the real length by about 20% only.

For the backward TE_{11} wave at the second cyclotron harmonic the normalized lengths of two sections are equal to 14.0 and 3.2 and the normalized beam current parameter is 0.0029 only. Accordingly, the starting length of the second section is about 14.0, so there are huge safety margins.

35

1.3.3. Results of the nonlinear analysis

The self-consistent set of non-linear equations (1.1)-(1.3) was studied numerically. Results of the gyro-TWT efficiency analysis are shown in Figs. 1.12 and 1.13, which correspond to the case without losses and the one with distributed losses
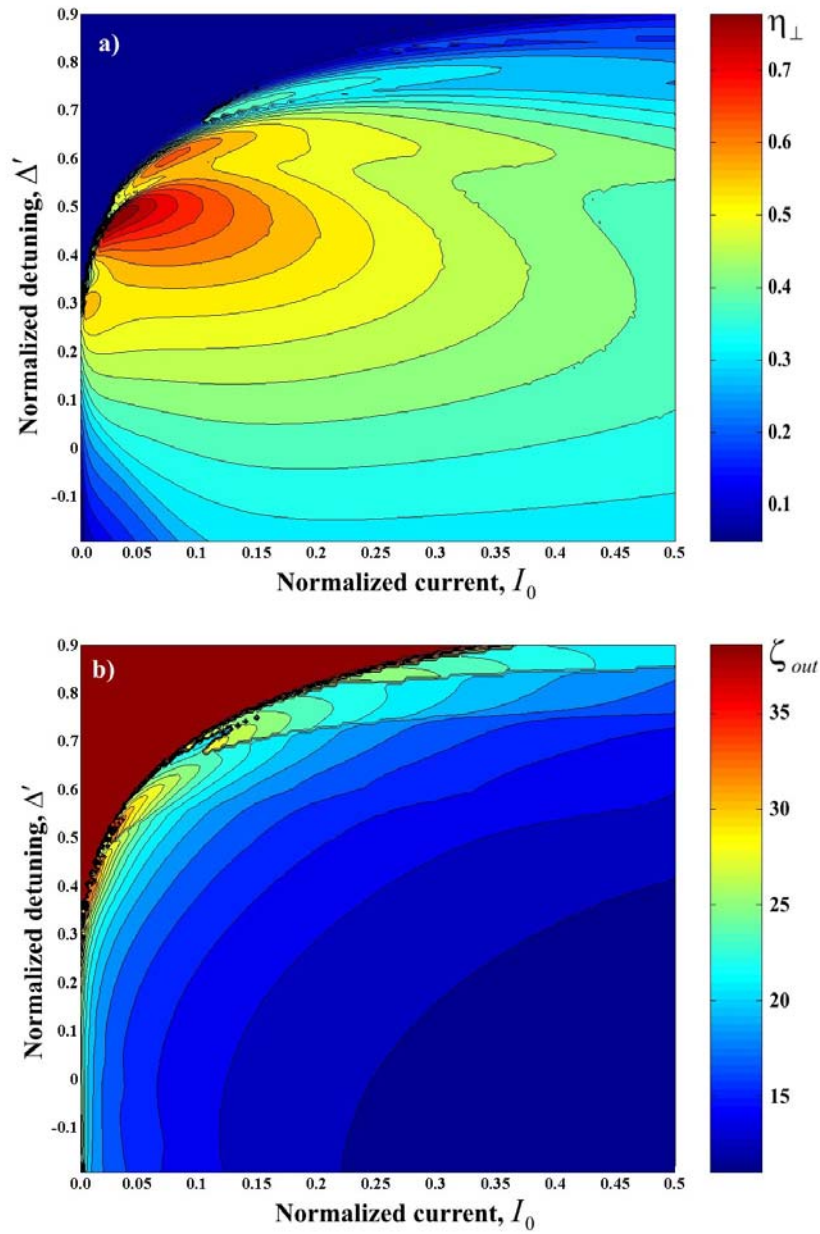
Fig. 1.12. Orbital efficiency of interaction (a) maximized over the length of the interaction space (b) for a lossless gyro-TWT.

in the first section of the tube, respectively. The length of the first section in the lossy case equals to 8.0 and the loss parameter d is equal to 0.4. These figures show the orbital efficiency of interaction $\eta_\perp$ maximized over the length of interaction space ζ_{out} (Figs. 1.12 (a) and 1.13 (a)) on the plane of normalized current parameter, I_0, and
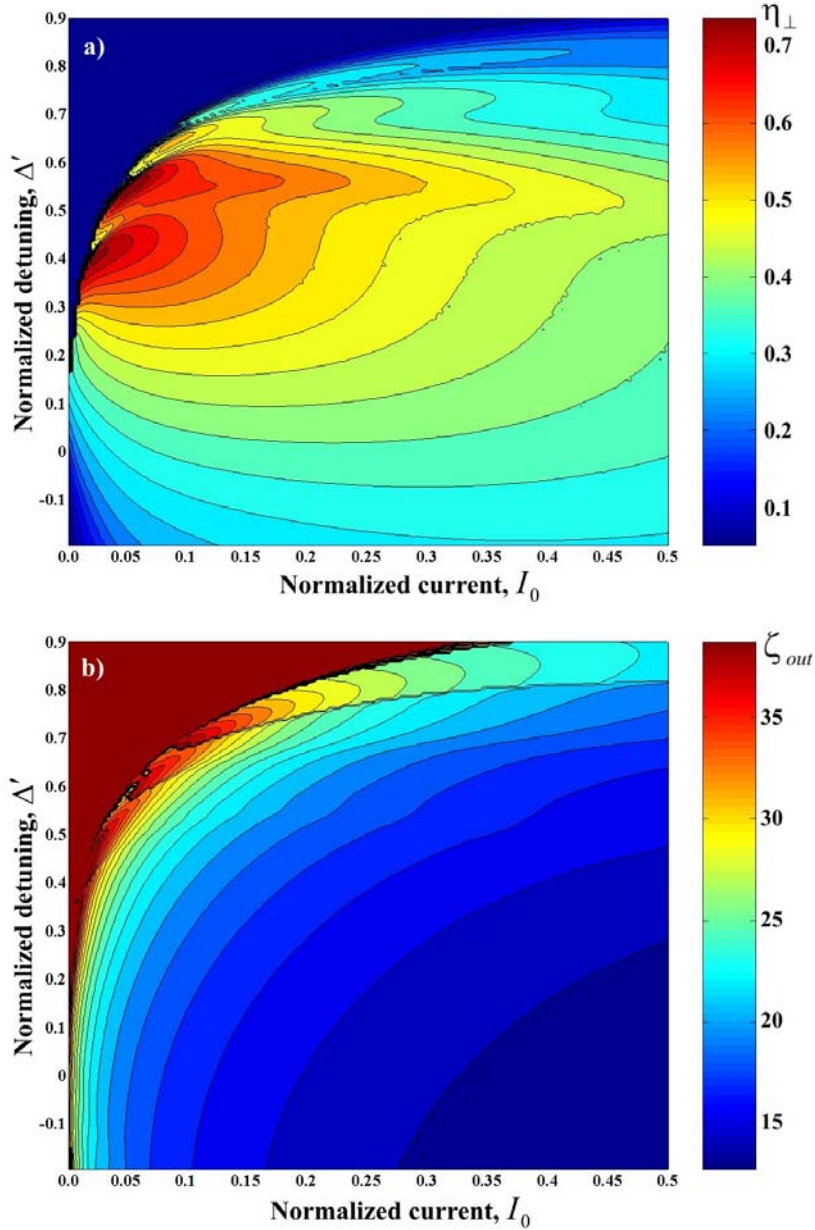
Fig. 1.13. Orbital efficiency of interaction (a) maximized over the length of the interaction space (b) for the two-stage gyro-TWT with distributed losses in the first section. The loss parameter d is equal to 0.4.

detuning, $\varDelta'$. The corresponding optimal values of ζ_{out} on the same parameter plane are shown in Figs. 1.12 (b) and 1.13 (b). As one may see, the maximum efficiency achieved is slightly lower in the presence of losses than in the lossless case, however the region of efficient operation is larger. This corresponds to the results obtained from the linear analysis, i.e. losses result in the increased effective bandwidth of the device (see Fig. 1.5).

The regions of maximum efficiency, however, do not coincide with the regions of maximum gain. This can be seen from Fig 1.14. showing the gain of a lossless two-stage gyro-TWT calculated for the parameters quoted above. The gain of the device grows with the increase of the normalized current, whereas the zones of maximum efficiency correspond to rather small values of the parameter. As discussed in the previous sections, stability problems may become critical at large values of I_0 and, therefore, care should be taken when selecting the parameters to provide the optimum
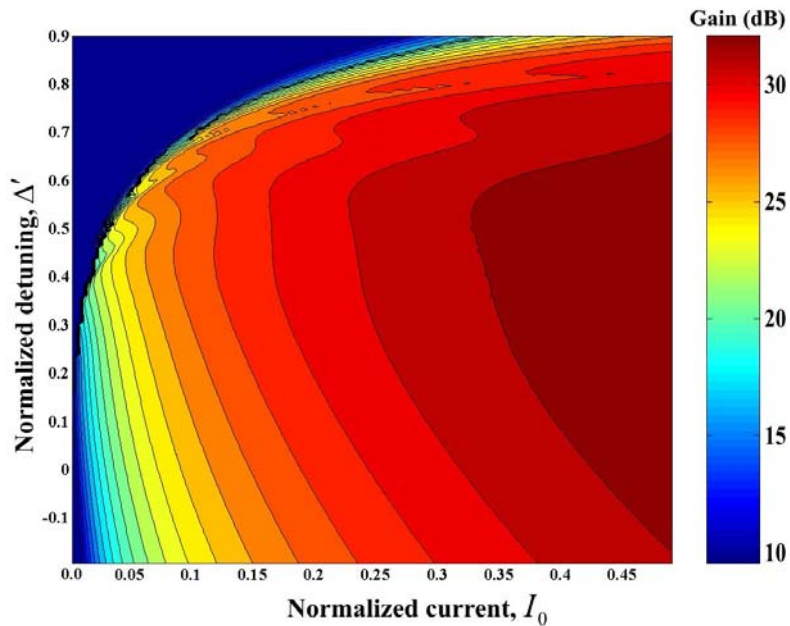
Fig. 1.14. Gain of the gyro-TWT maximized over the interaction length. Losses are not included.

operation. Moreover, the values of ζ_{out} shown in Figs. 1.12 (b) and 1.13 (b) were obtained without the analysis of BW self-excitation conditions, and hence the question of their choice remains open.

To analyze the effect of electron velocity spread on the device operation, one should consider a concrete device design since the number of parameters in the model increases and their choice cannot be arbitrary any more. Let us use the parameters of the NRL gyro-TWT described above. The effect of velocity spread on the amplifier bandwidth and output power is illustrated in Fig. 1.15. In this figure the output power is shown in dependence on the operating frequency for several values of the spread in orbital components of electron velocities. The driving power is constant for all the cases, being equal to 1.8 W. The 'triangular' velocity distribution function has been used in the computations, with RMS values of the spread indicated in the figure. As can be seen, there is a considerable degradation of power, gain and bandwidth as the
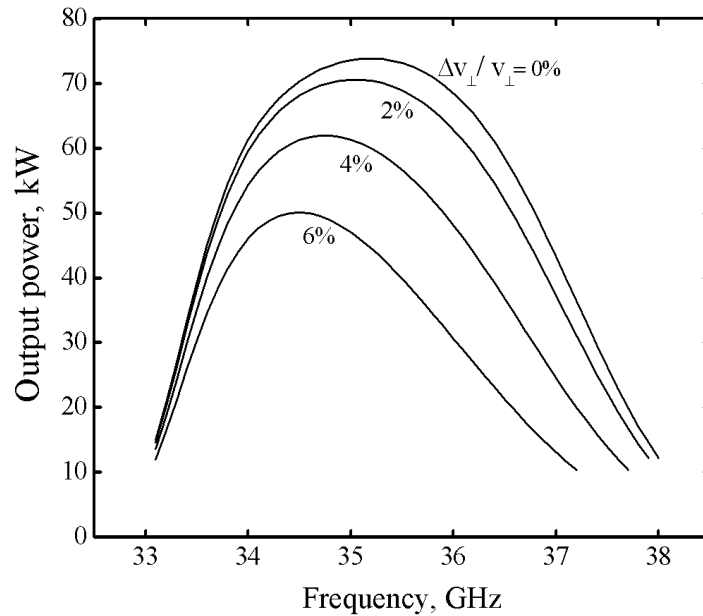
Fig. 1.15. Effect of orbital velocity spread for the NRL gyro-TWT. The RMS values of the spread are indicated in the figure. The driving power is equal to 1.8 W in all the cases.

amount of the spread is increased. It can also be noticed that the effect is relatively small at low frequencies, which are close to cutoff, while being better pronounced at the high frequency edge where the inhomogeneous Doppler broadening of the cyclotron resonance band (owing the axial velocity scatter) is much stronger.

We compared the results of our calculations with those obtained by MAGY as we did before in the linear analysis. First, only the uniform interaction region was considered with the input and output tapered sections ignored. Besides, the interaction with the operating TE_{11}-mode alone was analyzed. Fig 1.16 illustrates axial wave power profiles calculated by these two methods for three operating frequencies. Dependence of the output power upon the operating frequency is shown in Fig. 1.17. The two figures demonstrate a very good agreement between the results of the two approaches.

However, when the input taper (where the operating wave is partially converted into other modes) is included in MAGY simulations, a considerable difference between the results of the two approaches appears. As can be seen in Fig. 1.18, a good agreement exists between the axial power profiles at low frequencies (see Fig. 1.18 (a)) but the results diverge at high frequencies (Fig. 1.18 (b)). The agreement at low frequencies is observed in spite of the fact that MAGY predicts two minima in the axial dependence close to the input, whereas the theory predicts only one. At the same time, both methods yield only one minimum at high frequencies.

If, in the framework of our theory, we model the input downtaper by a waveguide section with a variable axial wavenumber, the theory also predicts two minima, as

40
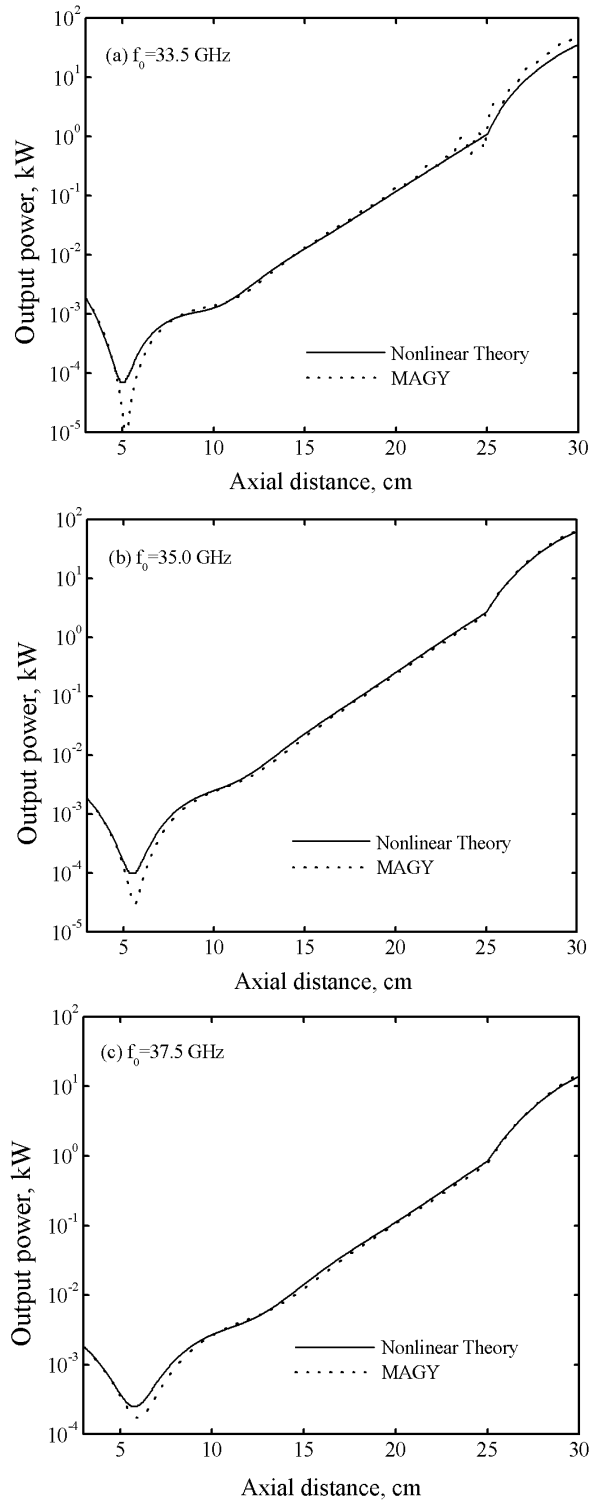
Fig. 1.16. Axial wave power profiles calculated for three operation frequencies by the use of nonlinear theory (solid) and MAGY (dotted). Only the uniform section of interaction space is analyzed. The driving power is equal to 1.8 W for all the cases.

41
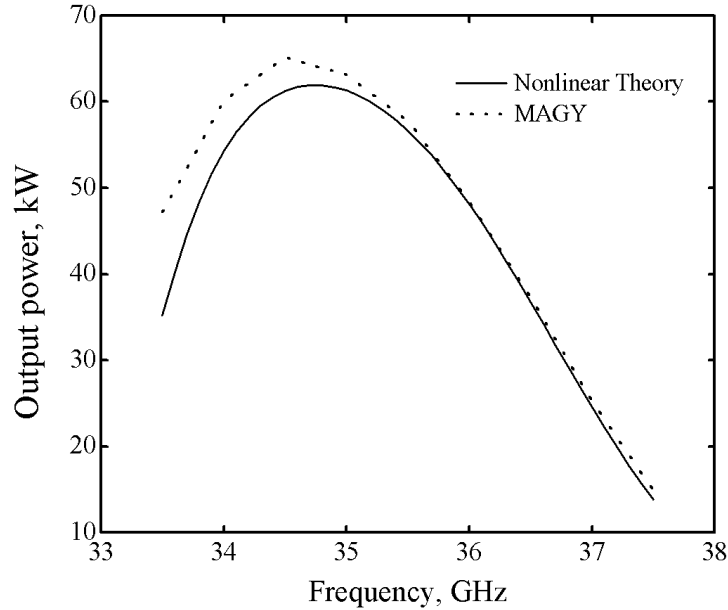
Fig. 1.17. Output power versus frequency obtained by nonlinear theory (solid) and MAGY (dotted). The uniform section of the interaction region is considered. The value of input power is equal to 1.8 W.

shown in Fig. 1.19 (a). However, MAGY yields a much higher power at low frequencies. As shown in Fig. 1.19 (b), the final gains are now in agreement at high frequencies only. The reason for the discrepancy at low frequencies can be attributed to the effects of interaction with backward waves that is ignored in our theory. In general, it is known that in the case of near cutoff operation wave excitation should be described by the second-order equation following from the wave equation, instead of the first-order equation (1.12) [49], [53]. In our case, the presence of the input downtaper where the input wave is partially reflected into a backward wave, makes this effect even more pronounced. A certain role can also belong to mode conversion in tapers, which effects have been ignored in the simple theory. As can be seen from

42
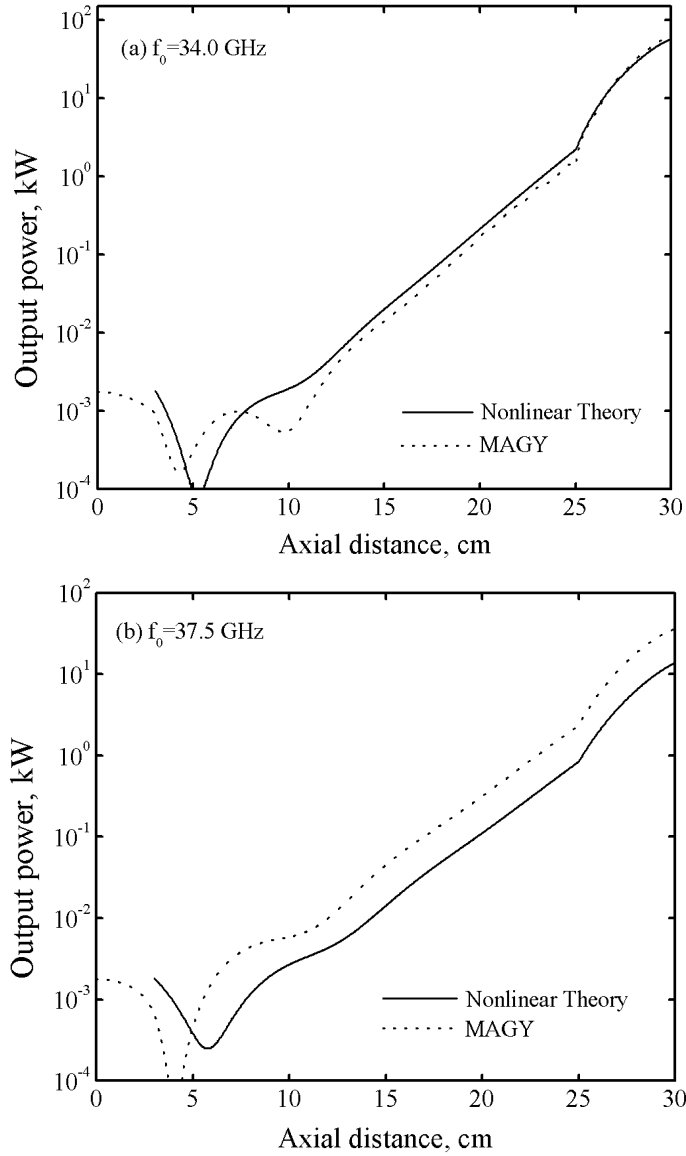
Fig. 1.18. Axial wave power profiles obtained at high and low frequencies. The input downtaper is included in MAGY simulations. The driving power is equal to 1.8 W. Fig. (a) shows that MAGY predicts two minima near the input.

Fig. 1.20, the level of the parasitic TE_{12} mode in the input and output taper regions is substantially higher than in the regular part of the structure. In order to reduce the effect of reflection, we considered the input taper with the angle of tapering $\delta = 0.51°$. (Accordingly, the initial radius of the waveguide was reduced from 3.248
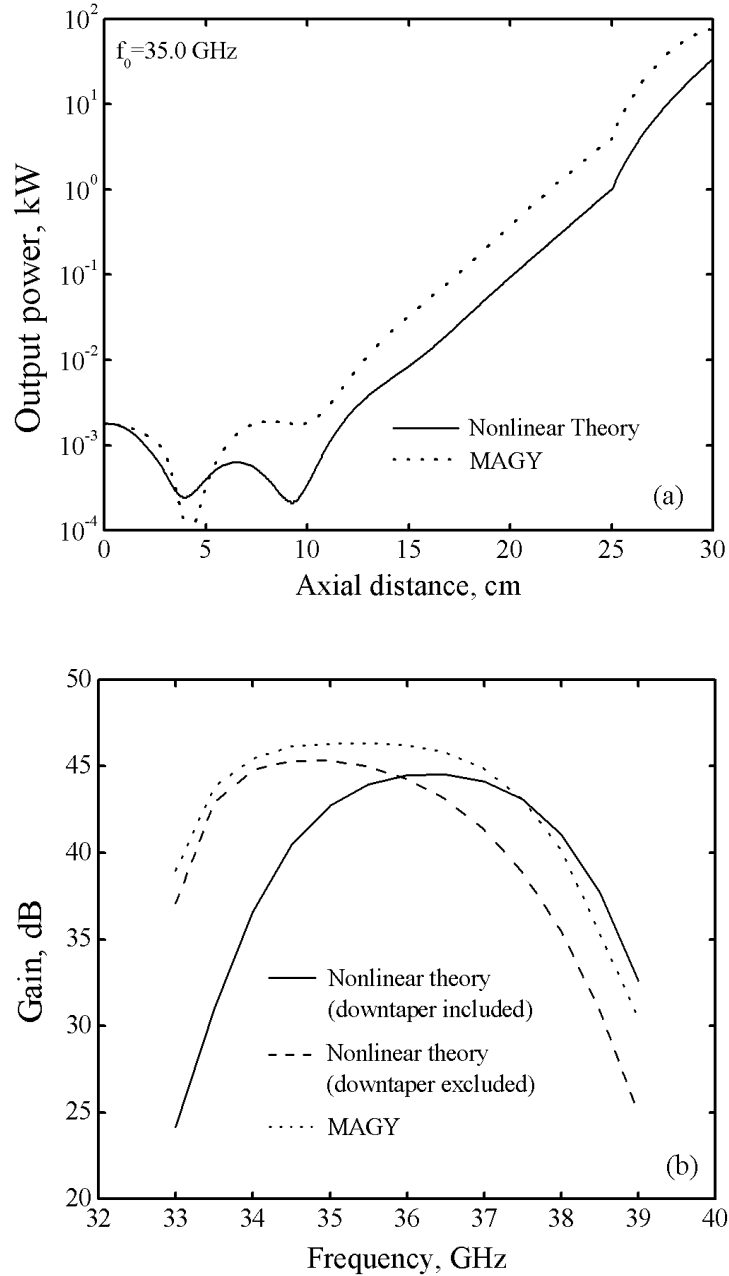
Fig. 1.19. (a) Axial wave power profiles for the central operation frequency. Nonuniform input section is taken into consideration both in the theory and in MAGY calculations. (b) Gain versus frequency calculated by the two methods. The curve corresponding to the case without input section in the theoretical calculations is shown for comparison. The input power is equal to 1.8 W.

44
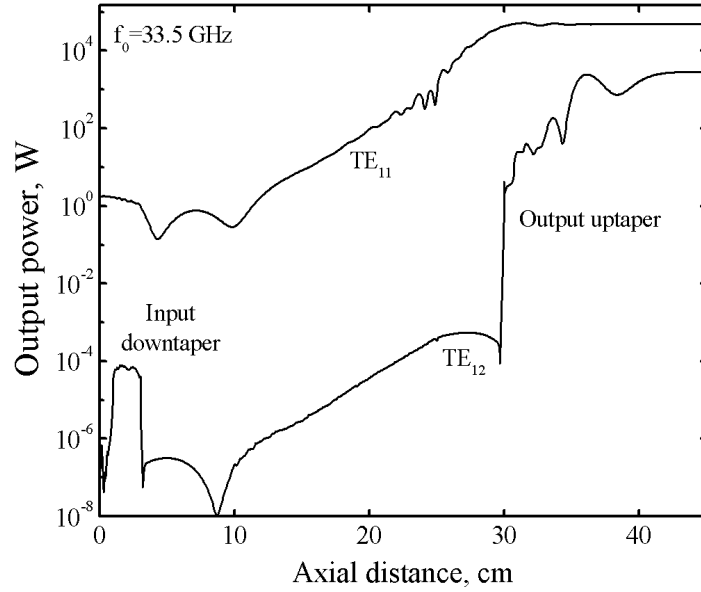
Fig. 1.20. Axial wave power profiles obtained by MAGY for dominant TE_{11} and parasitic TE_{12} modes. Larger magnitudes of the TE_{12} mode in the input and output tapered sections can be observed.
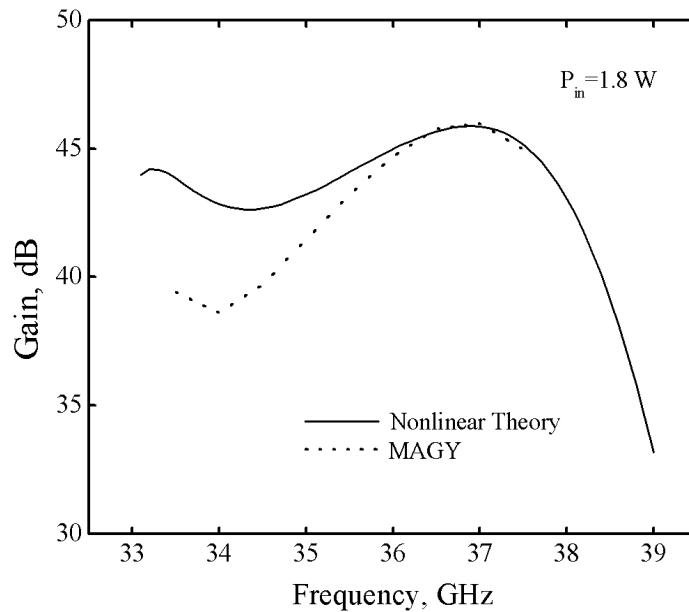
Fig. 1.21. Gain versus frequency for the case of reduced taper angle in the input section. MAGY predicts a considerable oversaturation at low frequencies in comparison with the theoretical results. The driving power is equal to 1.8 W.

45
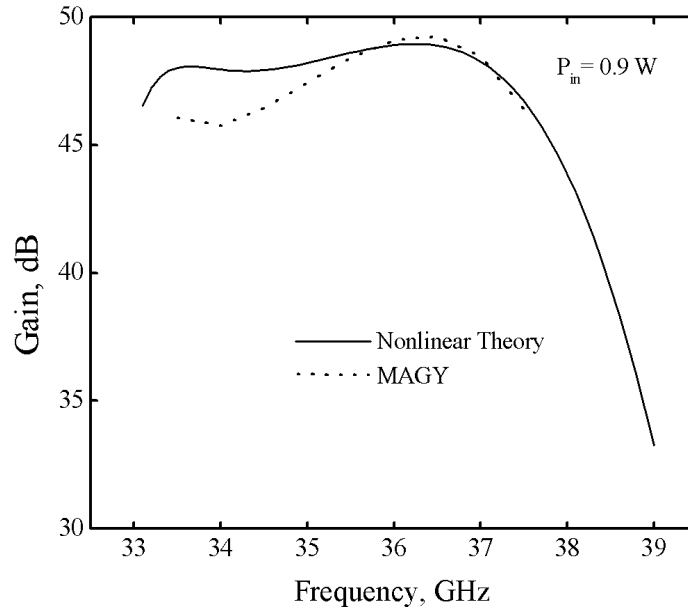
Fig. 1.22. Gain versus frequency for the case of reduced taper angle in the input section. Lower input power decreases the effect of oversaturation observed in MAGY results.

mm to 2.9 mm.) The results shown in Fig. 1.21 indicate this measure to have reduced the disagreement between the results of the two approaches. In particular, at high frequencies the agreement is very good. However, the MAGY prediction for low frequencies is a considerable oversaturation, possibly because the beam interacts strongly with both the forward and backward waves in the input taper of a smaller radius. To eliminate this additional effect, the input power was cut down from 1.8 W to 0.9 W. As shown in Fig. 1.22, the result is a reasonable agreement between the two approaches.

1.4: Theory of the gyro-TWT with tapered parameters

As mentioned in the previous sections, the theory of gyro-TWTs and gyro-BWOs with constant parameters has been developed a long time ago. The nonlinear theory of gyro-BWO with tapered waveguide radius and external magnetic field was presented in Ref. 54. In that paper, it was shown that for the case of linear tapering the maximum orbital efficiency of the gyro-BWO could be almost three times higher than that of the tube without tapering. However, so far, the nonlinear theory of the gyro-TWT with tapered parameters has not been developed in a similar form. In the present work, the author makes an attempt to start developing such a theory.

1.4.1: General formalism

Let us restrict our consideration to the case of a small tapering of the waveguide radius and/or external magnetic field. In this case, the effects of tapering can be taken into account in the cyclotron resonance mismatch Δ and the beam current parameter I_0 only. For the simplest case of linear tapering of the waveguide radius

$$R_w(z) = R_{w0}(1 + \delta_R \frac{z}{z_{out}}) \tag{1.24}$$

the corresponding changes of the normalized wavenumbers have the form:

$$\kappa(z) \simeq \kappa_0(1 - \delta_R \frac{z}{z_{out}}), \quad h(z) \simeq h_0(1 + \frac{\kappa_0^2}{h_0^2}\delta_R \frac{z}{z_{out}}), \tag{1.25}$$

where κ_0 and h_0 are, respectively, the transverse and axial wavenumbers at the waveguide entrance, δ_R is the waveguide taper parameter ($\delta_R \ll 1$) and z_{out} is the waveguide length. These expressions are valid under the assumption that the device operates far enough from the cutoff. Correspondingly, the cyclotron mismatch given by (1.4) can be represented as

$$\Delta(z) \simeq \Delta_0 - \frac{\delta_R}{b_0} \frac{z}{z_{out}},$$

(1.26)

where $b_0 = h_0 \beta_{\perp 0}^2 / 2\beta_{z0}(1 - h_0\beta_{z0})$ is the recoil parameter at the entrance. This parameter is small when the operating voltages are relatively low and the operation is not too far from the cutoff ($\pi / z_{out} \ll k_{z0} \ll \omega/c$) [48]. Therefore, when δ_R and b_0 are of the same order of magnitude, the changes in the cyclotron mismatch can be large and comparable with its initial value. In other words, even small tapering of the waveguide radius may bring to significant changes in the device performance due to variation in the cyclotron resonance conditions.

The normalized current parameter in the similar manner can be expanded as

$$I_0(z) = I_{0,in}(1 - \delta_I \frac{z}{z_{out}}),$$

(1.27)

where $I_{0,in}$ is the current parameter at the entrance and

$$\delta_I = \delta_R \left(\frac{\kappa_0^2}{h_0^2} + 3\frac{\beta_{z0}\kappa_0^2}{h_0(1 - h_0\beta_{z0})} - 4 \right).$$

(1.28)

(This expression has been obtained for the case of operation at the fundamental harmonic, $s = 1$).

48

The tapering of the external magnetic field brings to the changes in the cyclotron frequency, $\Omega_0 = eBc / \mathcal{E}$ and, therefore, in the detuning parameter only. For the case of parabolic tapering, $B(z) = B_0(1 - \delta_B z^2 / z_{out}^2)$, which describes the axial dependence of the real field rather accurately, the cyclotron mismatch takes the form

$$\Delta(z) = \Delta_0 + s \frac{\Omega_{0,in}}{\omega \mu_0} \delta_B \frac{z^2}{z_{out}^2}, \qquad (1.29)$$

where $\Omega_{0,in}$ is the cyclotron frequency at the entrance, $\mu_0 = \beta_{\perp 0}^2(1 - h_0^2) / 2(1 - h_0 \beta_{z0})$ and δ_B is the magnetic field taper parameter. The expression (1.29) is written in the exact form and therefore δ_B is not necessarily a small parameter. It can be noticed that when both waveguide and magnetic field tapers are used, the corresponding changes in the detuning parameter can to some degree compensate for each other due to their opposite signs.

Since b_0, δ_I μ_0 and $\Omega_{0,in}$ depend upon specific device parameters, viz. h_0, κ_0, β_{z0}, R_0 and B_0, and, therefore, there exists a relationship between them, it is quite problematic to carry out the analysis of the tapering effects in a general way. Instead, design parameters of a concrete device should be considered, which will be done in the next section.

1.4.2: Results of the numerical analysis

The author analyzed a gyro-TWT operating at about 250 GHz. To obtain its parameters, the design of the Ka-band gyro-TWT described in section 1.3.1, typical gun parameters for this frequency and the scaling properties of the equations (1.1)-(1.3) were used. The set of parameters obtained is the following:

Operation frequency…………………………………………..250 GHz

Operation mode………………………………………………TE_{01}

Beam voltage…………………………………………………….20 kV

Beam current…………………………………………………….1 A

Radius of electron guiding centers…………………………...0.037 cm

External magnetic field value……………………………....87 kG

Initial waveguide radius……………...…………………….0.076 cm

Waveguide length…………………………………………….6.725 cm

Length of the lossy section in the waveguide…………….…..5.5 cm

The dependences of the cyclotron detuning and normalized current parameters upon the axial coordinate for the four frequency values and fixed waveguide taper parameter $\delta_R = 0.01$ are shown in Fig. 1.23. The expressions (1.4) and (1.5) were used in these calculations. Also, for the purpose of comparison, shown are the curves calculated by the use of expressions (1.26) and (1.27) (dashed lines). As one may see, the changes in the detuning parameter can be described quite well by the expression (1.26) even close to cutoff ($f_{cut} = 240.6$ GHz), whereas the normalized current at these
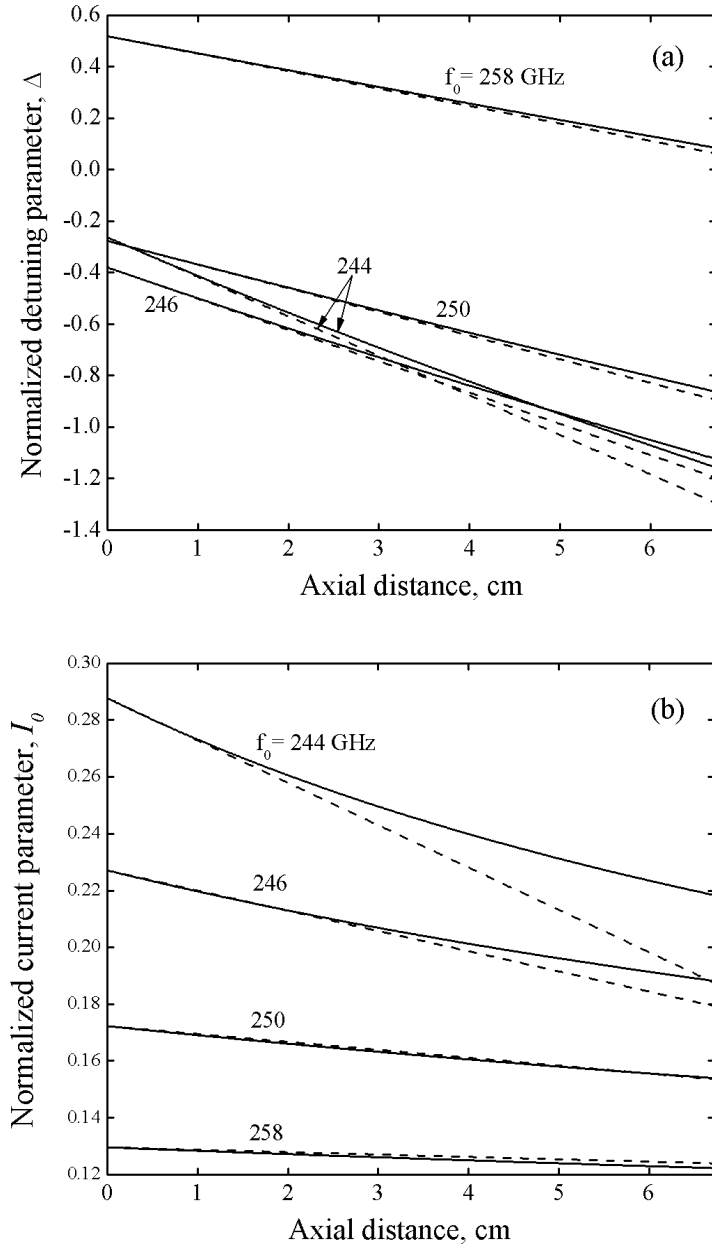
Fig. 1.23. Axial dependences of (a) the cyclotron detuning and (b) the normalized current current parameters for several frequency values. The waveguide taper parameter is equal to 0.01 in all the cases. Solid and dashed lines correspond to the results obtained by the use of expressions (1.4), (1.5) and (1.26), (1.27), respectively.

frequencies demonstrates strongly nonlinear behavior and the expression (1.27) proves to be inaccurate. Second-order small terms should be used in the expansion of I_0. It can be seen in Fig. 1.23 (a) that the absolute values of the detuning parameter at the exit of the device are at least three times larger than those at the input even for the central frequency of operation. The normalized current parameter in Fig. 1.23 (b) experiences significant changes only near the cutoff.

After these preliminary calculations, the contours of gain, bandwidth and gain-bandwidth products were obtained on the plane of taper parameters δ_R and δ_B for several values of input power, pitch-angle and initial magnetic field. The maximum gain values were found in the operational frequency range and bandwidths were estimated for these optimized values. The contours shown in Fig. 1.24 are obtained for the following set of parameters: $P_{in} = 100$ mW, $\alpha = 0.8$, $B_0 = 87.5$ kG. Figure 1.24 (a) shows gain in dB, Fig. 1.24 (b) shows bandwidth per cent and Fig. 1.24 (c) demonstrates the gain-bandwidth product in dB·GHz for the values of taper parameters specified on the figure axes. As can be seen, the maximum gain achieved is about 47 dB, which corresponds to the largest tapering of the magnetic field, $\delta_B = 0.04$. The waveguide taper parameter for this point is equal to 0.026. However Fig. 1.24 (b) shows that the corresponding bandwidth value is about 2% only. Contrary to the gain, the largest bandwidth (about 6.5%) is obtained for the case of constant magnetic field ($\delta_B = 0$) and for the waveguide taper parameter $\delta_R \approx 0.035$. Although such a discrepancy exists, the main factor that determines the gain-bandwidth product on the parameter plane is the bandwidth behavior. This can be seen in Fig. 1.24 (c), which shows that the gain-bandwidth product reaches its
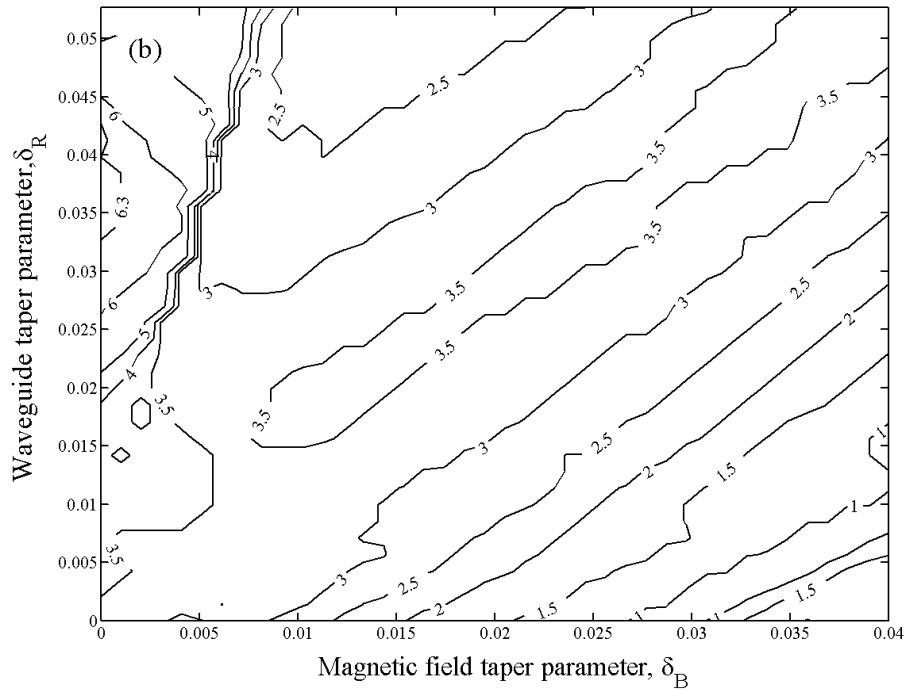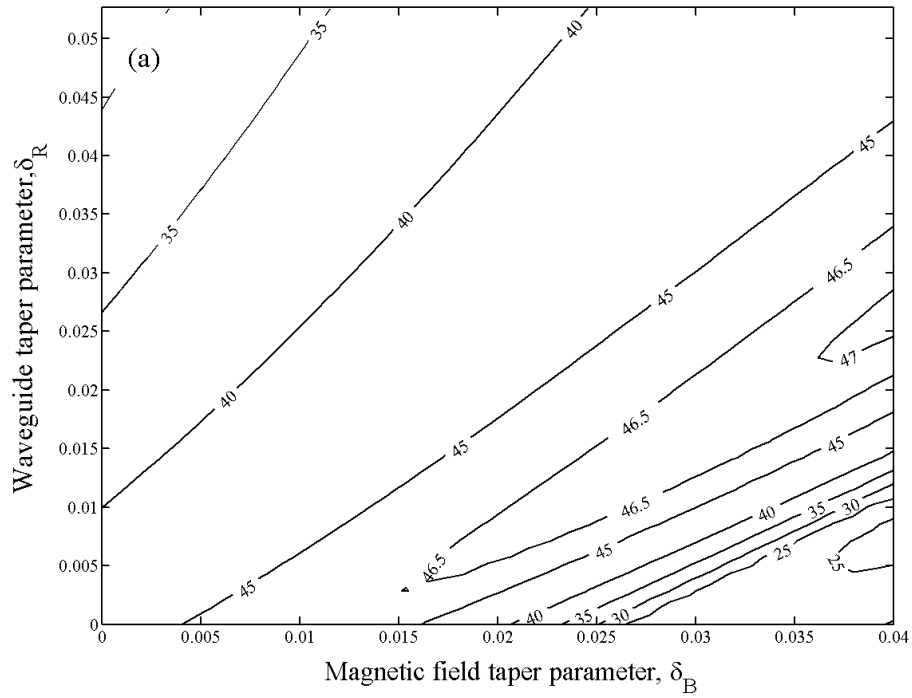
Fig. 1.24. (a) Optimized gain, (b) bandwidth and (c) gain-bandwidth product on the plane of taper parameters. The figures are obtained for the following set: $P_{in} = 100$ mW, $\alpha = 0.8$, $B_0 = 87.5$ kG. The optimum point for gain-bandwidth product corresponds to $\delta_B = 0$ and $\delta_R \approx 0.032$.
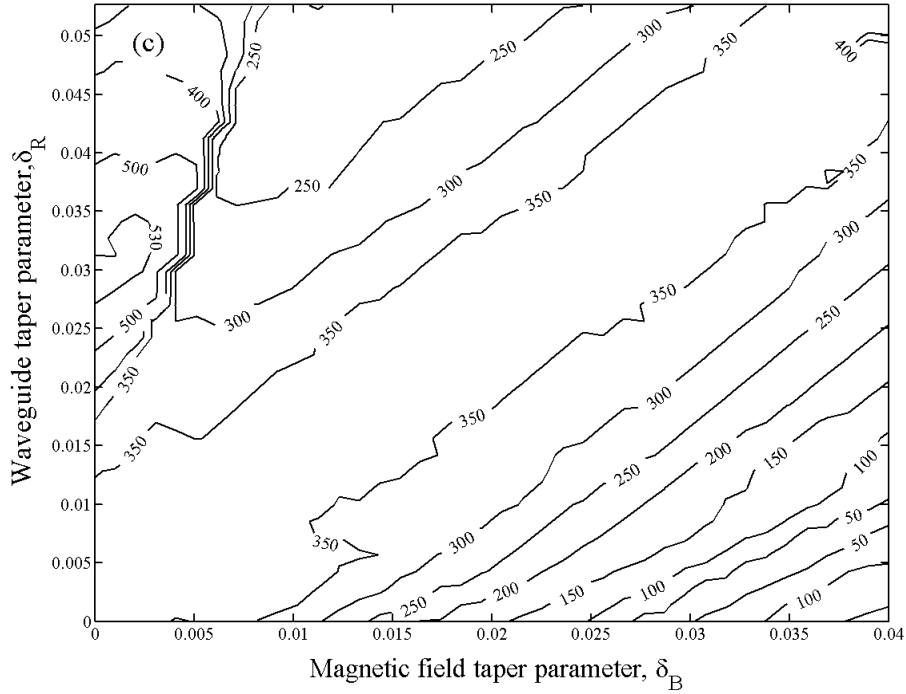
Fig. 1.24. (cont.)

maximum near the optimum bandwidth point and is about 540 dB·GHz. One may

conclude from these results that it is possible to significantly increase the bandwidth

and gain-bandwidth product of the device by tapering the waveguide radius only.

It is expedient to consider the dependences of gain and bandwidth upon the

magnetic field near the optimum point. These are shown in Figs. 1.25 and 1.26,

respectively, for two values of input power. Also, in Fig. 1.25, shown are the

frequencies that correspond to the optimum gains (dashed lines). As on may see,

higher gain and larger bandwidth can be achieved at lower driving powers since the

saturation effects for those are less pronounced. The sharp drops on the curves near

$B_0 = 88$ kG in Fig. 1.26 are caused by the presence of a valley on the corresponding

frequency dependences. The valley near this magnetic field value becomes deeper

than 3 dB, which brings to bandwidth collapse. This can be clearly seen in Fig. 1.27,

54
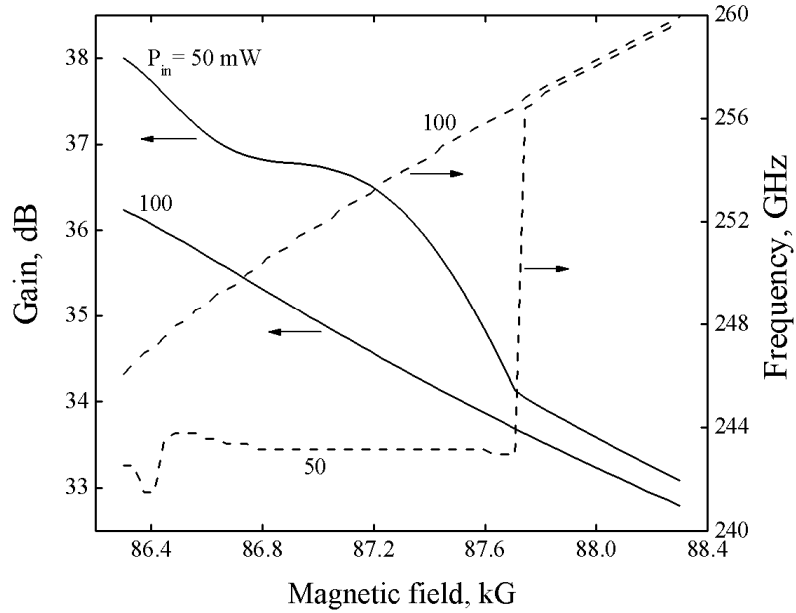
Fig. 1.25. Optimized gain (solid) and corresponding frequency values (dash) as functions of the magnetic field. The results are shown for two input power values indicated in the figure. The waveguide taper parameter is equal to 0.03 in all the cases.
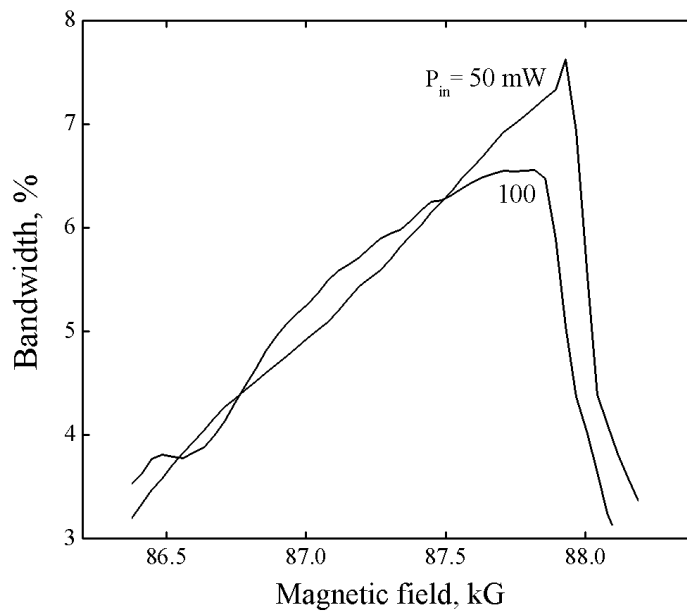
Fig. 1.26. Bandwidths estimated for the optimum gain as functions of the magnetic field. The results are shown for two values of input power indicated in the figure. The waveguide taper parameter is equal to 0.03.
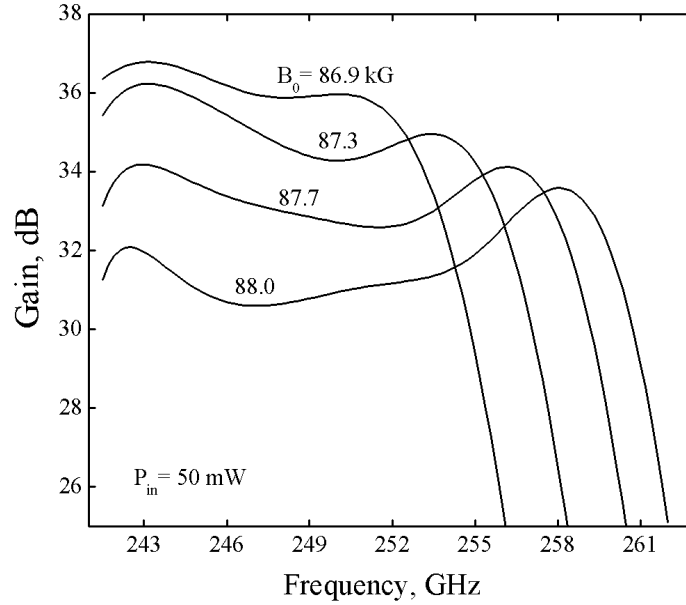
Fig. 1.27. Gain versus frequency for several values of
the magnetic field. The waveguide taper parameter is
equal to 0.03, the input power is indicated in the figure.

which shows frequency characteristics for the four values of B_0. The input power
equals to 50 mW in all the cases. Also, one may notice in this figure that the
maximum gain value shifts from lower frequencies to higher ones with the increase of
B_0. This shift causes a jump on the curve of optimum frequencies for the case of $P_{in} =$
50 mW (see Fig. 1.25).

The author has also analyzed the dependence of gain-bandwidth product upon
the electron orbital-to-axial velocity ratio, α. The results are shown in Fig. 1.28 for
the same input power and $B_0 = 87.8$ kG. One may see, that by going from $\alpha = 0.7$ to
$\alpha = 0.8$ the gain-bandwidth product (solid line) changes its value from approximately
45 to 610 dB·GHz, i.e. it gets increased by almost 13.6 times. Also, in this figure, the
gain-bandwidth product for the tube without tapering is shown (dashed line) for the
sake comparison. All other device parameters are the same as for the device with
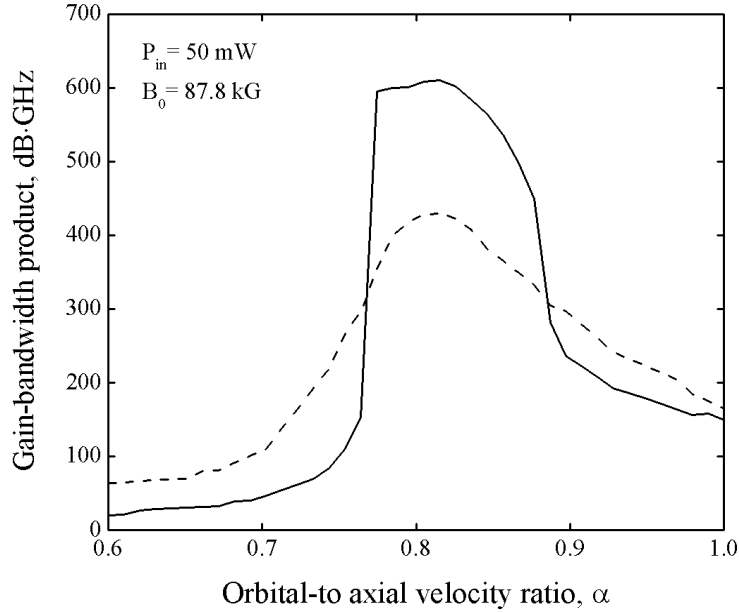
Fig. 1.28. Gain-bandwidth product for the tapered (solid) and untapered (dash) gyro-TWT as functions of the orbital-to-axial electron velocity ratio. The input power and magnetic field values are indicated in the figure.

tapering in this example. It can be seen that the corresponding increase in the gain-bandwidth product is 4 times only (from approximately 150 to 422 dB·GHz) for this case. Also, smaller gain-bandwidth product in the narrower range can be obtained for the untapered device for the same values of α considered. So, although the tapering allows one to increase the maximum gain-bandwidth by ~50%, this effect exists in a relatively narrow range of α's: from $\alpha \simeq 0.77$ to $\alpha \simeq 0.88$.

Here, the author has studied the effect of simple linear tapering of the waveguide wall radius and parabolic tapering of the magnetic field on the gyro-TWT performance. It has been shown that tapering of the waveguide radius alone may significantly increase the gain-bandwidth product of the device, which is a figure of merit for most of the gyroamplifiers nowadays. Obviously, other, optimized nonlinear

57

types of tapering can make better showing but their analysis is beyond the scope of this work.

Chapter 2: Theory of Multi-Stage Gyroklystrons

2.1: Basic device configurations

The schematic of a simple two-cavity gyroklystron is shown in Fig. 2.1. Very often, to improve the characteristics of a GKL, a larger number of cavities is employed. The interaction between the electron beam and the EM-wave occurs in the cavities separated by drift regions in which wave propagation is impossible. The input cavity is excited by an input signal. The EM-field in this cavity modulates the energy
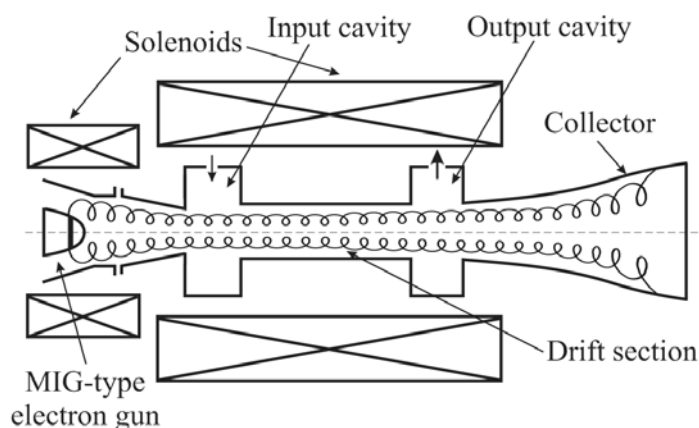
Fig. 2.1. Typical configuration of a two-cavity gyroklystron.

of electrons that, in accordance with (I.2), leads to their gyration with slightly different cyclotron frequencies and results in the electron phase orbital bunching, which proceeds when electrons move along the device axis in the drift sections. These modulation and bunching processes cause an appearance of high-frequency components at the signal frequency and its harmonics in the electron current density. One of these high-frequency components excites oscillations in the subsequent cavities that improve the quality of electron bunches and increase the gain and

59

efficiency. The microwave power is extracted from the output cavity. When the output cavity is excited by one of harmonics of the signal frequency, the device operates in the frequency multiplication regime.

The configuration of a clustered-cavity GKL is shown in Fig. 2.2. This is a four-cavity three-stage device, in which the first and last stages are represented by
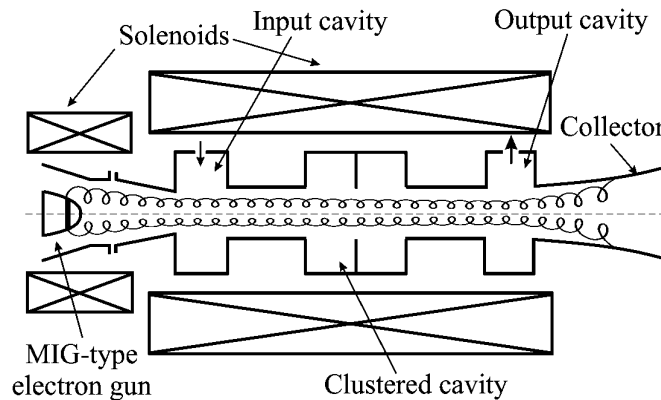
Fig. 2.2. Schematic of a three-stage clustered-cavity gyroklystron.

single cavities, while the intermediate stage is a cluster consisting of two cavities. The concept of clustered cavities was originally suggested by R. Symons for conventional linear beam klystrons for improving their bandwidth characteristics [56], [57].

It should be mentioned that there is no limitation for the number of cavities in the cluster, and the use of multiplets is also possible. The location of clusters is not limited by the intermediate sections, the input and output stages may also contain clustered cavities [35]. In this work the author considers the scheme shown in Fig. 2.2 with two cavities in the cluster located in the intermediate section of the device and compares this scheme with a standard 4-cavity GKL.

2.2: General formalism

2.2.1: Gyro-averaged equations of electron motion and the balance equation

We will ignore space charge effects and velocity spread in the electron beam and ignore the effect of the beam on the axial structure of the cavity field (cold-cavity approximation, cf. [55]). Also, negligible cross-talk between the cavities in each cluster is assumed when the clustered-cavity configuration is considered. Therefore, the electron motion in each cavity can be described by two equations, one for normalized magnitude of the orbital momentum p and another for the slowly varying gyrophase of gyrating electron relative to the rf field, ϑ [8], [34]:

$$\frac{dp}{d\zeta} = p^{s-1} \operatorname{Re}\{F_l f_l \exp(is\vartheta)\} \tag{2.1}$$

$$\frac{d\vartheta}{d\zeta} - \Delta + 1 - p^2 = p^{s-2} \operatorname{Re}\{iF_l f_l \exp(is\vartheta)\} \tag{2.2}$$

Here ζ is the normalized axial coordinate, $\Delta = (2/\beta_{\perp 0}^2)(1 - s\Omega_0/\omega)$ is the normalized mismatch between the signal frequency or its harmonic and the resonant harmonic of the electron cyclotron frequency, s is the cyclotron harmonic number, F_l is the normalized amplitude of the *l*-th cavity field and the function $f_l(\zeta)$ describes the axial structure of this field. Let us designate each cavity by two indices among which the first one, k, indicates the cluster number and the second one, l, refers to the number of a cavity in a given cluster. However, when single cavities are considered, we will be ignoring the second index in such notation. The susceptibility of the

electron beam with respect to the resonator field can be obtained by integrating Eqs. (2.1) and (2.2) with corresponding boundary conditions:

$$\chi_{k,l} = -\frac{2i}{F_{k,l}} \int_{\zeta_{k,l,in}}^{\zeta_{k,l,out}} f_{k,l}^* \left\{ \frac{1}{2\pi} \int_0^{2\pi} \left(pe^{-i\vartheta} \right)^{s_{k,l}} d\vartheta_0 \right\} d\zeta \qquad (2.3)$$

Here $\zeta_{k,l,in}$ and $\zeta_{k,l,out}$ correspond to the input and the output of a given cavity, respectively, and ϑ_0 is the initial gyrophase homogeneously distributed at the entrance to the first cavity between 0 and 2π. The functions $f_{k,l}(\zeta)$ in Eqs. (2.1)-(2.3) are normalized in such a way that $\int_{\zeta_{k,l,in}}^{\zeta_{k,l,out}} f_{k,l} d\zeta = 1$. The susceptibility of the electron beam, χ, its conductivity, σ, and the dielectric constant, ε, are related as [8]

$$\varepsilon = 1 + 4\pi I_0 \chi = 1 - i4\pi\sigma / \omega$$

(I_0 is the normalized current parameter specified below).

In the stationary regime, the amplitude and phase of a resonator field $F_{k,l} = |F_{k,l}| \exp(i\psi_{k,l})$ can be found from balance equations. For the first cluster (or single cavity) they can be written as

$$F_{k,l} \left\{ 1 + \delta_{k,l} + iI_{0(k,l)}\chi_{k,l} \right\} + A_l = 0. \qquad (2.4)$$

Here A_l is the complex amplitude of the field excited in the l-th cavity by the driver, I_0 is the normalized current parameter, which is proportional to the beam current and to the Q factor of a given cavity

$$I_0 = \frac{eI}{mc^3\gamma_0} Q \left(\frac{s^s}{(s-1)!} \right)^2 \beta_\perp^{2(s-3)} 4^{2-s} \frac{J_{m\mp s}^2(k_\perp R_0)}{(\nu^2 - m^2)J_m^2(\nu)\int |f|^2 dz'}, \qquad (2.5)$$

where $z' = \omega z / c$ and ν is the eigenvalue, which for a $TE_{m,p}$ mode of a cylindrical cavity is the *p*-th root of the equation $J'_m(\nu) = 0.$

As there is no input power for other cavities, the balance equations for them are:

$$I_{0(k,l)} \chi''_{k,l} = 1, \quad I_{0(k,l)} \chi''_{k,l} = -\delta_{k,l} \qquad (2.6)$$

In Eqs. (2.4) and (2.6) the detuning parameter $\delta_{k,l}$ is the mismatch between the signal frequency or its corresponding harmonic and the cold-cavity frequency $\omega_{k,l}$ normalized to the width of the resonance curve of this cavity:

$$\delta_{k,l} = \frac{\omega - \omega_{k,l}}{\omega_{k,l} / 2Q_{k,l}}. \qquad (2.7)$$

The expression for the gain describing the signal amplification in the *l*-th cavity of the *k*-the cluster can be given as

$$G = 10 \log \left\{ \frac{1}{A^2} \sum_{l=1}^{L_k} | F_{k,l} |^2 \right\}, \qquad (2.8)$$

where $A^2 = \sum_l A_l^2$ is the total intensity of the field excited in the input cluster or single cavity by the driver. This intensity for the case of single input cavity relates to the power of the driver, P_{dr}, as

$$A^2 = \frac{4 I_{01} P_{dr} Q_1}{P_{0\perp} Q_{cpl}}.$$

Here Q_1 is the loaded Q factor of this cavity, Q_{cpl} is the coupling or external Q factor of the drive cavity, $P_{0\perp} = \eta_{sp} V_b I_b = [\beta_\perp^2 / 2(1 - \gamma_0^{-1})] V_b I_b$ is the beam power associated with the electron gyration and V_b and I_b are the beam voltage and current, respectively.

2.2.2: Point-gap model

As known, in gyroklystrons as well as in conventional klystrons the drift regions are much longer than the cavities. The 'point-gap' model is the limiting case of very short cavities. We will assume that the total length of each cluster consisting of a number of closely located short cavities is also very small. Therefore, the electron phase at the entrance to an arbitrary (k,l) cavity can be determined as [35]

$$\vartheta(\zeta_{k,l}=0)=\vartheta_0+\sum_{k'<k}\left[\Delta-1+p_{k'}^2(\mu_{k'})\right]\mu_{dr,k'}+\sum_{l'<l}\mathrm{Re}\left\{iF_{k,l'}\exp(i\vartheta_{dr,k-1})\right\} \quad (2.9)$$

Here $p_{k'}(\mu_{k'})$ is the electron momentum at the exit from the k'-th cluster and $\mu_{dr,k'}$ is the normalized length of the drift-section following the one. The term $\sum_{k'}\Delta\mu_{dr,k'}$ in the first sum of this expression describes the transit effect for electrons passing through all previous drift sections and the term $\sum_{k'}[1-p_{k'}^2(\mu_{k'})]\mu_{dr,k'}$ describes the cumulative ballistic bunching due to modulation of electron momentum in each cavity. The last sum in Eq. (2.9) describes the effect of previous cavities in a given cluster on the electron phase ($\vartheta_{dr,k-1}$ is the electron phase after passing $k-1$ clusters). The electron momentum at the entrance to the same cavity can be determined as

$$p(\zeta_{k,l}=0)=1+\sum_{k'\le k,l'<l_k}\mathrm{Re}\left\{F_{k',l'}\exp(i\vartheta_{dr,k'-1})\right\}. \quad (2.10)$$

By integrating the equations for electron motion (2.1) and (2.2) one may calculate the susceptibility given by Eq. (2.3) [34]:

$$\chi_{k,l} = -i - \frac{2i}{F_{k,l}} \sum_{l'<l} F_{k,l'} - \frac{2i}{F_{k,l}} \left\langle \exp(-i\vartheta_{dr,k-1}) \right\rangle. \qquad (2.11)$$

Here the first term on the RHS describes the beam loading effect, the second term describes the effect of preceding cavities in a given cluster. Notice that this term is absent in conventional gyroklystrons where $l=1$. The last term describes the effect of ballistic bunching (angular brackets denote averaging over ϑ_0). Equation (2.11) being combined with the balance equation (2.4) or with Eqs. (2.6) determines the amplitudes and phases of fields in all cavities. This yields for the input cluster or cavity:

$$|F_{1,l}|^2 = \frac{|\mathcal{F}_{1,l}|^2}{(1+I_{0(1,l)})^2 + \delta_{1,l}^2}, \qquad (2.12)$$

$$\tan(\phi_s - \psi_{1,l}) = \frac{\delta_{1,l}\mathcal{F}'_{1,l} - (1+I_{0(1,l)})\mathcal{F}''_{1,l}}{(1+I_{0(1,l)})\mathcal{F}'_{1,l} + \delta_{1,l}\mathcal{F}''_{1,l}}, \qquad (2.13)$$

where $\mathcal{F}'_{1,l}$ and $\mathcal{F}''_{1,l}$ are, respectively, the real and imaginary parts of the function

$$\mathcal{F}_{1,l} = |A_l| + 2I_{0(1,l)} \sum_{l'<l} |F_{1,l'}| \exp(i\psi_{1,l'} - i\phi_{sgn}), \qquad (2.14)$$

and ϕ_{sgn} is the phase of the signal $A_l \equiv |A_l| \exp(i\phi_{sgn})$. The field intensities and phases for other clusters are equal to

$$|F_{k,l}|^2 = \frac{4I_{0(k,l)}^2}{(1+I_{0(k,l)})^2 + \delta_{k,l}^2} |\mathcal{F}_{k,l}|^2 \qquad (2.15)$$

$$\tan(\phi_{sgn} - \psi_{k,l}) = \frac{\delta_{k,l}\mathcal{F}'_{k,l} - (1+I_{0(k,l)})\mathcal{F}''_{k,l}}{(1+I_{0(k,l)})\mathcal{F}'_{k,l} + \delta_{k,l}\mathcal{F}''_{k,l}}, \qquad (2.16)$$

where

$$\mathcal{F}_{k,l} = \left(\left\langle \exp(-i\vartheta_{dr,k-1}) \right\rangle + \sum_{l'<l} F_{k,l'} \right) \exp(-i\phi_{sgn}) \qquad (2.17)$$

65

2.3: Comparison of two concepts: Conventional multi-cavity
versus clustered-cavity gyroklystrons

The results of the analysis of clustered-cavity gyroklystrons were presented in Ref. 35. In that work, a two-cluster GKL with two cavities in each cluster was analyzed. The results were compared with the ones obtained for a conventional two-cavity GKL. It was shown that by using the clustered-cavity gyro-concept, the bandwidth of gyroklystrons could be significantly enlarged, the efficiency of the device could be the same as of conventional GKLs or even higher; also the gain in the device of a given drift section length could be increased. However, a question arises whether such comparison between the clustered-cavity and the conventional scheme is valid. As mentioned, one resonator of the conventional tube was replaced by a couple or triplet in the clustered-cavity device. This means that the total number of cavities in the clustered-cavity GKL was larger than that in the conventional GKL of comparison and, therefore, the comparative analysis was not quite balanced. The present section is aimed at a "one-to-one" comparison of the conventional and clustered-cavity GKLs, in which the total number of cavities is the same for both schemes. The author considers two schemes of four-cavity GKLs: conventional scheme, in which all cavities are separated, and the clustered-cavity scheme shown in Fig. 2.2.

2.3.1: Point-gap model for the three-stage clustered-cavity gyroklystron

In this subsection the author will show the most important steps in the derivations for the clustered-cavity GKL under analysis. The derivations are based on the formalism described in the previous section.

The following representation for the field in the cluster can be used [35]:

$$F_{cc} = |F_{2,1}| \exp(i\psi_{2,1}) + |F_{2,2}| \exp(i\psi_{2,2}),$$ (2.18)

where $|F_{2,1}| \exp(i\psi_{2,1})$ and $|F_{2,2}| \exp(i\psi_{2,2})$ are the complex fields in the first and second cavities of the cluster, respectively. The susceptibility of the beam with respect to the field in the first cavity of the cluster can be given as

$$\chi_{2,1} = -i - \frac{2i}{|F_{2,1}|} \left\langle \exp(-i\theta_{dr,1}) \right\rangle \exp(-i\psi_{2,1}),$$ (2.19)

which allows one to determine the complex field in the first cavity of the cluster from the balance equation (2.6):

$$|F_{2,1}| \exp(i\psi_{2,1} - i\phi_2) = -2 \frac{J_1(q_1) I_{0(2,1)}}{(I_{0(2,1)} + 1) + i\delta_{2,1}}.$$ (2.20)

Here $q_1 = 2|F_1| \mu_{1,dr}$ is the so-called bunching parameter of the input cavity where $\mu_{1,dr}$ is the normalized length of the first drift-section. In the same manner, the beam susceptibility with respect to the field in the second cavity of the cluster is

$$\chi_{2,2} = -i - 2i \frac{|F_{2,1}|}{|F_{2,2}|} \exp(i\psi_{2,1} - i\psi_{2,2}) - 2i \frac{J_1(q_1)}{|F_{2,2}|} \exp(i\phi_2 - i\psi_{2,2}),$$ (2.21)

which gives

$$| F_{2,2} | \exp(i\psi_{2,2} - i\phi_2) = -2J_1(q_1)\frac{I_{0(2,2)}(1 - I_{0(2,1)} + i\delta_{2,1})}{(1 + I_{0(2,1)} + i\delta_{2,1})(1 + I_{0(2,2)} + i\delta_{2,2})}. \qquad (2.22)$$

So, the expression for the complex field in the cluster can be given as:

$$F_{cc} = -2J_1(q_1)\exp(i\phi_2)\left(\frac{I_{0(2,1)}}{1 + I_{0(2,1)} + i\delta_{2,1}} + \frac{I_{0(2,2)}}{1 + I_{0(2,2)} + i\delta_{2,2}} - \right.$$
$$\left. -\frac{2I_{0(2,1)}I_{0(2,2)}}{(1 + I_{0(2,1)} + i\delta_{2,1})(1 + I_{0(2,2)} + i\delta_{2,2})} \right) \qquad (2.23)$$

For the case of small beam loading, small input cavity prebunching and with the assumption $I_{0(2,1)} \simeq I_{0(2,2)} = I_{02}$ the expression for the field intensity in the cluster takes the following form

$$| F_{cc} |^2 = (2q_1 I_{02})^2 \frac{1 + [(\delta_{2,1} + \delta_{2,2})/2]^2}{(1 + \delta_{2,1}^2)(1 + \delta_{2,2}^2)}. \qquad (2.24)$$

The field intensity in the output cavity is given as

$$| F_3 |^2 = \frac{4I_{03}^2 | \mathcal{F}_3 |^2}{(1 + I_{03})^2 + \delta_3^2}, \qquad (2.25)$$

where $\mathcal{F}_3 = \exp(-i\phi_3)(q_1 - iq_2\exp(i\phi_2))/2$. Assuming $q_2 \gg q_1$ (small signal case), one may easily get $| \mathcal{F}_3 |^2 = q_2^2/4 = | F_{cc} |^2 \mu_{2,dr}^2$, where $\mu_{2,dr}$ is the normalized length of the second drift-section. From the expressions just obtained and the expression for the field intensity in the input cavity, A_s, the following expression for the gain of the three-stage clustered-cavity GKL can be obtained:

$$G_{SS,clust} = 20\log(8I_{03}I_{02}\mu_{1,dr}\mu_{2,dr}) -$$
$$-10\log\left\{ \frac{(1 + \delta_1^2)(1 + \delta_{2,1}^2)(1 + \delta_{2,2}^2)(1 + \delta_3^2)}{1 + [(\delta_{2,1} + \delta_{2,2})/2]^2} \right\}. \qquad (2.26)$$

2.3.2: Efficiency studies

We start our comparative analysis with the efficiency studies of both schemes. First, we will consider the conventional four-cavity GKL. The bunching efficiency of the device can be given by

$$\eta_b = \left| \frac{1}{2\pi} \int_0^{2\pi} \exp(i\vartheta_{entr}) d\vartheta_0 \right|^2, \tag{2.27}$$

where ϑ_{entr} is the slowly variable gyrophase at the entrance to the output cavity. The bunching efficiency is equal to the orbital efficiency of interaction at the first harmonic within the point-gap model. The slowly variable gyrophase ϑ_{entr} has the following form (see Eq. (2.9)):

$$\begin{aligned}
\vartheta_{entr} &= \vartheta_0 + \Delta\mu_\Sigma - q_1 \sin\vartheta_0 - q_2 \sin(\Delta\psi_1 + \vartheta_0 + \\
&+ \Delta r_1\mu_\Sigma - q_1 r_1 \sin\vartheta_0) - q_3 \sin(\Delta\psi_2 + \vartheta_0 + \Delta r_2\mu_\Sigma - \\
&- q_1 r_2 \sin\vartheta_0 - q_2 r \sin[\Delta\psi_1 + \vartheta_0 + \Delta r_1\mu_\Sigma - q_1 r_1 \sin\vartheta_0]).
\end{aligned} \tag{2.28}$$

Here μ_Σ is the normalized length of the circuit preceding the output cavity, q_1, q_2 and q_3 are the bunching parameters describing the ballistic bunching due to the first, second and third cavity field, respectively. The parameter $r_1 = L_{1,dr} / L_\Sigma$ characterizes the location of the second cavity, $r_2 = L_{2,dr} / L_\Sigma$ characterizes the location of the third cavity and $r = (L_{2,dr} - L_{1,dr})/(L_\Sigma - L_{1,dr})$. Also, in Eq. (2.28), $\Delta\psi_1$ and $\Delta\psi_2$ are the phase differences between the complex fields in the first and second and the first and third resonators, respectively. For simplicity, we fixed in our consideration the bunching parameter of the first cavity, q_1=1.84, which corresponds to the maximum of the first harmonic in electron current density in the case of one-cavity prebunching.

Also, for the sake of simplicity, the case of exact cyclotron resonance was considered. Efficiency has been calculated as the function of the second (q_2) and third (q_3) bunching parameters for various locations of the second and third resonators and different values of the phase differences $\Delta\psi_1$ and $\Delta\psi_2$. Some results of these calculations are shown in Fig. 2.3. In this figure, cases (a) and (b) correspond to the relative location of the second cavity $r_1 = 0.1$ and positions of the third cavity $r_2 = 0.15$ and $r_2 = 0.95$, respectively. In other words, the third cavity is, first, close to the second one and both are close to the input cavity (a), and then the third cavity is shifted to the output one (b). As one can see, such shift allowed for increasing the maximum orbital efficiency from about 42% to almost 75%. Figures (c) and (d) correspond to the relative locations $r_1 = 0.3, r_2 = 0.35$ and $r_1 = 0.3, r_2 = 0.95$, respectively. The efficiency values in case (c) are higher than in case (a) and again, by moving the third cavity to the output one, the maximum efficiency for this cavity arrangement is achieved. Results for relative locations $r_1 = 0.6, r_2 = 0.65$ and $r_1 = 0.8, r_2 = 0.95$ are shown in figures (e) and (f). The maximum efficiency corresponds to the case (f) and is about 80%. The phase shifts are $\Delta\psi_1 = \pi/2$ and $\Delta\psi_2 = \pi$ in all the cases. Notice that the location of the maximum efficiency point on the $q_2 q_3$-plane, which corresponds to the negative values of q_3, in cases (b), (d) and (f) is actually the result of a shift of the parameter $\Delta\psi_2$ by π. In other words, by adding $\pm\pi$ to $\Delta\psi_2$, one may keep the values of q_2 and q_3 always positive, which has more sense since the bunching parameter is positive by definition. However, for

70
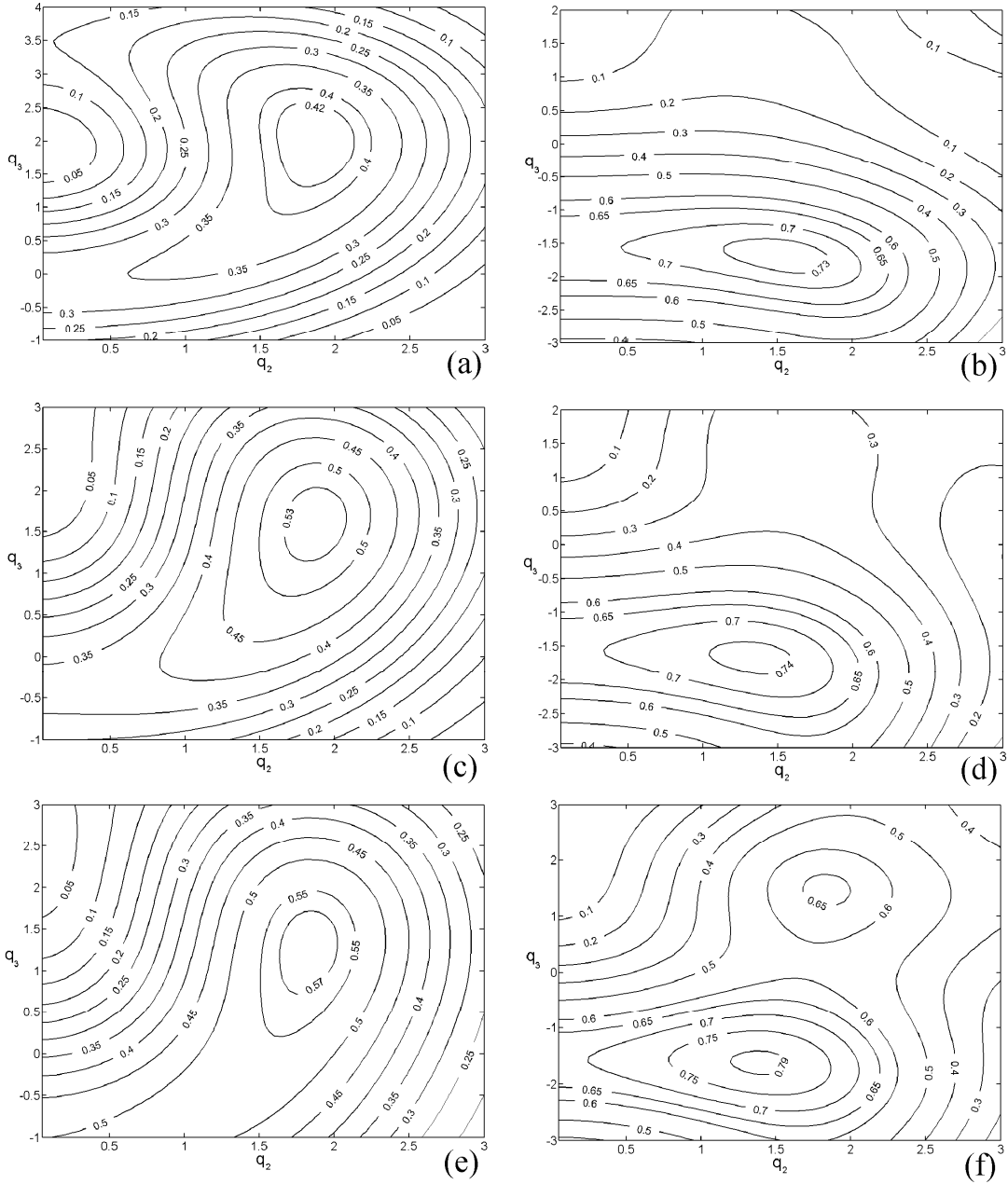
Fig. 2.3. Contour plots of bunching efficiency describing the effect of prebunching in a four-cavity gyroklystron on the plane of bunching parameters: (a) the second and third cavities are located near the input one: $r_1 = 0.1$ and $r_2 = 0.15$; (b) the third cavity is shifted to the output resonator, $r_1 = 0.1$ and $r_2 = 0.95$; (c) the resonator locations are $r_1 = 0.3$ and $r_2 = 0.35$; (d) $r_1 = 0.3$, $r_2 = 0.95$; (e) $r_1 = 0.6$, $r_2 = 0.65$; (f) both intermediate cavities are located close to the output one: $r_1 = 0.8$ and $r_2 = 0.95$.

simplicity of calculations and similarity of the plots, values of $\Delta\psi_2$ were kept unchanged. The results summarizing the ones shown in Fig. 2.3 are demonstrated in Fig. 2.4. In this figure, the dependences of the maximum efficiency values upon the relative location of the third resonator are shown for several locations of the second
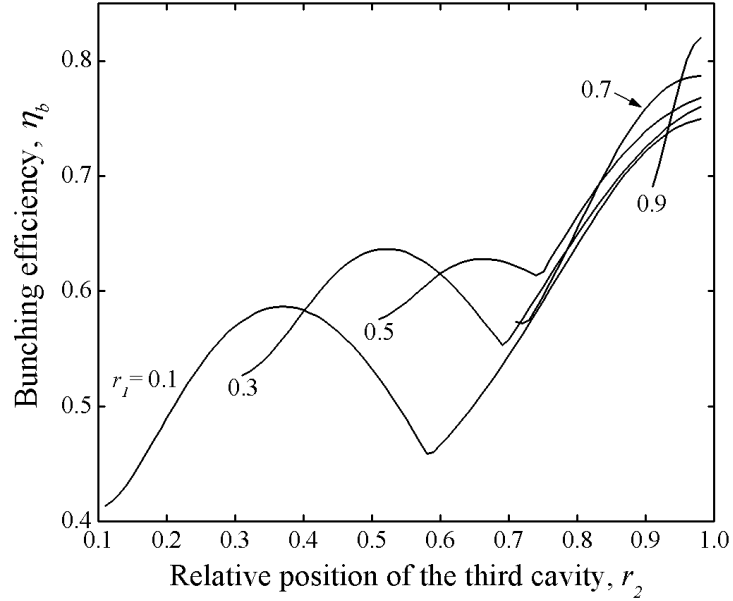
Fig. 2.4. Maximum values of bunching efficiency of a four-cavity gyroklystron. These are shown as functions of the relative position of the third cavity for several locations of the second one.

cavity. One may notice the initial maximum on the curves, which corresponds to positive values of the parameter q_3. The sharp bends on the curves are related to the shift of the parameter $\Delta\psi_2$ just discussed. Notice, that when the relative position of the second cavity reaches the values about *0.6*, the first maximum on the curves disappears, which means that the maximum efficiency is obtained only for negative values of q_3.

Similar calculations were also done for the clustered-cavity GKL. For the clustered-cavity GKL $L_{2,dr} \to L_{1,dr}$, which gives $r_2 \to r_1$. The expression for the gyrophase at the entrance to the 4-th cavity for the case of exact synchronism now takes the form

$$\theta_{entr} = \theta_0 - q_1 \sin \theta_0 - q_2 \sin(\varDelta\psi_1 + \theta_0 - q_1 r_1 \sin \theta_0) - $$
$$-q_3 \sin(\varDelta\psi_2 + \theta_0 - q_1 r_1 \sin \theta_0) \qquad (2.29)$$

The results of the calculations are shown in Fig. 2.5. Here the figures a), b), c) and d) correspond to the relative position of the cluster $r_1 = 0.1$, 0.3, 0.7 and 0.95, respectively.
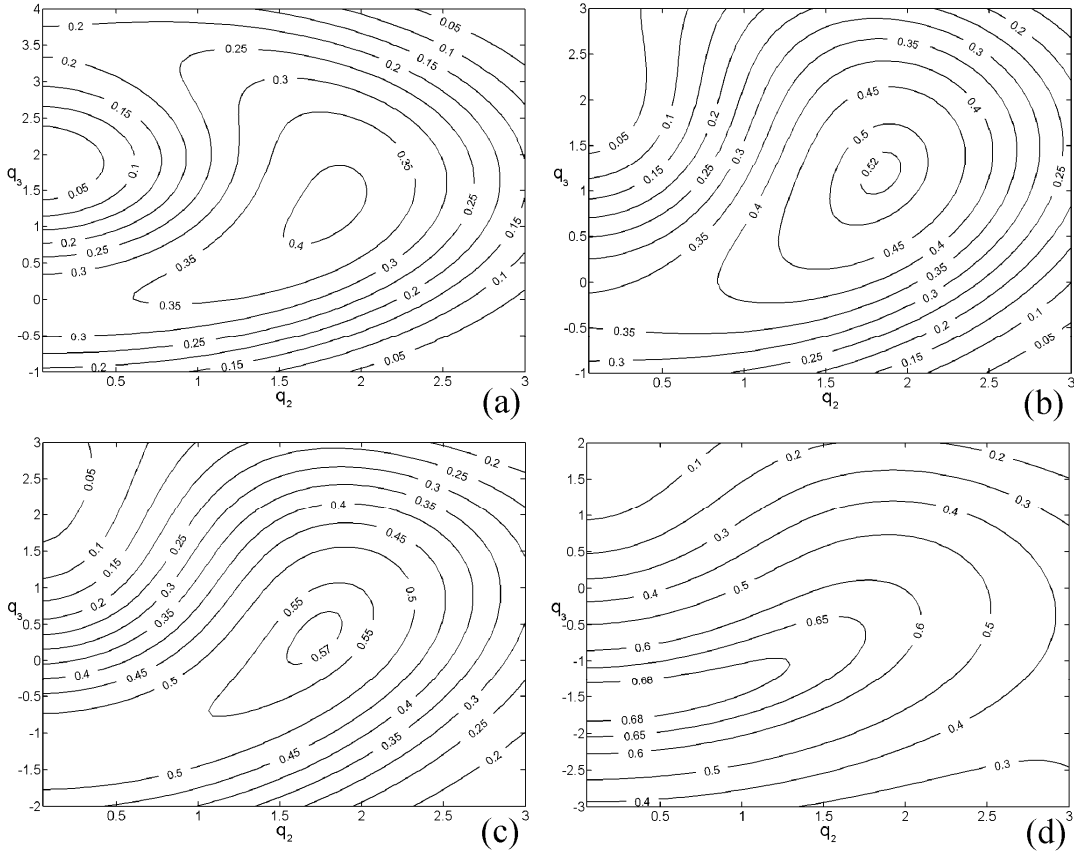
Fig. 2.5. Contour plots of orbital efficiency describing the effect of prebunching in the three-stage clustered-cavity gyroklystron on the plane of bunching parameters. (a) the cluster is close to the input resonator, $r_1 = 0.1$; (b) $r_1 = 0.3$; (c) $r_1 = 0.7$; (d) the cluster is close to the output cavity, $r_1 = 0.95$.

Figure 2.6 demonstrates the results similar to the ones shown in Fig. 2.4. In this figure the dependences of the maximum efficiency versus the relative cluster location are shown. The maximum efficiency is about 70% for $r_1 = 0.95$ that is a little
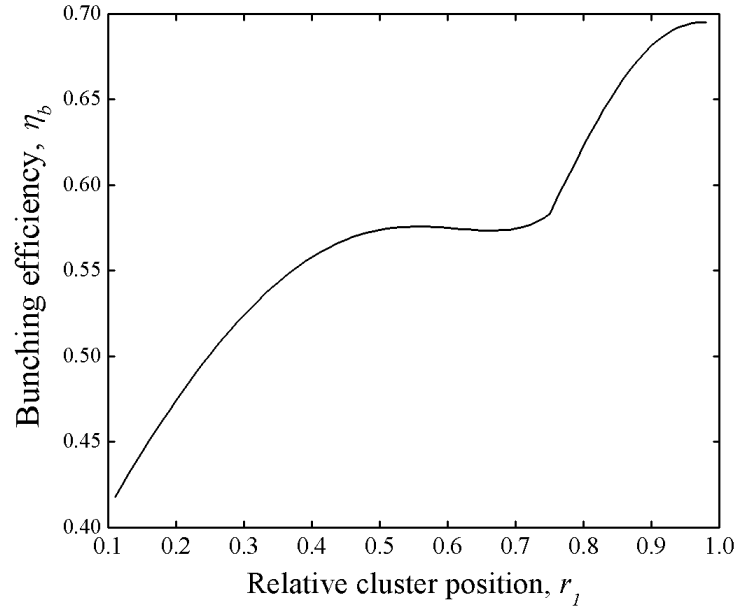
Fig. 2.6. Maximum bunching efficiency values of the clustered-cavity gyroklystron as a function of the relative position of the cluster.

smaller than in the previous case. This result is similar to the one obtained for the conventional GKL where the maximum efficiency is obtained when the second and third cavities are located near the output one. Therefore, a conclusion can be made that both conventional and clustered-cavity GKLs reach the highest efficiency values when their intermediate cavities are located close the output.

2.3.3: Gain studies

In a small-signal regime, the expression for the gain for both the conventional GKL and the clustered-cavity GKL can be represented as a superposition of two terms [34]:

$$G_{SS} = G_{SS}^{const} + G_{SS}^{(var)}(\omega_{sign}).$$

In the case of negligibly small beam loading, corresponding expressions for the clustered-cavity GKL gain can be written as (See Eq. (2.26)):

$$G_{SS,clust}^{(const)} = 20\log\{8I_{02}I_{03}\mu_\Sigma^2 r_1(1-r_1)\} \tag{2.30}$$

$$G_{SS,clust}^{(var)} = -10\log\{(1+\delta_1^2)(1+\delta_{2,1}^2)(1+\delta_{2,2}^2)(1+\delta_3^2)\} +$$
$$+10\log\{1+[(\delta_{2,1}+\delta_{2,2})/2]^2\} \tag{2.31}$$

In these expressions, μ_Σ is the total normalized length of the device. Similar expressions for the conventional GKL can be written as [34]:

$$G_{SS,conv}^{(const)} = 20\log\{8I_{02}I_{03}I_{04}\mu_\Sigma^3 r_1(r_2-r_1)(1-r_2)\} \tag{2.32}$$

$$G_{SS,conv}^{(var)} = -10\log\{(1+\delta_1^2)(1+\delta_2^2)(1+\delta_3^2)(1+\delta_4^2)\} \tag{2.33}$$

One may notice that when the cavities in the cluster are symmetrically detuned, i.e. when in Eq. (2) $\delta_{2,1} = -\delta_{2,2}$, the variable parts of the gains are the same for both schemes.

It can easily be shown that the constant parts of the gain, which depend upon the location of the cavities, reach their maximum values when $r_1 = 1/3$ and $r_2 = 2/3$ for the conventional GKL and when $r_1 = 1/2$ for the clustered-cavity GKL. This means that the cavities must be equally spaced in the conventional device and the cluster

must be in the middle of the device in the clustered-cavity GKL. Obviously, these results are not consistent with the ones obtained in the efficiency analysis, where the maximum efficiency is achieved when the intermediate cavities are close to the output in both schemes. Therefore, the choice of resonator location should be determined as a result of a trade-off between the gain and efficiency.

Now, let us compare the constant parts of the gains for both schemes with the assumption that the lengths of the devices are equal, the resonators are located to yield the maximum gain and $I_{0i} = I_0$. Then, for the conventional GKL one may get:

$G_{SS,conv}^{(const)} = 60 \log(2 I_0 \mu_\Sigma / 3)$, and for the clustered-cavity GKL:

$G_{SS,clust}^{(const)} = 20 \log 2 + 40 \log I_0 \mu_\Sigma$. Figure 2.7 demonstrates both gains plotted as functions of $I_0 \mu_\Sigma$. One may conclude from this figure that the clustered-cavity scheme is preferable when there are limitations on the length of the device and/or the beam current.
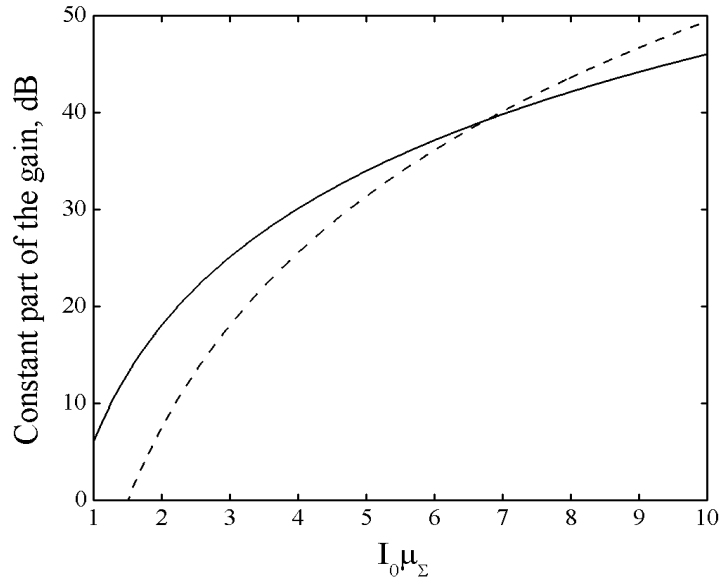
Fig. 2.7. Constant parts of the gains for the conventional four-cavity GKL (dashed) and the three-stage clustered-cavity GKL (solid) as functions of the normalized current - device length product.

76

2.3.4: Bandwidth studies

For the sake of simplicity, let us consider the case when eigenfrequencies of the cavities' modes form an equidistant spectrum, i.e.

$$\omega_{n+1} - \omega_n = \Delta\omega = const \ \ (n = 1, 2, 3).$$

The dependences of $G_{SS,conv}^{(var)}$ and $G_{SS,clust}^{(var)}$ upon frequency detuning given by (2.31) and (2.33) for several values of the stagger-tuning parameter, ξ ($\xi \sim \Delta\omega$), are shown in Fig. 2.8. It can be seen that the use of clustered cavities allows one to achieve much
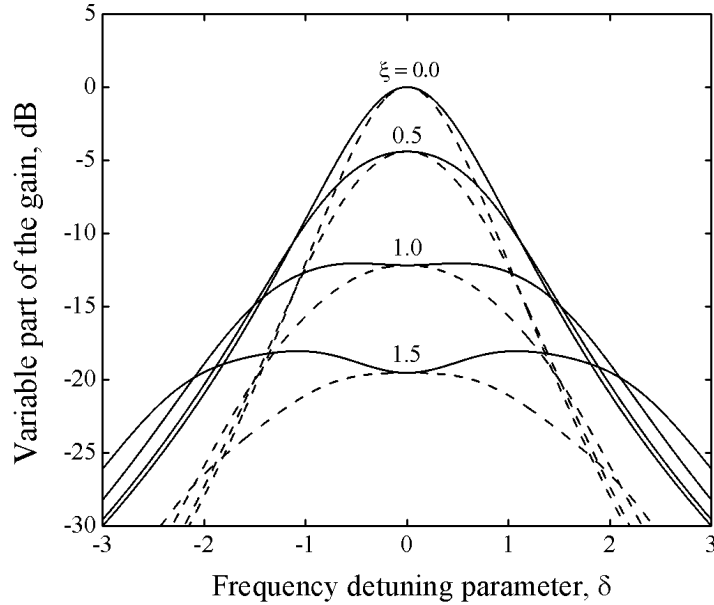
Fig. 2.8. Variable parts of the small-signal gains for the four-cavity conventional GKL (dashed) and the three-stage clustered-cavity GKL (solid) as functions of frequency detuning for several values of the stagger-tuning parameter.

larger bandwidths in comparison with the conventional scheme. Bandwidths in terms of δ as functions of the stagger-tuning parameter are shown in Fig. 2.9. One may see that the bandwidth of the clustered-cavity GKL is almost twice larger than that for the
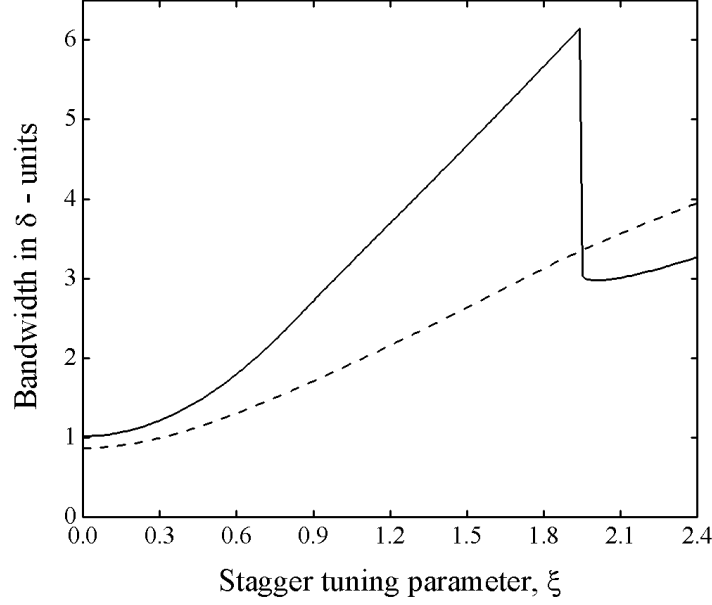
Fig. 2.9. Bandwidths in terms of δ as functions of the stagger-tuning parameter for the four-cavity conventional GKL (dashed) and the three-stage clustered-cavity GKL (solid).

conventional device when ξ is about 1.8. The sharp drop on the curve for the clustered-cavity GKL is due to the fact that the valley at the center of its bandwidth characteristic (see Fig. 2.8) becomes deeper than 3dB and the bandwidth collapses. However, such bandwidth degradation must not be a problem since it occurs at large values of ξ where device operation is not practical because of substantial gain loss caused by stagger tuning.

The plots of gain-bandwidth products and gain degradation as functions of stagger-tuning parameter are shown in Fig. 2.10. Case (a) corresponds to the constant part of the gain $G_{SS}^{(const)} = 35$ dB and case (b) corresponds to $G_{SS}^{(const)} = 45$ dB for both schemes. Such choice of $G_{(SS)}^{(const)}$ corresponds to $I_0 \mu_\Sigma \simeq 5.2$ and $I_0 \mu_\Sigma \simeq 8.5$, respectively (see Fig. 2.7). This, for example, may stand for shorter and longer tubes to be analyzed keeping I_0 fixed. Again, it can be seen that the clustered-cavity GKL

78

possesses an advantage over the conventional GKL in both cases (even in the absence of stagger tuning).
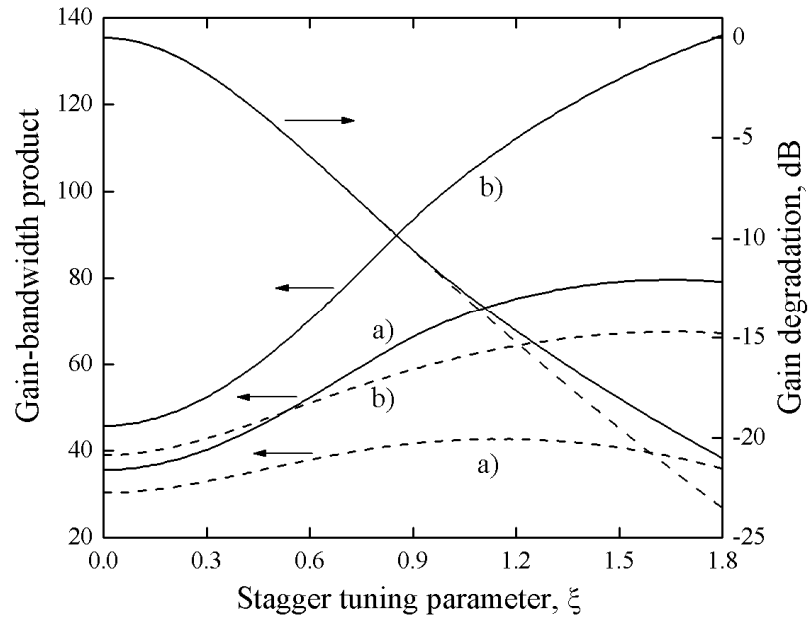
Fig. 2.10. Normalized gain-bandwidth product and gain degradation for the four-cavity conventional GKL (dashed) and the three-stage clustered-cavity GKL (solid) as functions of the stagger-tuning parameter. The constant parts of the gain are (a) 35 dB and (b) 45 dB for both schemes.

Chapter 3: Startup Scenarios in High-Power Gyrotrons

3.1: Preliminary remarks

As a rule, any microwave oscillator passes through a time-dependent variation of operating conditions before it reaches its steady-state operating point. This startup scenario should first fulfill the conditions for self-excitation, and then move to the stable operating point in a way that ensures that the desired mode is excited with maximum efficiency at the desired power level, while the neighboring modes are suppressed.

For microwave sources driven by electron beams, the self-excitation conditions are usually characterized by the starting current I_{st}, which is a function of various operating parameters (such as the beam voltage, beam position, etc.) So, when beam current I_b exceeds I_{st} the self-excitation conditions are fulfilled, and this gives rise to oscillations. If the operating parameters are reasonably chosen, the oscillations reach the steady-state regime in a certain transit time. The parameter region, where $I_b \geq I_{st}$, is known as the region of soft self-excitation. The oscillations in this region can start growing from the noise level, which is usually determined by the presence of the beam. In addition to the region of soft self-excitation, there is also a region of hard self-excitation, which exists in many oscillators. The self-excitation conditions starting from low noise level are not fulfilled in this region (i.e. $I_b < I_{st}$), however the oscillations can be sustained, once their initial amplitude exceeds a certain threshold level. This classification was first introduced by Appleton and van

der Pol for radio oscillators [58] and then used in consideration of various sources of coherent electromagnetic radiation. In the region of hard self-excitation, devices exhibit hysteresis. That is, depending on the history of parameter variation, one can observe for a given final set of parameters either the presence or the absence of oscillations. Very often, the maximum efficiency can be obtained only in the region of hard self-excitation. In such cases, the device parameters should, first, pass through the region of soft self-excitation before reaching the point of the most efficient operation in the hard self-excitation region. Of course, the oscillations should remain stable in the process of this transition.

If a device is designed to operate at a high-order mode, the startup problem becomes even more complicated, because the mode spectrum is very dense and, therefore, the self-excitation conditions can simultaneously be fulfilled for several modes. It is desirable to excite the operating mode prior to the others in this case and then maintain the conditions under which this mode will suppress all competitors. Suppression occurs due to nonlinear competition between the modes [59]. The mode competition results in the fact that effectively the starting current of a parasitic mode is increased by the presence of the desired operating mode. Therefore, relying upon the effect of mode competition, it becomes possible to drive the desired mode to the point of the most efficient operation even in the presence of many competing modes [60]. It is necessary to emphasize that such a scenario should be realized on a timescale that greatly exceeds the cavity fill time, Q/ω, since all changes made on a shorter timescale can be considered as an instant turn-on. For typical frequencies in the range of 100 GHz and Q-factors of the order of 10^3, this means the variation of

parameters with the timescale exceeding 10 ns. (In reality, the beam voltage and current rise times are usually much longer than microseconds in devices designed for a long-pulse operation).

Now, the question arises "Which parameters in the scenario should be varied to fulfill all the conditions described?" It is known that the minimum start current in gyrotrons corresponds to smaller mismatches of the resonance than the high-efficiency regime, because the EM-field of large amplitude can trap electrons even in the case of large initial mismatches [61], [62]. Since the cyclotron resonance mismatch in gyrotrons is proportional to $\omega - s\Omega_0$, it can be concluded that the relativistic cyclotron frequency in the initial excitation phase should be larger than in the final one of the efficient operation. So, the startup scenario should imply either the decrease of the external magnetic field or the increase of the beam voltage. In the case of continuous wave operation, both of them can be varied. However, the possibilities of varying the magnetic field are severely limited in the case of pulsed operation, especially when the superconducting solenoids are used. Therefore, the studies of start-up scenarios are usually focused on the voltage variation [63], [64]. It should be emphasized that the beam voltage rise alone, which is typically slow enough, automatically changes the cyclotron resonance mismatch in the desired way.

Now, let us briefly discuss different types of mode interaction in gyrotrons. The simplest case of interaction is the one between two modes only. When their frequencies are well separated, $|\omega_2 - \omega_1| \gg \omega/Q$, or the modes are azimuthally orthogonal, $m_2 \neq m_1$, the phase relations can be eliminated from the equations for mode intensities, i.e. the changes in mode amplitudes become independent of their

phases. This is the same situation that occurs in radio oscillators with two degrees of freedom [59], as well as in other microwave oscillators [65], where the mode frequency separation is much larger than the mode resonance width. This kind of interaction is often called the nonsynchronous one [60]. Two kinds of coupling between modes in this case, "strong" and "weak", were analyzed by Lamb for lasers [66]. In the first case, both modes interact with the same electrons, and hence strongly compete. In the second case, the modes predominantly interact with different electrons and, therefore, are weakly coupled.

The case when the evolution of mode amplitudes depends on the phase relations is known as the synchronous or parametric interaction. When all modes are in resonance with electrons at the same cyclotron harmonic, the synchronous or parametric interaction may occur between three modes, whose frequencies and azimuthal indices obey the following conditions [60]:

$$\omega_1 + \omega_3 \approx 2\omega_2, \quad m_1 + m_3 = 2m_2 . \tag{3.1}$$

Here index "2" designates the central mode, while indices "1" and "3" designate the low-frequency and high-frequency satellites, respectively. The first condition in (3.1) is an approximate one because the modes have a finite width of resonance curves. So, it is possible to have the mode frequencies slightly detuned from an exactly equidistant spectrum. The corresponding condition can be written more precisely as

$$|2\omega_2 - \omega_1 - \omega_3| \leq \frac{\omega}{Q} . \tag{3.2}$$

Neighboring whispering gallery modes ($m \gg p$) with the same radial index generally satisfy the conditions given by (3.1) and (3.2). So, the parametric interaction between such modes can take place. Obviously, this interaction becomes significant only when

the mode frequency separation is smaller than the cyclotron resonance band, i.e., when each of the modes can interact with electrons resonantly.

Instability of the central mode with respect to such symmetric satellites is often called the automodulation or sideband instability. The first study of this instability was carried out by Zapevalov and Nusinovich in 1985 [67]. In this work, the authors showed that the regime with maximum efficiency can be stable with respect to the satellites when the resonator length is reasonably short. It was also found that the most dangerous satellites are not the modes located very close to the operating one, but those that have a certain frequency separation. This conclusion was later confirmed by other authors [68], [69]. There are two conditions of the stability of the central mode oscillations. The authors in Refs. [68] and [69] characterized corresponding instabilities as the phase instability and the overbunch instability. The result of the phase instability is the jumping from one mode to another, while the result of overbunch instability can be a multimode equilibrium.

3.2: Excitation of the gyromonotron

In this section, the formalism describing the excitation of resonators at one mode is described briefly. Obviously, it cannot give the idea of mode excitation in the presence of other modes, however it can be used for some simple estimates that will be shown below.

The non-stationary interaction process in the gyrotron cavity can be described by the gyro-averaged equations of electron motion and the equation, which describes the excitation of the resonator field by an electron beam. The equations of electron motion can be given as

$$\frac{dw}{d\zeta} = 2\,\mathrm{Im}\left\{ Ff(\zeta) w^{s/2} \exp(-i\vartheta) \right\} \tag{3.3}$$

$$\frac{d\vartheta}{d\zeta} + \Delta + w - 1 = -s\,\mathrm{Re}\left\{ Ff(\zeta) w^{(s/2)-1} \exp(-i\vartheta) \right\}. \tag{3.4}$$

These are essentially equations (2.1) and (2.2) rewritten in new variables, viz.

$$w = p'^2 = p_\perp^2 / p_{\perp 0}^2 = 1 - 2(\mathcal{E}_0 - \mathcal{E})/\beta_{\perp 0}^2 \mathcal{E}_0, \quad \zeta = s\zeta', \quad F = F'/s \quad \text{and} \quad \vartheta = -(s\vartheta' + \pi/2)$$

(here primes denote the "old" variables used in Chapter 2). The excitation equation has the following general form [70]:

$$\frac{dB}{dt} + i(\omega - \omega_s)B = -\frac{1}{2N_s} \int_V \vec{j}_\omega \cdot \vec{E}_s^* dv, \tag{3.5}$$

where the integration in the RHS is performed over the resonator volume V. In this equation, B is the complex amplitude of the magnetic field represented as $\vec{H} = \mathrm{Re}\left\{ B\vec{H}_s(\vec{r}) \exp(i\omega t) \right\}$, where the function $\vec{H}_s(\vec{r})$ describes the spatial

structure of this field (correspondingly, $\vec{E}_s(\vec{r})$ describes the spatial structure of the electric field), $\omega_s = \omega_s'(1 + i/2Q_s)$ is the cold-cavity frequency, $\vec{j}_\omega$ is related to the electron current density $\vec{j}$ as $\vec{j} = \mathrm{Re}\{\vec{j}_\omega \exp(i\omega t)\}$ and N_s is the norm of the operating mode given by

$$N_s = \frac{1}{4\pi} \int_V |\vec{E}_s|^2 \, dv = \frac{1}{4\pi} \int_V |\vec{H}_s|^2 \, dv. \tag{3.6}$$

The real part of the cold-cavity frequency, ω_s, determines the mode eigenfrequency, whereas its imaginary part describes some losses. Typically, two sorts of losses – ohmic and diffraction – can be important when gyrotron open resonators are considered. Thus, Q_s can be determined as

$$\frac{1}{Q_s} = \frac{1}{Q_{dif}} + \frac{1}{Q_{ohm}}. \tag{3.7}$$

The excitation equation (3.5) can be rewritten in the gyrotron form for the normalized amplitude F:

$$\frac{dF}{d\tau} = F \left\{ I_s \Phi - \frac{1}{2Q} - i \frac{\omega - \omega_s'}{\omega} \right\}, \tag{3.8}$$

where $\tau = \omega t$ is the normalized time, I_s is the normalized current parameter and Φ is the complex gain function

$$\Phi = \Phi' + i\Phi'' = -\frac{i}{F} \frac{1}{2\pi} \int_0^{2\pi} \left\{ \int_{\zeta_{in}}^{\zeta_{out}} f^*(\zeta) w^{s/2} \exp(i\vartheta) \, d\zeta \right\} d\vartheta_0. \tag{3.9}$$

This function can be expressed via the susceptibility of an electron beam with respect to the resonator field, $\hat{\chi}$ [71]:

$$\Phi = -i \frac{\hat{\chi}}{2}. \tag{3.10}$$

In the regime of stationary oscillations at frequency ω the real part of Eq. (3.8) represents the balance of active powers

$$2I_s Q\Phi' = 1.$$

(3.11)

This is essentially the balance equation (I.22) given in the Introduction. The imaginary part of Eq. (3.8) in the same regime demonstrates the so-called frequency pulling effect, i.e. the shift of the oscillation frequency ω with respect to the oscillation frequency:

$$I_s\Phi'' = \frac{\omega - \omega_s'}{\omega}.$$

(3.12)

By integrating Eq. (3.3) and averaging it over the initial phases, one may represent the real part of the gain function as $\Phi' = \eta_\perp / 2 |F|^2$, where $\eta_\perp = \langle 1 - w(\zeta_{out}) \rangle_{\vartheta_0}$ is the orbital efficiency of interaction introduced before. Correspondingly, the balance equation (3.11) can be rewritten as

$$|F|^2 = I_0 \eta_\perp,$$

(3.13)

where a new normalized current parameter, $I_0 = I_s Q$, has been introduced. It can be noticed that this equation is similar to the energy conservation law for the gyro-TWT given by Eq. (1.9) of Chapter 1.

Equation (3.11) defines the starting value of the normalized beam current through the corresponding value of the real part of the gain function. It is possible to calculate Φ in the framework of the small-signal theory in the following way. Assuming that the normalized amplitude F is small, one may find the zero-order solutions for w and ϑ:

$$w_{(0)} = 1, \quad \vartheta_{(0)} = \vartheta_0 - \Delta\zeta.$$

(3.14)

The first-order approach results in

$$w_{(1)} = 2\,\mathrm{Im}\left\{F\int_0^\zeta f(\zeta')\exp(-i\vartheta_{(0)})d\zeta'\right\} \qquad (3.15)$$

$$\vartheta_{(1)} = -\int_0^\zeta w_{(1)}(\zeta')d\zeta' - s\,\mathrm{Re}\left\{F\int_0^\zeta f(\zeta')\exp(-i\vartheta_{(0)})d\zeta'\right\}. \qquad (3.16)$$

Substituting these solutions into the expression for the linearized gain-function,

$$\Phi_{lin} = -\frac{i}{F}\frac{1}{2\pi}\int_0^{2\pi}\left\{\int_{\zeta_{in}}^{\zeta_{out}} f^*(\zeta)\left(\frac{s}{2}w_{(1)}+i\vartheta_{(1)}\right)\exp(i\vartheta_{(0)})d\zeta\right\}d\vartheta_0, \qquad (3.17)$$

and introducing $f'(\zeta) = f(\zeta)\exp(i\Delta\zeta)$, one may obtain

$$\Phi_{lin} = \int_{\zeta_{in}}^{\zeta_{out}} f'^*(\zeta)\left\{i\int_0^\zeta d\zeta'\int_0^{\zeta'} f'(\zeta'')d\zeta'' - s\int_0^\zeta f'(\zeta')d\zeta'\right\}d\zeta, \qquad (3.18)$$

which does not contain the normalized amplitude F and depends only on the axial structure of the field and the detuning parameter. This expression can be simplified by the use of the relations

$$\left|\int_{\zeta_{in}}^{\zeta_{out}} f'(\zeta)d\zeta\right|^2 = \int_{\zeta_{in}}^{\zeta_{out}} f'(\zeta)\left\{\int_0^\zeta f'^*(\zeta')d\zeta'\right\}d\zeta + \int_{\zeta_{in}}^{\zeta_{out}} f'^*(\zeta)\left\{\int_0^\zeta f'(\zeta')d\zeta'\right\}d\zeta$$

and $df'/d\Delta = i\zeta f'$. Thus, the imaginary part of the susceptibility $\hat{\chi}$ introduced in Eq. (3.10) can be given as

$$\hat{\chi}'' = 2\Phi' = -\left(s+\frac{d}{d\Delta}\right)\left|\int_{\zeta_{in}}^{\zeta_{out}} f'(\zeta)d\zeta\right|^2. \qquad (3.19)$$

It follows from the Eqs. (3.10)-(3.11) that $\hat{\chi}''$ is related to the starting current I_0 as

$$I_0 = \frac{1}{\hat{\chi}''}, \qquad (3.20)$$

which represents the self-excitation condition for a given mode in gyrotron. Oscillations start to grow in the region where $I_0 > 1/\hat{\chi}''$.

The axial structure of the field in open resonators is often approximated by the Gaussian function $f(\zeta) = \exp\{-(2\zeta/\mu-1)^2\}$, for which [62]

$$\hat{\chi}'' = \frac{\pi}{4}\mu^2\left(\frac{\Delta\mu^2}{4}-s\right)\exp\left\{-\frac{(\Delta\mu)^2}{8}\right\} \qquad (3.21)$$

with μ being the normalized length of the resonator.

3.3: Analysis and simulations

3.3.1: Starting current and the growth rate of oscillations

The beam current and the starting current vary during the voltage rise. The evolution of the beam current and the electron orbital-to-axial velocity ratio with the voltage can be determined with the use of either the adiabatic theory of magnetron-type electron guns [72]-[74], or numerical codes (such as the widely used E-gun code [75]). The starting current determination is somewhat more complicated. As shown in the previous section, it is possible to derive an expression for the starting current in the framework of the small-signal theory. However, these results are valid only in the case of cold-cavity approximation and when there is no interaction between the electrons and the RF field after the resonator output cross section. The cold-cavity approximation works well when the diffractive Q-factor for a resonator of length L, $Q_{dif} \simeq \omega L / v_{gr}$, is much larger than its minimal value, which can be estimated as $Q_{dif,\min} \approx 4\pi (L/\lambda)^2$ [53]. The designs presently used in MW-class CW gyrotrons often have a smooth transition between the cylindrical section, which plays the role of the resonator, and the output uptaper (see Fig. 3.1). The diffractive Q-factor for such resonators is close to its minimum value. Even more important is the fact that the interaction between the electron beam and the outgoing radiation continues in the output uptaper. Indeed, the angle of tapering is rather small (it typically ranges from 2° to 5°), and the external magnetic field remains close to its maximum value even after the cylindrical cavity region. Therefore, the interaction can continue in this uptaper and it is very difficult (if not impossible) to precisely determine the cross

section where this process stops. The analysis in Ref. 76 has shown that, depending on the output cross section, i.e. the axial position at which we assume the interaction stops, the starting current can vary significantly. Moreover, the starting currents of the operating and parasitic modes may vary in such a way that the starting current of the operating mode can be either higher or lower than the one of the parasitic mode depending upon the choice of interaction length. Obviously, the linearized starting current calculations are insufficient for determining which of the two neighboring modes will be excited first during the voltage rise.

The growing rate of oscillations can be estimated from the field excitation equation. Since the initial stage of the oscillation growth is considered, the nonlinear terms in the equation (3.8) can be neglected. Then, it can be found that the field intensity grows in time as

$$\exp(\sigma\tau) = \exp\left\{\frac{\omega}{Q}\left(\frac{I_b}{I_{st}} - 1\right)t\right\}. \tag{3.22}$$

So, in addition to the estimate (Q/ω) one gets a factor that characterizes the excess of the beam current over the starting current. Now, the time necessary for the mode to grow from the noise level to the large-signal level should be estimated. The field amplitude at this level becomes large enough to affect the starting current of the second mode. The noise level is the level of spontaneous radiation providing the white noise. As shown in Ref. 69, the amplitude of this noise is proportional to $N_*^{1/2}$, where N_* is the number of electrons passing the resonator during the cavity decay time. This number can be estimated as

$$N_* = nS_b v_z \frac{Q}{\omega} = \frac{I_b}{e} \frac{Q}{\omega} = \frac{I_b(A)Q \cdot 10^9}{f(GHz)} . \tag{3.23}$$

For typical operating parameters such as $I_b \leq 50$ A, $Q \approx 10^3$, $f \geq 100$ GHz, this number is of the order of 10^{12} and, therefore, the initial noise-level amplitude is of the order of 10^{-6}. At the same time, numerous simulations show that large-signal effects start to occur when the amplitude reaches the level of 0.1-1. Correspondingly, the time necessary to reach saturation can be estimated to be

$$t_{sat} \sim (11.5-14)\frac{Q}{\omega}\frac{I_{st}}{I_b - I_{st}} . \tag{3.24}$$

The cases of the instant turn-on and adiabatically slow voltage rise considered in the Section 3.1 can now be redefined more accurately. Lets us assume that there are two competing modes and that the self-excitation conditions are fulfilled for these modes at the voltages $V_{st}^{(1)}$ and $V_{st}^{(2)}$, respectively. The time interval between these voltages for the case of a linear voltage rise, $V(t) = \xi t$, can be estimated as $(\Delta t)_{1-2} = (V_{st}^{(2)} - V_{st}^{(1)})/\xi$. Correspondingly, the "instant turn-on" will be the case when the intensity of the first mode grows insignificantly during this time interval, i.e.

$$(\Delta t)_{1-2} \ll t_{sat} . \tag{3.25}$$

In this case, the self-excitation conditions for the second mode will not be affected by the first one, which has a small amplitude. In the opposite case

$$(\Delta t)_{1-2} \gg t_{sat} \tag{3.26}$$

the first mode has sufficient time to grow large enough to suppress the excitation of the second mode. The coefficient ξ, which characterizes the voltage rise time, in short pulses can be very different from that in long pulses, depending on the

characteristics of the power supply employed. For example, it takes about 1 μs to reach the nominal voltage of about 80 kV in short-pulse gyrotron experiments at MIT [77], whereas this time is larger than 100 μs in long-pulse tests at CPI.

3.3.2: Simulation results for the 140 GHz, 1 MW CPI gyrotron

First, our simulations were performed for the 140 GHz gyrotron developed at CPI for electron-cyclotron resonance heating and current drive in the German stellarator "Wendelstein 7-X" [78]. The circuit geometry and magnetic field profile
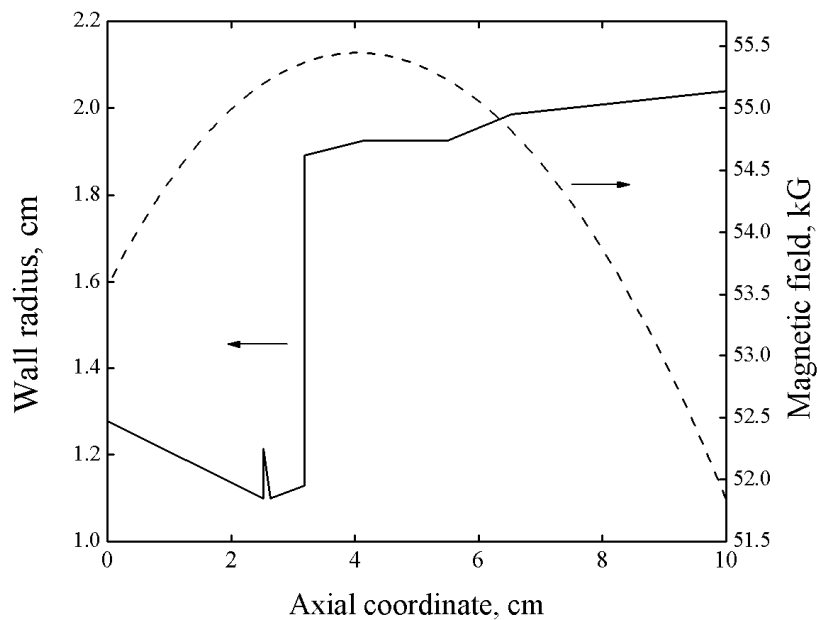
Fig. 3.1. Circuit geometry (solid) and magnetic field profile (dash) for the 140 GHz, 1 MW gyrotron developed at CPI.

for this tube are shown in Fig. 3.1. The operating mode in this tube is $TE_{28,7}$ and the operation is at the fundamental cyclotron resonance. The nominal accelerating

voltage is 80 kV and the corresponding orbital-to-axial velocity ratio is about 1.4. The beam current for this voltage is 40 A.

The preliminary analysis shows that the most important competing modes for a given beam radius are $TE_{27,7}$ and $TE_{29,7}$. The operating mode and these two competitors form a triplet of modes corotating with gyrating electrons, which can interact parametrically. Indeed, the eigenvalues of these modes are the following: $\nu_{27,7} = 55.3046$, $\nu_{28,7} = 56.5182$ and $\nu_{29,7} = 57.7281$ and the corresponding nonequidistance of cutoff frequencies is

$$|2\nu_{28,7} - \nu_{27,7} - \nu_{29,7}|/\nu_{28,7} \approx 6.55 \cdot 10^{-5}.$$

The cold-cavity Q-factor for this gyrotron is about $1.2 \cdot 10^3$, therefore, the conditions (3.1)-(3.2) for synchronous interaction between these modes are fulfilled. However, the frequency separation of these modes is about 2.2%, while the cyclotron resonant band typically does not exceed 1%. Therefore, when one of such modes is excited by the beam, its low- and high-frequency satellites can be present due to the parametric interaction, but the amplitudes of these satellites should be small, because they do not interact resonantly with the beam.

Also important is the triplet of counterrotating modes, having the radial index $p = 8$: $TE_{-24,8}$, $TE_{-25,8}$ and $TE_{-26,8}$. The radial profile of the coupling impedance,

$$G = \frac{J_{m\pm s}^2(\nu_{m,p}R_0/R_w)}{(\nu_{m,p}^2 - m^2)J_m^2(\nu_{m,p})},\tag{3.27}$$

for the six modes under consideration in the vicinity of the beam position is shown in Fig. 3.2. The "minus" and "plus" sign in the expression (3.27) stand for the corotating and counterrotating modes, respectively. In Fig. 3.2, the corotating modes are shown
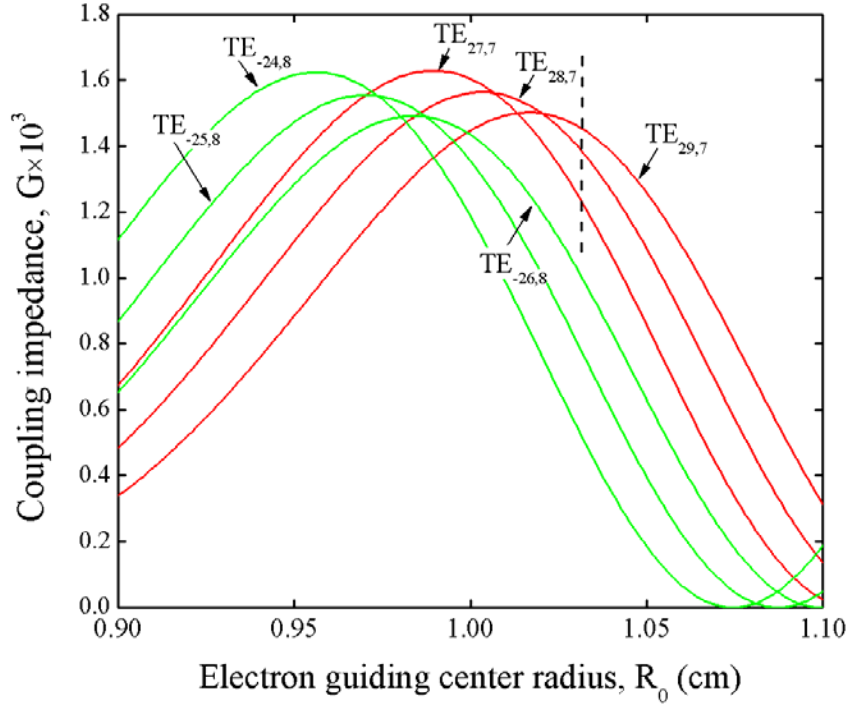
Fig. 3.2. Coupling impedances of the corotating (red) and counterrotating (green) modes in the vicinity of the beam position as functions of the electron guiding center radius. The beam position is indicated by the dashed line.

in red color, while the counterrotating ones are shown in green. The beam position is indicated by the vertical dotted line and it corresponds to the beam radius employed in the gyrotron. The position is intentionally made a little larger than the optimum radius of the operating mode, which strongly reduces the coupling to the counterrotating parasites.

Fig. 3.3 demonstrates the imaginary part of the susceptibility, $\hat{\chi}''$ as a function of the operating frequency and accelerating voltage for the parameters of the device specified. Assuming that the axial field structure in the resonator is close to the Gaussian one, the expression (3.21) was used in these calculations. One may see that the modes with higher frequencies are excited first, whereas the low-frequency modes

are excited at high voltage values at the end of the voltage rise. This is consistent with the changes of the detuning parameter during such rise discussed in Section 3.1. So, a
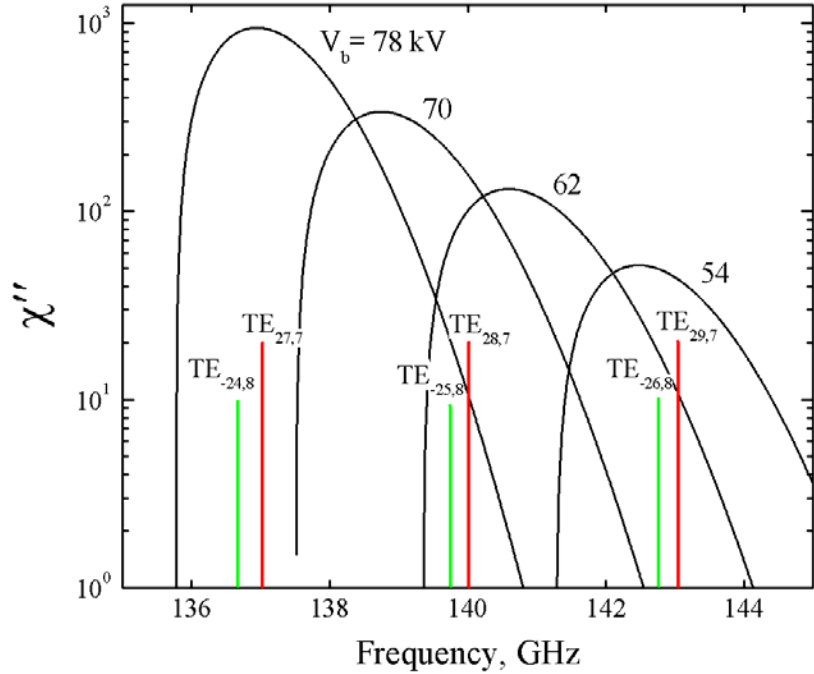
Fig. 3.3. Imaginary part of the beam susceptibility as a function of the operating frequency for several values of the accelerating voltage. The mode cutoff frequencies of the corotating and counterrotating triplets are shown by the red and green vertical lines, respectively.

possible scenario will be the following. The $TE_{29,7}$ and $TE_{-26,8}$ modes are excited first in the regime of soft self-excitation and start growing competing between each other. Then, as the voltage continues to grow, the mode, which wins the competition and suppresses its rival, moves to the region of hard self-excitation, while the modes $TE_{28,7}$ and $TE_{-25,8}$ become excited in the regime of soft self-excitation. At this point a competition may occur between the operating mode and the counterrotating $TE_{-25,8}$. Also, the operating mode may compete with the remaining high-frequency mode.

Eventually, with further voltage increase, the $TE_{29,7}$ or $TE_{-25,8}$ should get outside the resonance band and stop interacting efficiently, while the $TE_{28,7}$ or $TE_{-25,8}$ get into the region of hard self-excitation. The operating mode should stay in this region to achieve the maximum efficiency point. At the end of the voltage rise, the low-frequency modes ($TE_{-24,8}$ and $TE_{27,7}$) may enter the game and bring to a competition, but at that time the operating mode should be strong enough to suppress them.

To verify these simple arguments, simulations were carried out for the six considered modes by the use of the self-consistent, multifrequency code MAGY [26]. Our experience with this code has shown that in order to achieve accurate results, the time step should not exceed 0.1 ns, a small fraction of the cavity fill time ($Q/\omega \approx 8.57$ ns). Thus, the time step chosen in the simulations was 0.05 ns. Then we determined that it takes about 4 h of real-time to simulate 100 ns of mode evolution when six modes are considered. Obviously, it is impossible to simulate the complete 100 μs of the voltage rise in long-pulse gyrotrons. Instead, we had to employ two time-saving techniques. First, we began our simulations at about 50 kV (rather than zero), choosing the initial voltage to be slightly below the voltage at which the modes' growth rates become positive. Second, we divided the voltage rise into 2 kV steps, simulating the mode evolution at each voltage value for 100 ns (a time long enough for these modes to reach steady-state in most cases), and using the final values of the mode amplitudes and phases from the previous run as input data for the subsequent run. This choice of voltage steps and duration of each run corresponds to the voltage rise time coefficient ξ equal to 20 kV/μs. This coefficient is, for comparison, approximately 80- and 0.8 kV/μs for MIT short-pulse experiments and

CPI long-pulse experiments, respectively. Thus, our choice of steps and lengths of runs should be adequate for modeling slower startup scenarios in comparison with the MIT experiments. Although our simulations employ a series of instantaneous voltage steps, such an approach is acceptable if these steps are small enough. The choice of 2 kV step allows accurate description of the mode excitation and competition during the voltage rise; calculations with smaller steps yield the same results.

Results of the simulations are shown in Fig. 3.4. The figure shows the radiated power in all six modes at the output cross section, where the simulations were ended. This cross section is about 3 cm downstream from the end of the straight section forming the resonator ($z = 8.5$ cm, see Fig. 3.1). As expected, the high frequency $TE_{29,7}$ and $TE_{-26,8}$ modes are excited first at low voltages with the counterrotating mode winning their subsequent competition. This mode remains dominant up to voltages of about 64 kV, however its power level is on the order of a few milliwatts only. Then, the central modes of both triplets are excited at 64 kV and the operating mode starts to suppress the counterrotating rival when the voltage reaches 70 kV. However, the oscillations of the low-frequency parasitic $TE_{27,7}$ begin to grow at this voltage level. The three corotating modes coexist at comparable power levels in the range of voltages between 72 and 76 kV. The counterrotating triplet is not completely suppressed here, but the power of its modes is at least two orders of magnitude lower than the power in the corotating triplet. Finally, the desired operating mode starts to suppress all others at about 78 kV reaching the power level of 1 MW at the final voltage. The power of each of the remaining five parasites does not exceed 1 W at this point.
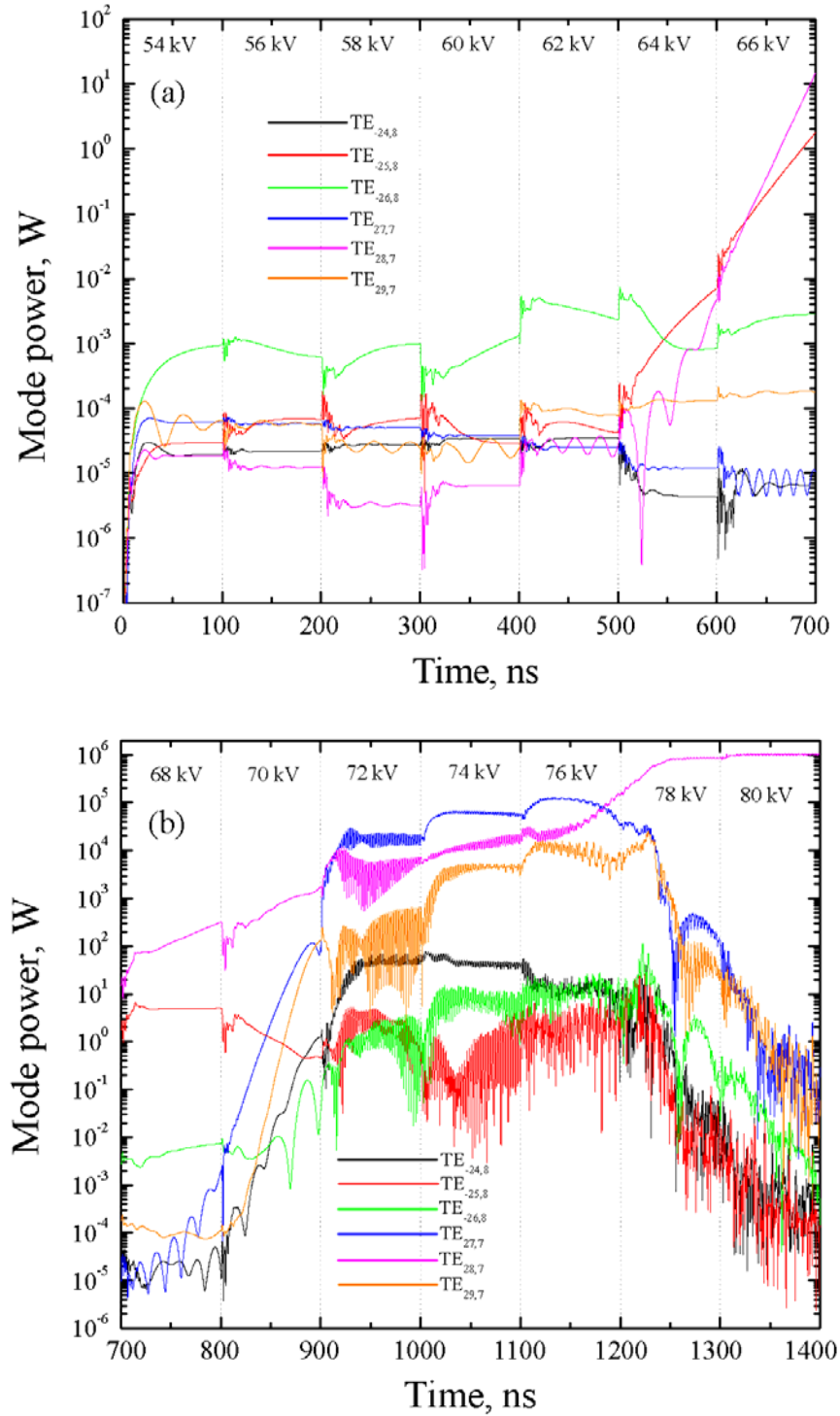
Fig. 3.4. Startup scenario for the 140 GHz, CPI gyrotron. The beam voltage varies in 2 kV steps. For each voltage value, the simulations are conducted for 100 ns time intervals. The voltage values are indicated in the figures.

Although the operation of the desired mode at the final operating parameters has been predicted, it should be noticed that the mode amplitudes did not reach the steady state before the subsequent step at some voltage values. In addition, since some steps demonstrate oscillations in multiple modes, there is a concern that these simulations might indicate that the gyrotron will not reach the desirable steady state if operated at lower voltages. Therefore, we checked some stages of our simulation using longer computational runs. First, we checked the results for 60 kV, where the steady state was not reached in 100 ns. The dominant $TE_{-26,8}$ mode (as well as other modes) reached the steady-state during the run of 400 ns instead of 100 ns. Then we conducted a longer simulation at 64 kV, where the 100-ns interval was clearly not long enough for reaching the steady state. Results of a 700 ns run for this voltage are shown in Fig. 3.5 (a). Its is interesting to notice that during the first 300 ns of this run, when the power of two competing modes ($TE_{28,7}$ and $TE_{-25,8}$) increases, other modes exhibit steady-state operation at lower power levels. However, when the operating mode starts to suppress its rival, the damping of the parasitic $TE_{-25,8}$ mode brings to the appearance of automodulation oscillations in all modes, including the operating one. A further voltage increase causes only the growth of the operating mode power up to 1 MW level, a shown in Fig. 3.5 (b), while the power of all parasites does not exceed 1 mW. It should be noted that the highest power of the most dangerous parasitic $TE_{-25,8}$-mode did not exceed 1 W in the long runs, while some parasitic modes reached the 100 kW level in the short ones (see Fig. 3.4 (b)). These effects demonstrate that the predicted behavior is quite sensitive to the details of the startup scenario if the voltage changes fast relative to the rise times of the modes considered.
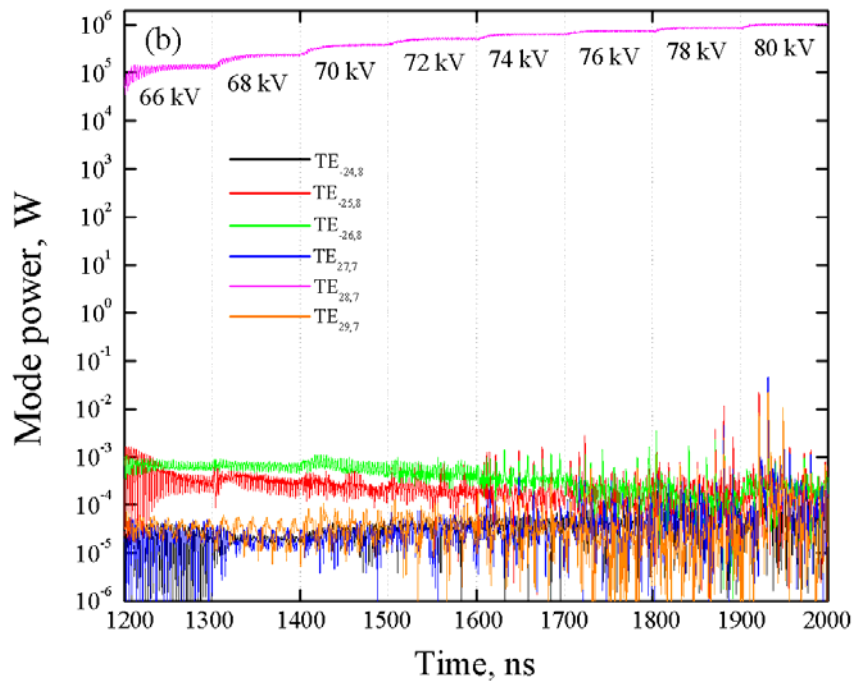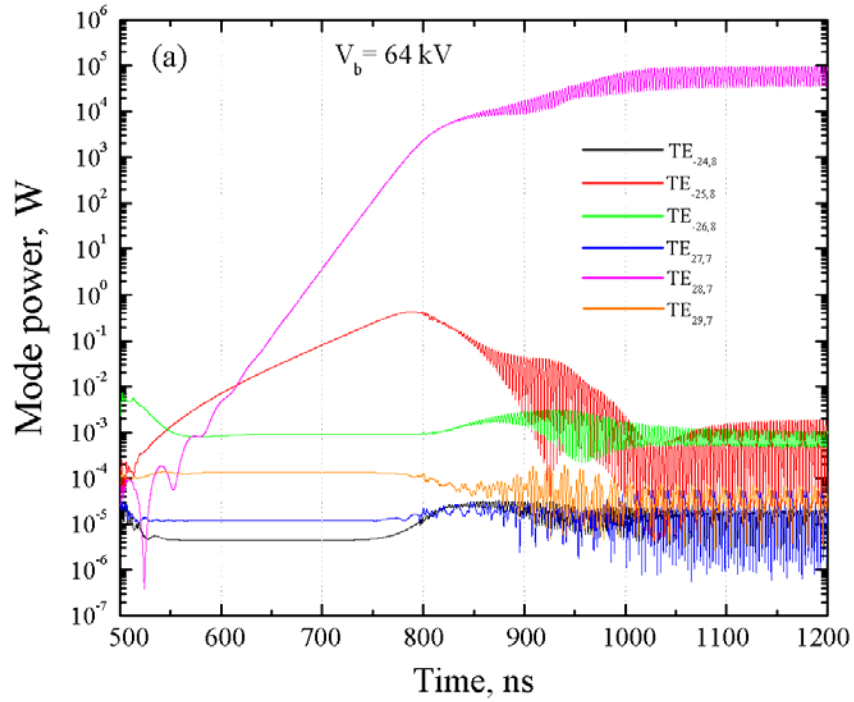
Fig. 3.5. Evolution of modes at the final stage of startup scenario allowing additional time for the modes to reach steady state. (a) Results of the long run at 64 kV. (b) Increase in the power of the desired mode with the further increase in voltage up to the nominal level.

3.3.3: Simulation results for the 110 GHz, 1.5 MW CPI gyrotron

In an effort to produce a gyrotron design that is both more reliable and cost effective for large fusion installation such as U.S. tokamak "Doublet-IIID" [79], a new 110 GHz design has been developed at CPI that has a power-handling capability of 1.5 MW. The circuit geometry and magnetic field profile for this gyrotron are shown in Fig. 3.6. The operating mode is $TE_{22,6}$, the operation is at the first cyclotron harmonic. The accelerating voltage is 96 kV, the corresponding beam current is 40 A and the orbital-to-axial velocity ratio is about 1.4.
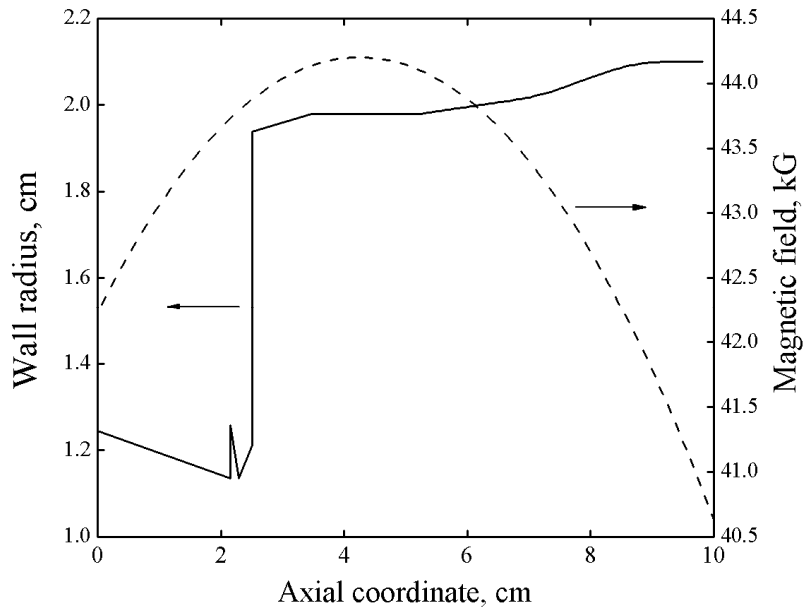
Fig. 3.6. Circuit geometry (solid) and magnetic field profile (dash)
for the 110 GHz, 1.5 MW gyrotron developed at CPI.

The most important competing modes are $TE_{21,6}$ and $TE_{23,6}$, which form a triplet with the operating mode. The eigenvalues of these modes can be found to be

$v_{21,6} = 44.403$, $v_{22,6} = 45.6243$ and $v_{23,6} = 46.8407$, and the corresponding

nonequidistance of cutoff frequencies is

$$| 2 \cdot v_{22,6} - v_{21,6} - v_{23,6} | / v_{22,6} \approx 1.1 \cdot 10^{-4},$$

which satisfies the conditions (3.1) and (3.2) for the *Q*-factor being equal to 10^3. The

counterrotating triplet is formed by the modes with radial index $p = 7$: *TE*-18,7, *TE*-19,7

and *TE*-20,7. The radial profile of the coupling impedance for the six modes is shown

in Fig. 3.7. As before, red and green colors in the figure correspond to corotating and

counterrotating modes, respectively. We were considering two beam positions in our
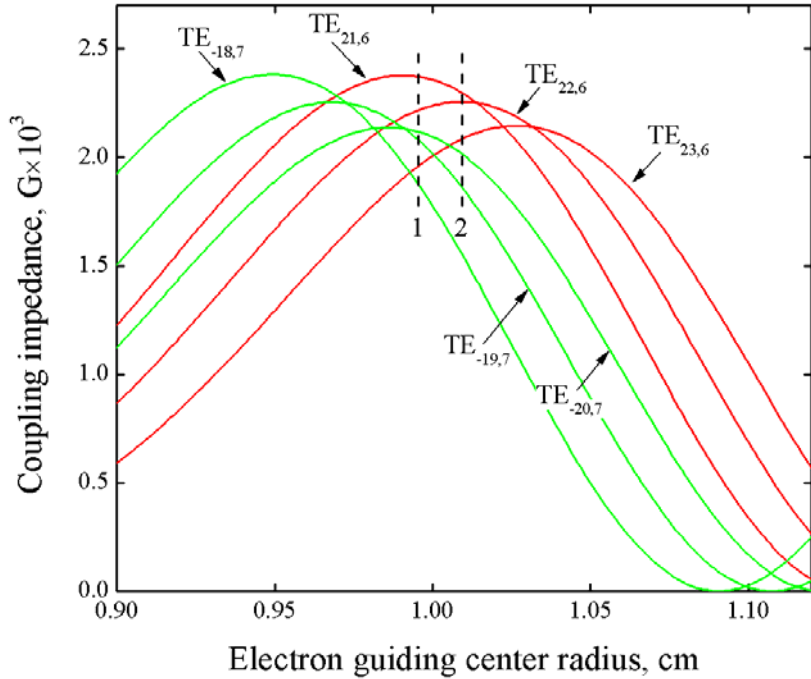
Fig. 3.7. Coupling impedances of the corotating (red) and counterrotating (green) modes in the vicinity of the beam positions (dashed) as functions of the electron guiding center radius.

analysis, which are shown by dashed lines with the corresponding indices. The first

position was initially used by the CPI during the test simulations for this tube. As we

will see, this position results in the excitation of the parasitic $TE_{-19,7}$-mode instead of the desired $TE_{22,6}$-mode.

The imaginary part of the susceptibility versus frequency is shown in Fig. 3.8. It can be seen in this figure that the high-frequency $TE_{23,6}$ and $TE_{-20,7}$ modes should be excited at about 56 kV during the voltage rise. Then, the central modes of both triplets, $TE_{22,6}$ and $TE_{-19,7}$, should start growing near 74 kV and, finally, the low-frequency $TE_{21,6}$ and $TE_{-18,7}$ will enter the game when the voltage reaches 88-90 kV.
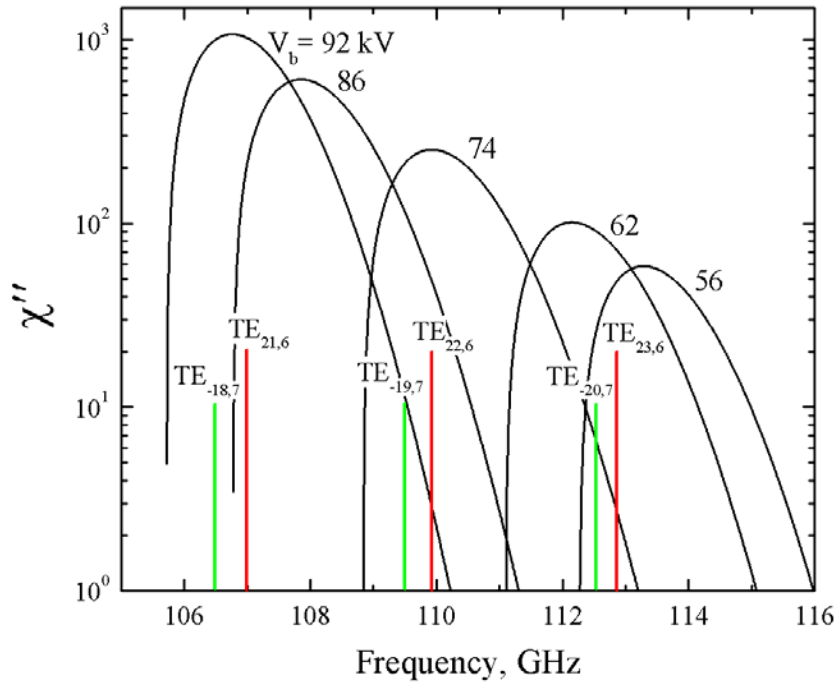
Fig. 3.8. Preliminary calculations for the CPI 110 GHz gyrotron. Imaginary part of the beam susceptibility as a function of the operating frequency for several values of the accelerating voltage. The mode cutoff frequencies of the corotating and counterrotating triplets are shown by the red and green vertical lines, respectively.

Corresponding MAGY simulations for the first beam location are shown in Fig. 3.9. As before, the length of each run corresponding to a fixed voltage value was

100 ns and the voltage was increasing in 2 kV steps. The cross section, at which the results were obtained, was located at z = 9.82 cm, i.e. at the end of the output section (see Fig. 3.6). One may see that instead of only high-frequency modes, all three modes of the corotating triplet exist above the noise level at initial voltages. Then, when the voltage is about 54 kV, the high-frequency $TE_{23,6}$ mode starts suppressing the operating $TE_{22,6}$ mode slightly. At the same time, at 56-58 kV, the central mode of the counterrotating triplet, $TE_{-19,7}$, begins to grow replacing the operating one. It is interesting to notice that magnitudes of the operating and the high-frequency counterrotating $TE_{-20,7}$ modes oscillate with the same frequency of about 40 MHz when the voltages are between 58 and 62 kV. At 64 kV, the $TE_{-19,7}$ and $TE_{22,6}$ start growing very rapidly, however they differ in power by almost two orders. The growth of these modes provokes a similar growth of the low-frequency $TE_{21,6}$ mode. The growth of the central modes stops at 70 kV where they experience a small drop, while the $TE_{21,6}$ continues to grow and drops only at 72 kV. At this voltage, the $TE_{-19,7}$ and $TE_{-20,7}$ start rising again competing between each other. The counterrotating mode wins this competition, while the operating mode gets suppressed and starts dropping at 78 kV. All other modes also become suppressed and drop to the noise level. The parasitic $TE_{-19,7}$ reaches the point of its maximum efficiency at the final voltage.

As can be seen in the Fig. 3.9, the modes did not reach the steady state at most of the voltage values. Therefore, the results obtained were checked in longer runs. These are shown in Fig. 3.10. It can be noticed immediately that there is a significant difference in mode behavior in both figures. At first, the results for initial voltage values in Fig. 3.10 (a) are comparable with those in Fig 3.9 (a). Indeed, one may see

Fig. 3.9. Startup scenario for the 110 GHz, CPI gyrotron. The results are obtained for the first beam position shown in Fig. 3.7. The beam voltage varies in 2 kV steps. For each voltage value, the simulations are conducted for 100 ns. The voltage values are indicated in the figures.

that the $TE_{23,6}$ and $TE_{21,6}$ modes are growing slowly suppressing the operating $TE_{22,6}$, while the $TE_{-20,7}$ mode is oscillating with the frequency about 35-40 MHz. Such oscillations can be noticed in both Fig. 3.9 (a) and Fig. 3.10 (a). However, starting from the value of 58 kV, an absolutely different behavior can be seen in Fig. 3.10 (a). The high-frequency $TE_{-20,7}$ and $TE_{23,6}$ modes in this figure start growing relatively fast and eventually reach significant power levels. One may notice that although the cutoff frequency of the $TE_{-20,7}$-mode is lower than the one for the $TE_{23,6}$-mode, it is excited first possibly because the value of its coupling impedance is larger for the given beam radius (see Fig. 3.7). Both $TE_{-20,7}$ and $TE_{23,6}$ are growing slowly at 58 kV (Fig. 3.10 (b)) and reach saturation in about 4.5 μs. As can be seen from Fig. 3.9 (a), this growth was not predicted in the short runs. Also, it is interesting to notice that the modes with lower frequencies in Figs. 3.10 (a) and 3.10 (b) do not interact and remain stable during this rise. The two high-frequency modes start falling at 60 kV (Fig. 3.10 (b)), while the central $TE_{-19,7}$-mode experiences a small rise. As can be seen in Figs. 3.10 (b), 3.10 (c) and 3.10 (d), the $TE_{-20,7}$ and $TE_{23,6}$ modes fall to the level of other modes in about 9 μs. Then, at 62 kV, the $TE_{-19,7}$-mode continues to rise while the operating mode starts oscillating with a slowly increasing amplitude. It can be noticed that for these central modes, the $TE_{-19,7}$ is excited prior to the $TE_{22,6}$-mode although it couples to the beam slightly weaker. One may see in Figs. 3.10 (e) and (f) that the $TE_{-19,7}$-mode reaches the saturation at this voltage value in about 7 μs. The oscillations of the operating mode die away at the end of this time interval. At subsequent voltage steps, the parasitic $TE_{-19,7}$-mode continues to grow suppressing all other modes and reaches its highest efficiency at 96 kV (Fig. 3.10 (g)). These results
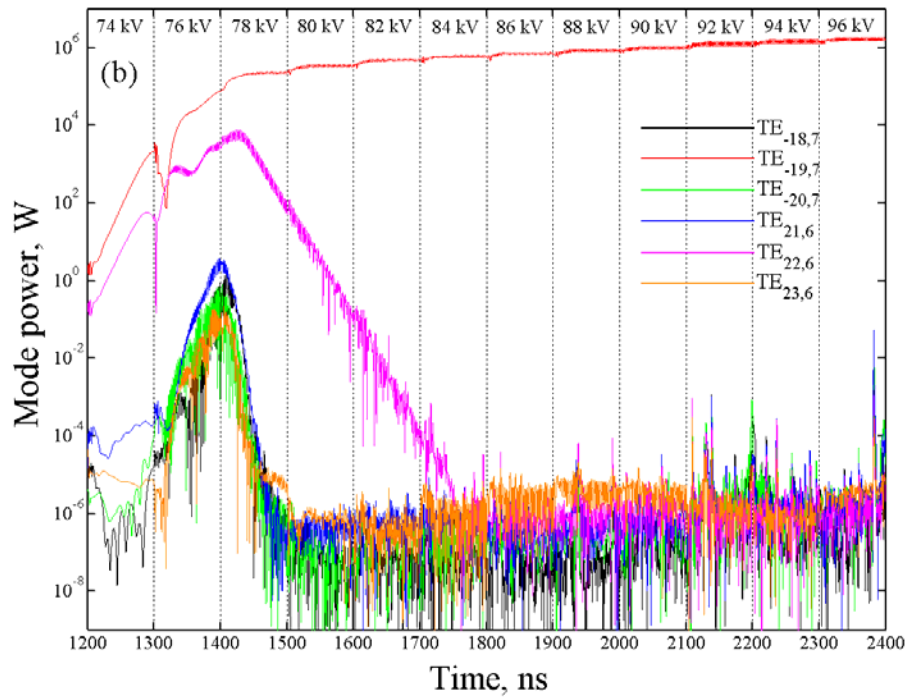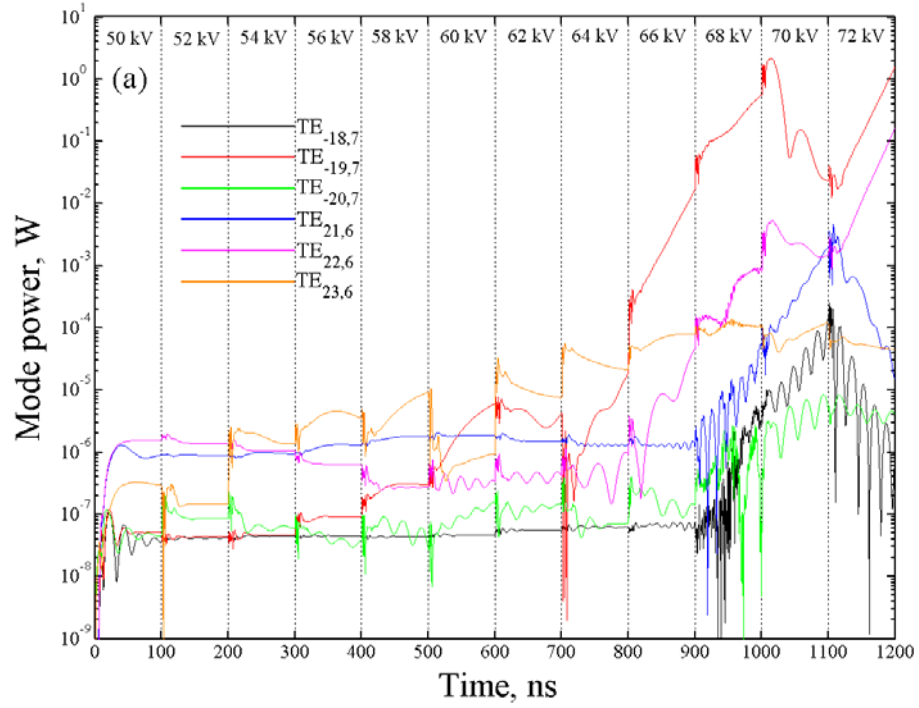
107

Fig. 3.10. Startup scenario for the 110 GHz, 1.5 MW CPI gyrotron. The results are obtained for the first beam position shown in Fig. 3.7. The length of the runs at each beam voltage value allows the modes to reach steady state. The voltage varies in 2 kV steps, which are indicated in the figure.

Fig. 3.10. (cont.)

109
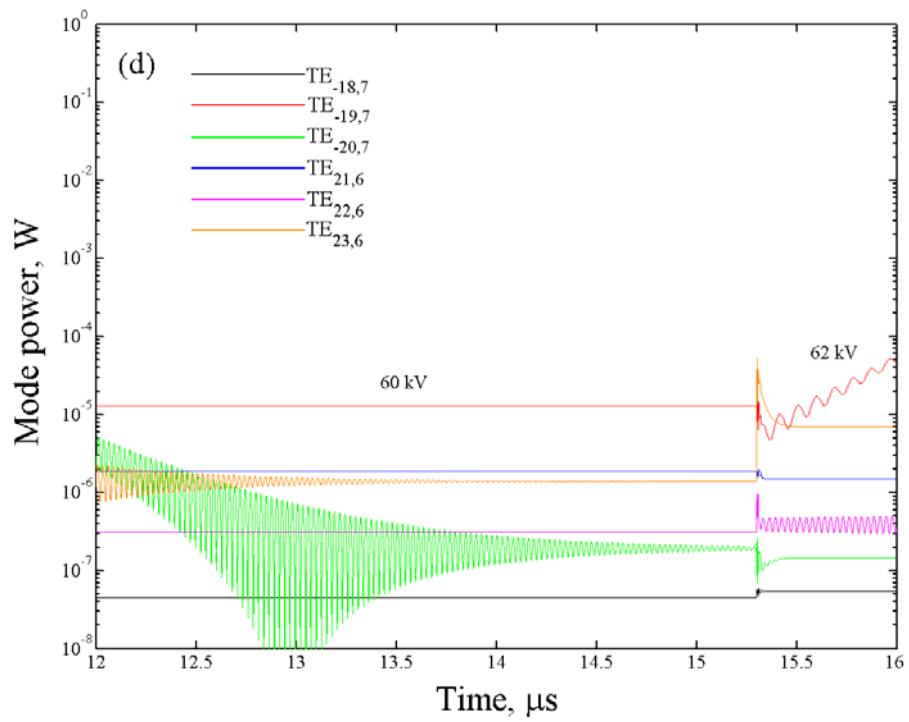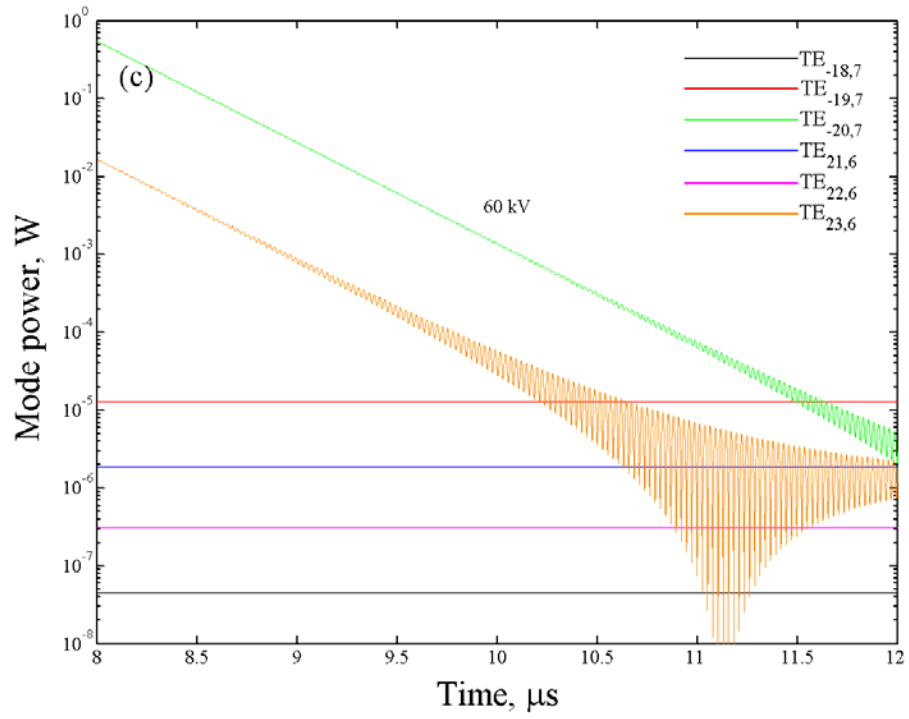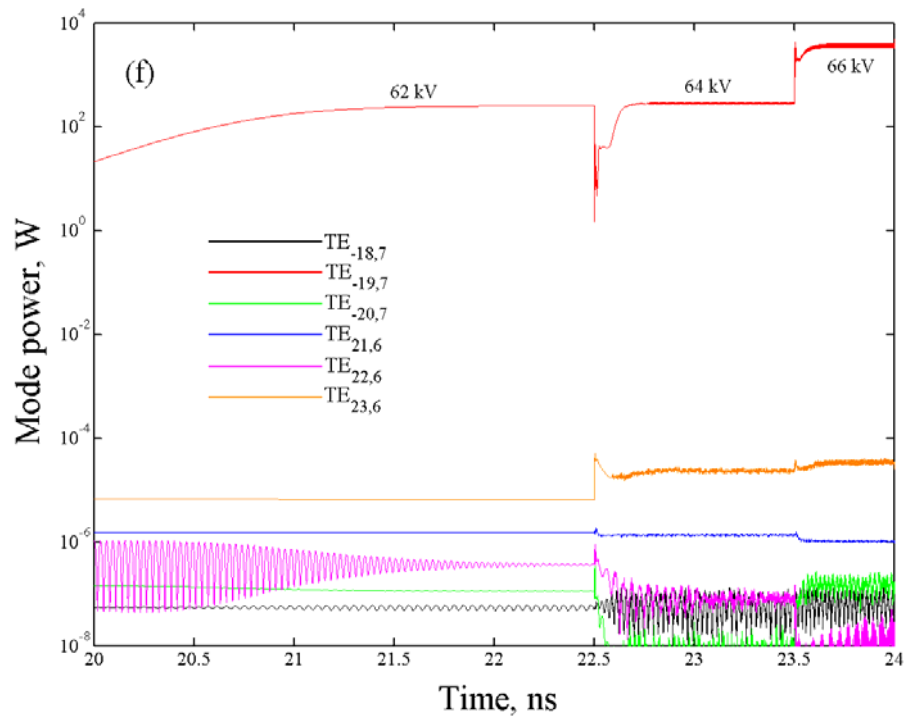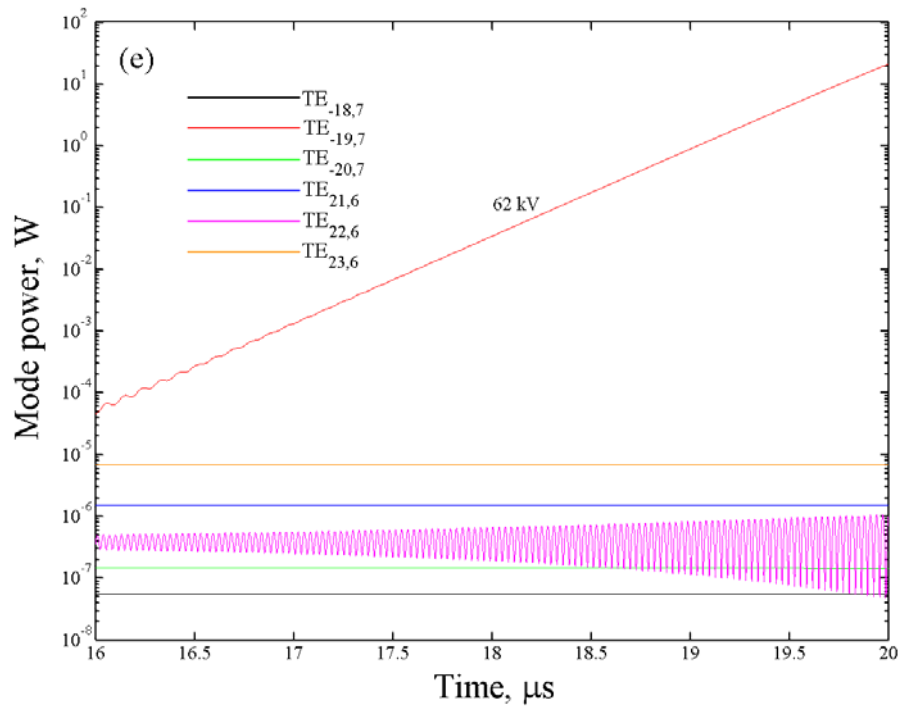
Fig. 3.10. (cont.)
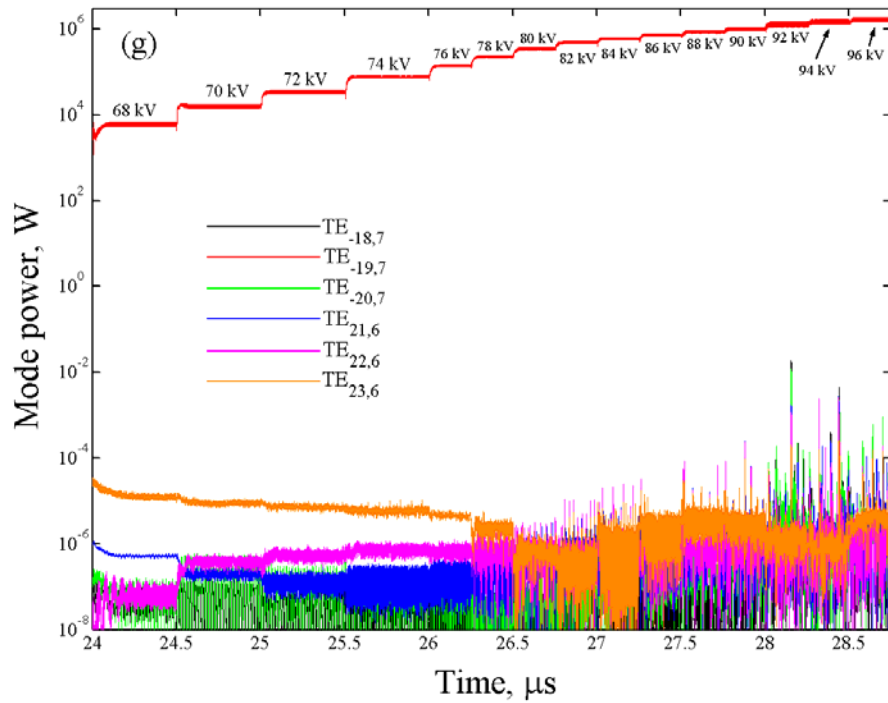
Fig. 3.10. (cont.)

are also in contradiction with the ones obtained by short runs, although the operation of the $TE_{-19,7}$-mode at the final stage has been predicted for both simulations. A keen mode competition can be observed between 68 kV and 78 kV in Fig. 3.9, which is absent in Fig. 3.10. Also, the operating $TE_{22,6}$-mode reaches almost 10 kW level at 78 kV in Fig. 3.9 (b), whereas it barely gets to 1 μW in Figs. 3.10 (f) and 3.10 (g). As in the case of the 140 GHz gyrotron, we may conclude that the predicted mode behavior is quite sensitive to the rate of the voltage rise.

Since the operation of the desired $TE_{22,6}$-mode was not achieved, we changed the beam radius from 0.996 cm to 1.01 cm (see Fig. 3.7). Correspondingly, the ratio of the coupling impedance of the operating mode to the one of the most dangerous $TE_{-19,7}$-mode changed from 1.066 to 1.211. The results of short runs for the second
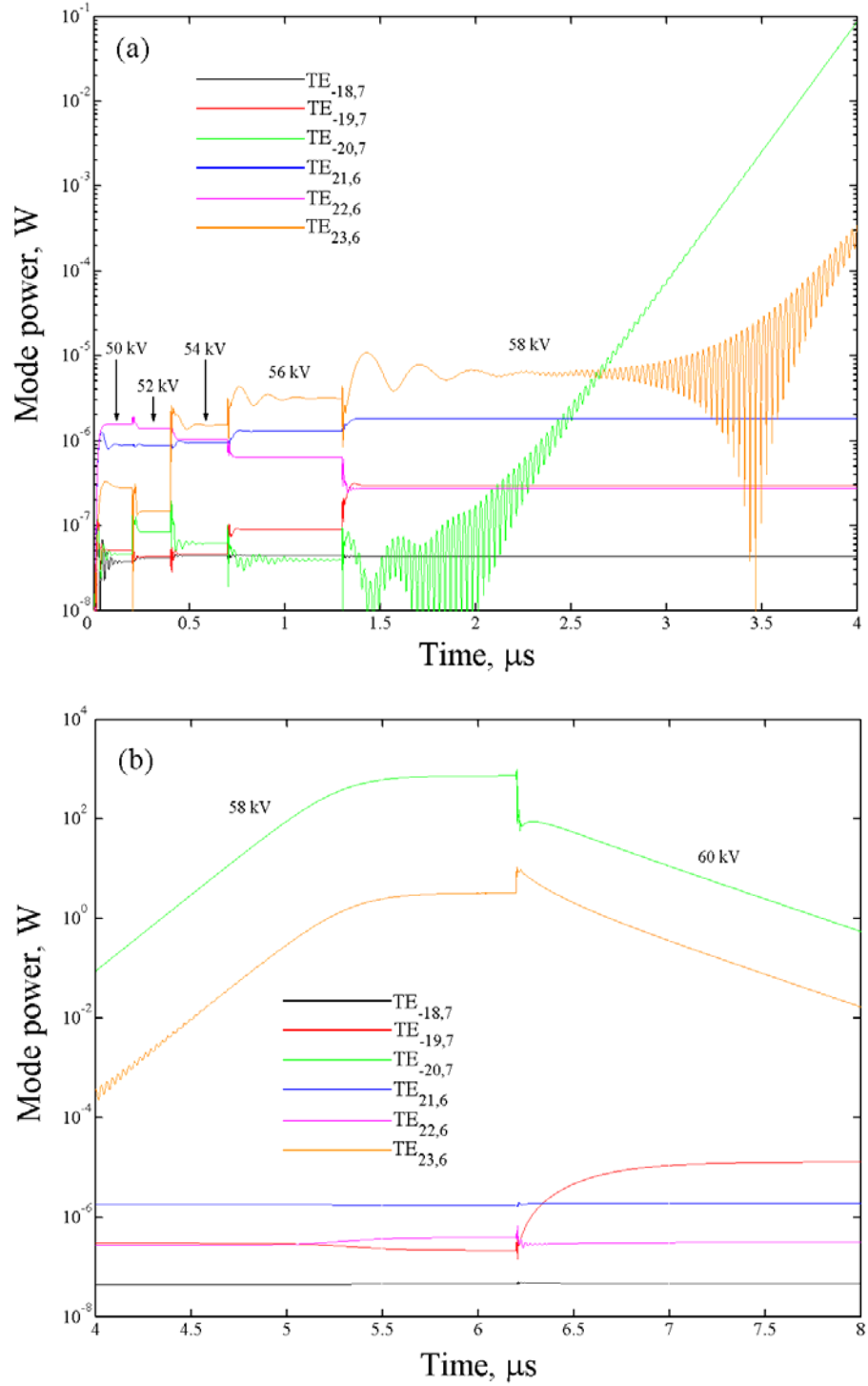
111
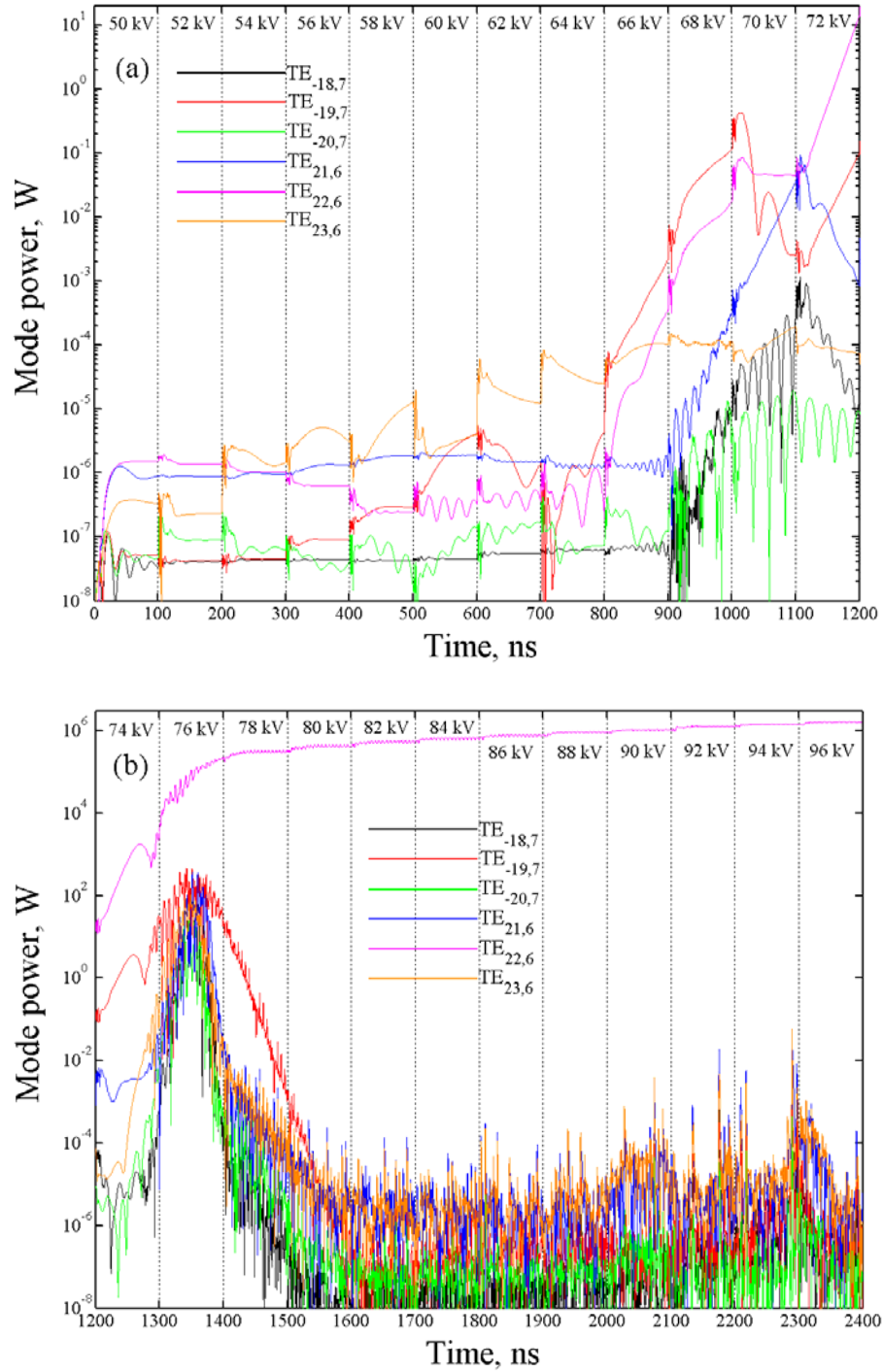
Fig. 3.11. Startup scenario for the 110 GHz, CPI gyrotron. The results are obtained for the second beam position shown in Fig. 3.7. The beam voltage varies in 2 kV steps. For each voltage value, the simulations are conducted for 100 ns. The voltage values are indicated in the figures.

beam radius are shown in Fig. 3.11. In this figure, one may observe a severe mode competition in the range of beam voltages from 66 kV to 78 kV, which is similar to the one shown in Fig. 3.9. However, the operating $TE_{22,6}$-mode wins in this case and successfully reaches its maximum efficiency at 96 kV. It is interesting to notice that the parasitic $TE_{-19,7}$-mode starts growing before the operating one and has a higher power at 64-68 kV but still loses its advantage at 70 kV. (It should be mentioned that a smaller beam radius than the one shown in Fig. 3.2 was initially employed for the 140 GHz gyrotron. But it was found in a series of simulations [80] and experiments that the parasitic $TE_{-25,8}$-mode was suppressing the desired $TE_{28,7}$-mode under those conditions).

As in the results for the first beam radius, the modes did not reach steady state in the majority of runs and, therefore, the results should be verified in long simulations. These simulations are currently in progress.

A few important conclusions can be made based on the results of our simulations. First of all, they show that it is necessary to consider the time scale of the voltage rise when attempting to predict the outcome of a startup scenario, because the sequence of modes that can be excited, and their final power levels can be quite different depending on whether the voltage rises slowly or rapidly relative to the rise times of the modes themselves. This means, in particular, that the results of short-pulse tests of gyrotrons operating in high-order modes may not be reproducible in long-pulse tests of the same tubes. Second, these results show that to predict the final power levels of various modes, it is necessary to track the behavior of the oscillator starting from a voltage, at which the first mode can be excited from the noise level, up

to the nominal voltage. Third, in the case of exciting many modes, it is often necessary to consider the temporal mode evolution during the intervals much longer than the saturation time, which was estimated above for a single-mode excitation. Our results also show that a simultaneous treatment of two triplets was absolutely necessary for determining details of mode excitation and interaction. Finally, it should be emphasized that the results of our simulations agree qualitatively with experiments conducted at CPI.

3.4: Slow stage of startup scenarios

3.4.1: Slow processes in CW and long-pulse gyrotrons

Recently, attention has been paid [81]-[83] to the fact that in CW and long-pulse gyrotrons some slow processes may take place, whose typical time is much larger than the voltage rise time and whose presence can be important for stability of gyrotron operation. In this section, we will discuss the following three effects:

1) ion neutralization of DC space charge fields;

2) frequency deviation caused by the temperature rise of cavity walls due to the ohmic heating;

3) the decrease of the beam current due to cathode cooling.

Ion neutralization. Initially, an electron beam is injected into the interaction space, which contains a small amount of the residual gas. There is a certain clearance between the cavity wall and the electron beam, which is immersed at the position close to the caustic radius, $R_c = m / \nu_{m,p}$ of the high-order $TE_{m,p}$-mode. This clearance determines the depression of the beam potential with respect to the wall potential due to the DC beam space charge forces. In gyrotrons, which operate in the range of voltages between 80 kV and 100 kV, this voltage depression, δV , is typically of the order of several kV. Collision of beam electrons with the molecules of residual gas creates ions and electrons, with the latter ones quickly escaping to the cavity walls because of the beam space charge force. Then, the ions compensate the DC space charge of an electron beam and the beam potential reaches its nominal value

determined by the applied voltage. Certainly, the time of this process depends on the initial gas pressure, but typically it is on the order of hundred milliseconds [84] or even seconds [82], [85].

Frequency deviation. The ohmic losses of microwave power in the cavity wall cause a certain thermal expansion of the walls, which in its turn decreases the frequency of radiation. Typically, the shift of the operating frequency due to this effect is of the order of several hundred MHz and it usually occurs during the interval of hundreds of milliseconds. This interval depends on the cavity wall thickness and the cooling conditions. The frequency change is reversible if the operation is under normal cooling conditions. In this case, the cavity shape remains unchanged after long-pulse operation. The cavity geometry changes [86] in the case of excessive wall loading (ohmic losses of the order of several kW/cm^2 or more) and this affects not only the mode frequency, but also its quality factor Q [84].

Cathode cooling. In some tubes, the effect known as cathode cooling was observed in the long-pulse operation. This effect means a slow decrease of the electron current. For example, in the 170 GHz ITER gyrotron studied at JAERI [83], the beam current decreased from 35 A at the beginning of the pulse to 25 A at the end.

As mentioned in Section 3.1, the most efficient gyrotron operation is often possible only in the regime of hard self-excitation, where the optimum beam current is smaller than the starting current. As discussed elsewhere [87], another characteristic current for such regime is the minimum current, at which the oscillations can be stable. This current is smaller than the optimum one, but if the

116

beam current experiences a large decrease and at some point becomes smaller than this minimum current, then the oscillations of a given mode will loose the stability. In this case, the oscillator operating at a high-order mode exhibits a hopping to a lower frequency mode, which can be excited in the soft self-excitation regime in this case. This mode hopping was observed in Ref. 83.

3.4.2: Analysis of the effects

Let us analyze the processes just discussed by the use of a simple general theory based on the use of gyro-averaged equations of electron motion and cold-cavity approximation for the resonator field presented in Section 3.2.

The effects of ion compensation and frequency shift affect, first of all, the cyclotron detuning $\Delta = (2/\beta_{\perp 0}^2)(1 - s\Omega_0/\omega)$, because the ion compensation changes the electron energy, $\gamma_0 = 1 + eV_b/mc^2$, and, hence, the cyclotron frequency Ω_0, while the frequency deviation changes the operating frequency ω. Corresponding changes in the cyclotron resonance detuning can be given as

$$\delta\Delta = \frac{2}{\beta_{\perp 0}^2}\left[\frac{\Delta\omega}{\omega} + \frac{V_{b,comp} - V_{b,depr}}{mc^2/e + V_b}\right]. \tag{3.28}$$

Here $V_{b,depr}$ and $V_{b,comp}$ are the beam potentials before and after the ion compensation of the voltage depression, respectively. As follows from this equation, the frequency deviation, which is typically of the order of 0.1-0.2%, in the gyrotron driven by a 96 kV electron beam with the orbital-to-axial velocity ratio of 1.4 causes the reduction of the detuning parameter by about 0.01-0.02. Also, the voltage drop in such beam, as

117

show simulations for the 1.5 MW, 110 GHz CPI gyrotron, is about 4.6 kV. Then, Eq. (3.28) predicts that the ion compensation of this voltage depression should increase the detuning by 0.0785.

To illustrate the importance of these changes, the dependence of the orbital efficiency upon the cyclotron detuning Δ is shown in Fig. 3.12 for several values of the normalized interaction length μ for a gyrotron with a Gaussian axial distribution of the RF field. As follows from this figure, the increase in Δ by about 0.08 from its optimal value does not lead to the loss of oscillation stability when the normalized length μ does not exceed 14 – corresponding maximum value of the orbital efficiency
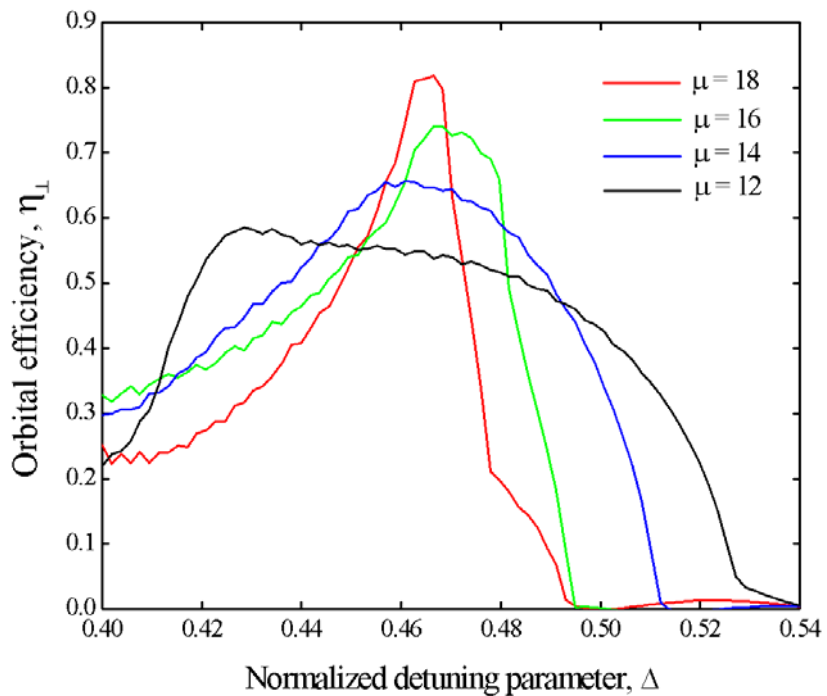
Fig. 3.12. Orbital efficiency as a function of the normalized detuning parameter for several normalized interaction lengths.

is close to 65 %. However, in the regimes providing the maximum orbital efficiency – over 80% for $\mu = 18$ – such shift in Δ is too large for sustaining stable oscillations.

This conclusion about necessity to have the normalized length not exceeding 14 agrees with a similar conclusion ($\mu < 13$) made on the basis of the analysis of the stability of single-mode oscillations in multimode gyrotrons [69].

In Fig. 3.13 the dependence of the orbital efficiency on the normalized beam current parameter is given for several values of the normalized length μ; the cyclotron resonance detuning is chosen to maximize the efficiency at the peak point of $\eta_\perp(I_0)$
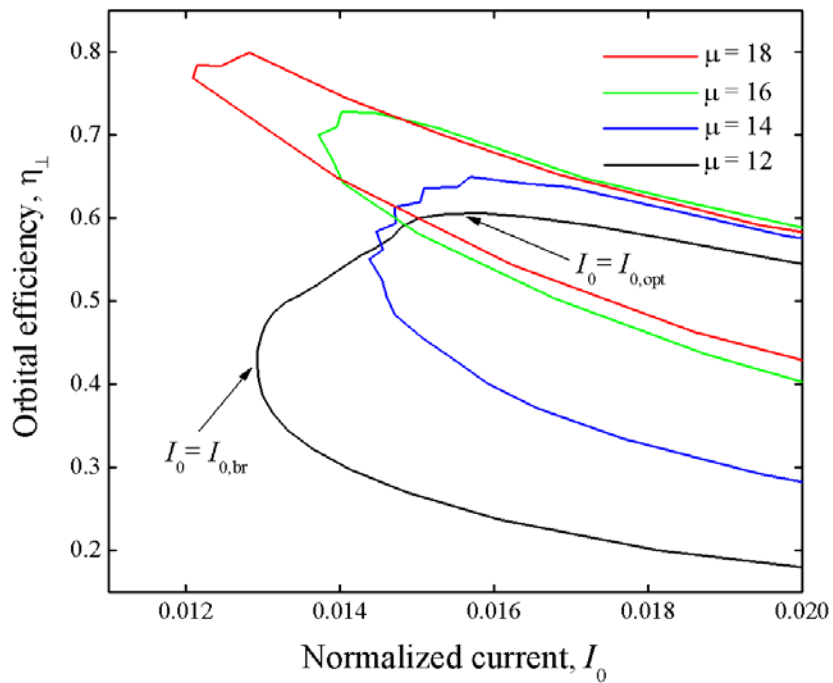
Fig. 3.13. Orbital efficiency of interaction versus the normalized current parameter for several values of the interaction length. The cyclotron resonance detuning is chosen to maximize the efficiency at the peak point. The optimum and break currents are indicated in the figure for $\mu = 12$.

for each μ. (This plot is similar to those shown in Ref. 60.) This dependence again shows that when the operating parameters approach their optimal values the requirements for their deviation become more stringent. Indeed, considering the

difference δI between the current corresponding to maximum efficiency, $I_{0,opt}$, and

the break current, $I_{0,br}$ (see Fig. 3.13), below which the oscillations become unstable,

one may see that for the case of $\mu = 18$, the cathode cooling should not reduce the

beam current by more than 5%. However, in the case of $\mu = 12$ the allowed cathode

cooling is close to 17% of the nominal beam current.

Fig. 3.14 summarizes the results presented in Fig. 3.13. It shows the

dependence of the ratio $\delta I / I_{0,opt} = (I_{0,opt} - I_{0,br}) / I_{0,opt}$ on the normalized length μ. It

can be seen that in order to provide stable operation, the interaction length should be

equal to or less than 14. This conclusion agrees with the one based on the results

shown in Fig. 3.13.
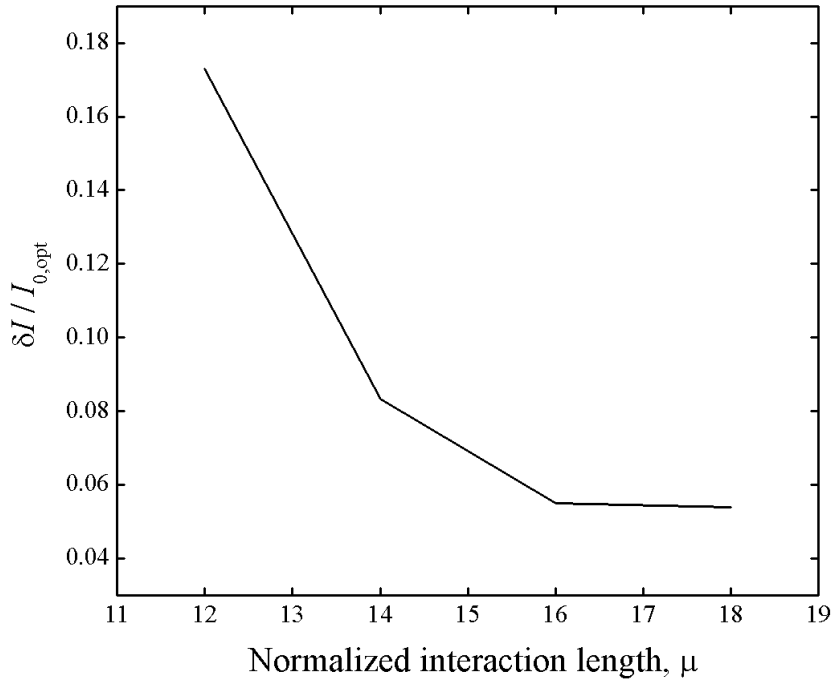
Fig. 3.14. The difference between the optimum and break
currents related to the optimum current as a function of
the normalized interaction length.

For the sake of comparison, we have modeled the effect of cathode cooling with MAGY for the 110 GHz, CPI gyrotron. The results are shown in Fig. 3.15. We started the simulations from the optimum operating point corresponding to $V_b = 96$ kV and $I_b = 40$ A (see Fig. 3.11). Then, by gradually reducing the beam current, the
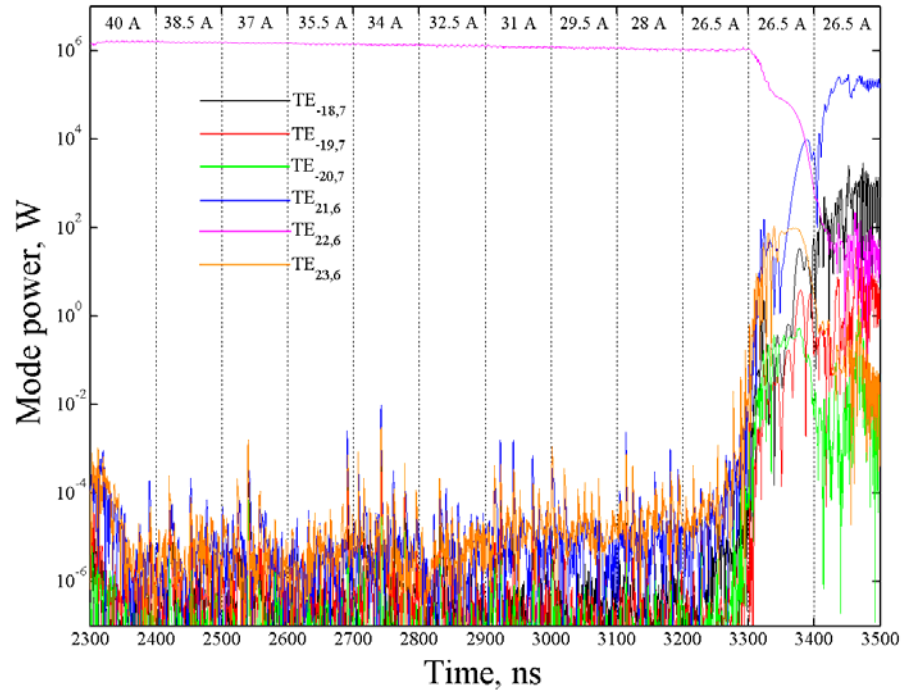
Fig. 3.15. The cathode cooling effect simulated by using MAGY for the 110 GHz, CPI gyrotron.

point where the operating $TE_{22,6}$-mode loses its stability was reached. As one may see, it occurs at $I_b \approx 26.5\,\text{A}$ (i.e. the current decrease is about 34%), where the operating mode is replaced by the low-frequency $TE_{21,6}$-mode. Similar results were obtained for the 170 GHz long-pulse gyrotron developed at JAERI [83]. The beam current decreased from 35 A to 25 A (i.e. the decrease was about 29%) for that tube and the operating $TE_{31,8}$-mode was replaced by the $TE_{30,8}$-mode. Since the normalized length μ is usually chosen to be about 13-14 for most gyrotrons, one may see that the

permissible current decrease predicted by MAGY is much larger than the one shown in Fig. 3.14 for the same interaction length. Such discrepancy may be attributed to the fact that the axial field distribution in real tubes can differ from the Gaussian one significantly, whereas we used the Gaussian profile in our simple theory.

Summary

Gyro-TWTs. The results of both linear and nonlinear analyses of two-stage gyro-TWTs with distributed losses have been presented. The effect of distributed losses on the gain and bandwidth of the devices has been studied and the analysis of starting conditions for excitation of the backward waves has been carried out. It has been shown that the presence of losses in the interaction region of a gyro-TWT allows eliminating of the parasitic BW oscillations in the device. Examples have been considered which show that predictions of both linear and nonlinear theories may agree well with the results of a thorough numerical analysis based on the use of accurate codes.

The nonlinear theory of gyro-TWT with tapered parameters has been developed. A particular configuration of a gyro-TWT has been analyzed within the theory. The results of this analysis demonstrated that the bandwidth and gain-bandwidth product of the device can be significantly enlarged by the use of waveguide wall tapering only.

Gyroklystrons. Conventional and clustered-cavity GKLs with the same number of cavities in both schemes have been compared. The gain studies showed that for the case of limitations on the length of the device and the beam current, the clustered-cavity scheme is preferable. Studies of the bandwidth properties showed that the use of clustered cavity approach allows one to achieve much larger bandwidths in comparison with the conventional scheme.

Startup scenarios in high-power gyrotrons. The startup scenarios of two MW-class gyrotrons developed at CPI have been simulated. The operation at the desired mode and power level has been demonstrated for both devices. It has been shown that it is necessary to consider the time scale of the voltage rise when attempting to predict the outcome of the startup scenario. Also, we have demonstrated that a simultaneous treatment of two triplets is absolutely necessary for determining details of mode excitation and interaction. The results agree well with the experiments conducted at CPI.

Some slow processes in CW and long-pulse gyrotrons have been considered. The effects of frequency deviation caused by cavity temperature expansion and decrease of beam current due to cathode cooling have been analyzed by the use of a simple nonlinear theory. It has been shown that these effects can be critical in the devices with a long interaction region.

A detailed description of some results presented in this work can be found in the following publications:

1) G.S. Nusinovich, O.V. Sinitsyn and A. Kesar, "Linear theory of gyro-traveling-wave tubes with distributed losses," *Phys. Plasmas*, vol. 8, pp. 3427-3433, 2001.

2) O.V. Sinitsyn, G.S. Nusinovich, K.T. Nguen, and V.L. Granatstein, "Nonlinear theory of the gyro-TWT: Comparison of analytical method and numerical code data for the NRL gyro-TWT," *IEEE Trans. Plasma. Sci.*, vol. 30, pp. 915-921, 2002.

3) O.V. Sinitsyn, G.S. Nusinovich and V.L. Granatstein, "Comparison of two concepts: Multi-cavity versus clustered-cavity gyroklystrons," *Proc. 6th Workshop on High Energy Density and High Power RF.*, Berkeley Springs, WV, 2003, AIP Conf. Proc. 691, pp. 378-385, 2003.

4) G. S. Nusinovich, O. V. Sinitsyn, M. Yeddulla, L. Velikovich, T. M. Antonsen, Jr., A. N. Vlasov, S. Cauffman, and K. Felch, "Effect of the radial thickness of

electron beams on mode coupling and stability in gyrotrons," *Phys. Plasmas*, vol. 10, pp. 3335-3343, 2003.

5) G.S. Nusinovich, O.V. Sinitsyn, J. Rodgers, T. M. Antonsen, Jr., V.L. Granatstein, and N.C. Luhmann, Jr., "Comparison of multistage gyroamplifiers operating in the frequency-multiplication regime with gyroamplifiers operating at a given cyclotron harmonic," *IEEE Trans. Plasma. Sci*., vol. 32, pp. 957-969, 2004.

6) G.S. Nusinovich, O.V. Sinitsyn, L. Velikovich, M. Yeddulla, T.M. Antonsen, Jr., A.N. Vlasov, S.R. Cauffman, and K. Felch, "Startup scenarios in high-power gyrotrons," *IEEE Trans. Plasma. Sci*., vol. 32, pp. 841-852, 2004.

Bibliography

[1] R. O. Twiss, "Radiation transfer and the possibility of negative absorption in radio astronomy," *Aust. J. Phys.,* vol. 11, pp. 567–579, 1958.

[2] J. Schneider, "Stimulation emission of radiation by relativistic electrons in a magnetic field," *Phys. Rev. Lett.,* vol. 2, pp. 504–505, 1959.

[3] R. H. Pantell, "Backward wave oscillation in an unloaded waveguide," *Proc. IRE,* vol. 47, p. 1146, 1959.

[4] A. V. Gaponov, "Interaction between irrectilinear electron beams and electromagnetic waves in transmission lines," *Izv. VUZov. Radiofiz.*, vol. 2, pp. 836–837, 1959.

[5] K. K. Chow and R. H. Pantell, "The cyclotron resonance backward wave oscillator," *Proc. IRE,* vol. 48, pp. 1865–1870, 1960.

[6] J. L. Hirshfield and J. M. Wachtell, "Electron cyclotron maser," *Phys. Rev. Lett.,* vol. 12, pp. 533–536, 1964.

[7] I. I. Antakov, V. M. Bokov, R. P. Vasilyev, and A. V. Gaponov, "Interaction of a trochoidal electron beam with an electromagnetic wave in a rectangular waveguide," *Izv. VUZov. Radiofiz.,* vol. 3, p. 1033, 1960.

[8] A. V. Gaponov, M. I. Petelin, and V. K. Yulpatov, "The induced radiation of excited classical oscillators and its use in high frequency electronics," *Radiophys. Quantum Electron.,* vol. 10, pp. 794–813, 1967.

[9] V. L. Granatstein, M. Herndon, R. K. Parker, and P. Sprangle, "Coherent synchrotron radiation from an intense relativistic electron beam," *IEEE J. Quantum Electron.,* vol. QE-10, p. 651, 1974.

[10] V. L. Granatstein, P. Sprangle, M. Herndon, R. K. Parker, and S. P. Schlesinger, "Microwave amplification with an intense relativistic electron beam," *J. Appl. Phys.,* vol. 46, pp. 3800–3805, 1975.

[11] V. L. Granatstein, M. Herndon, P. Sprangle, Y. Carmel, and J. A. Nation, "Gigawatt microwave emission from an intense relativistic electron beam," *Plasma Phys. Control. Fusion,* vol. 17, pp. 23–28, 1975.

[12] A. V. Gaponov, A. L. Goldenberg, M. I. Petelin, and V. K. Yulpatov, "A device for cm, mm, and submm wave generation," *Official Bull. KDIO of SM USSR,* no. 11, p. 200, 1976.

[13] V. V. Alikaev, G. A. Bobrovskii, M. M. Ofitserov, V. I. Poznyak, and K. A. Razumova, "Electron-cyclotron heating on the Tokamak TM-3," *JETP Lett.,* vol. 15, pp. 27–31, 1972.

[14] N. I. Zaytsev, T. B. Pankratova, M. I. Petelin, and V. A. Flyagin, "Millimeter- and submillimeter-wave gyrotrons," *Radio Eng. Electron. Phys.,* vol. 19, pp. 103–107, 1974.

[15] D. V. Kisel, G. S. Korablev, V. G. Pavel'yev, M. I. Petelin, and Sh. Ye. Tsimring, "An experimental study of a gyrotron operating at the second harmonic of the cyclotron frequency with optimized distribution of the high-frequency field," *Radio Eng. Electron. Phys.,* vol. 19, pp. 95–100, 1974.

[16] A. V. Gaponov, A. L. Goldenberg, D. P. Grigor'ev, T. B. Pankratova, M. I. Petelin, and V. A. Flyagin, "An experimental investigation of cm wave gyrotrons," *Izv. VUZov. Radiofiz.,* vol. 18, pp. 280–289, 1975.

[17] Yu. V. Bykov, A. F. Goldenberg, L. V. Nikolaev, M. M. Ofitserov, and M. I. Petelin, "An experimental investigation of a gyrotron with whispering-gallery modes," *Izv. VUZov. Radiofiz.,* vol. 18, pp. 1544–1547, 1975.

[18] M. E. Read, R. M. Gilgenbach, R. Lucey, K. R. Chu, A. T. Drobot, and V. L. Granatstein, *IEEE Trans. Microwave Theory Tech.,* vol. MTT-28, pp. 875–878, 1980.

[19] A. V. Gaponov, "Relativistic dispersion equations for waveguide systems with helical and trochoidal electron beams ," *Izv. Vyssh. Uchebn. Zaved., Radiofiz.,* vol. 4, pp. 547-560, 1961 (In Russian).

[20] V. K. Yulpatov, "Nonlinear theory of the interaction between a periodic electron beam and an electromagnetic wave," *Radiophys. Quantum Electron.,* vol. 10, pp. 471-476, 1967.

[21] K. R. Chu, A. T. Drobot, V. L. Granatstein, and J. L. Seftor, "Characteristics and optimum operating parameters of a gyrotron traveling-wave amplifier," *IEEE Trans. Microwave Theory Tech.,* vol. 27, pp. 178-187, 1979.

[22] K. R. Chu, A. T. Drobot, H. H. Szu, and P. Sprangle, "Theory and simulation of the gyrotron traveling-wave amplifier operating at cyclotron harmonics," *IEEE Trans. Microwave Theory Tech.,* vol. 28, pp. 313-317, 1980.

[23] N. S. Ginzburg, I. G. Zarnitsyna, and G. S. Nusinovich, "Theory of relativistic cyclotron-resonance maser amplifiers," *Radiophys. Quantum Electron.,* vol. 24, pp. 331-338, 1981.

[24] A. W. Fliflet, "Linear and nonlinear theory of the Doppler-shifted cyclotron resonance maser based on TE and TM waveguide modes, " *Int. J. Electron.,* vol. 61, pp. 1049-1080, 1986.

[25] G. S. Nusinovich, "Introduction to the physics of gyrotrons," *The John Hopkins University Press*, Baltimore and London, 2004.

[26] M. Botton, T. M. Antonsen, Jr., B. Levush, K. T. Nguyen, and A. N. Vlasov, "MAGY: A time-dependent code for simulation of slow and fast microwave sources," *IEEE Trans. Plasma. Sci.,* vol. 26, pp. 882-892, 1998.

[27] T. M. Antonsen Jr., A. A. Mondelli, B. Levush, J. P. Verboncoeur, and C. K. Birdsall, "Advances in modeling and simulation of vacuum electronic devices," *Proc. IEEE,* vol. 87, pp. 804-839, 1999.

[28] K. R. Chu, L. R. Barnett, H. Y. Chen, S. H. Chen, Ch. Wang, Y. S. Yeh, Y. C. Tsai, T. T. Yang, and T. Y. Dawn, "Stabilization of absolute instabilities in the gyrotron traveling wave amplifier," *Phys. Rev. Lett.,* vol. 74, pp. 1103-1106, 1995.

[29] K. R. Chu, H. Y. Chen, C. L. Lung, T. H. Chang, L. R. Barnett, S. H. Chen, T. T. Yang, and D. J. Dialetis, "Theory and experiment of ultrahigh-gain gyrotron traveling wave amplifier," *IEEE Trans. Plasma Sci.,* vol. 27, pp. 391-404, 1999.

[30] K. T. Nguyen, J. P. Calame, D. E. Pershing, B. G. Danly, M. Garven, B. Levush, and T. M. Antonsen, Jr., "Design of a Ka-band gyro-TWT for radar applications," *IEEE Trans. Electron Devices,* vol. 48, pp. 108-115, 2001.

[31] G. S. Nusinovich, O. V. Sinitsyn, and A. Kesar, "Linear theory of gyro-traveling-wave tubes with distributed losses," *Phys. Plasmas,* vol. 8, pp. 3427-3433, 2001.

[32] K. R. Chu, P. E. Latham, and V. L. Granatstein, "Penultimate cavity tuning of the gyroklystron amplifier," *Int. J. Electron.,* vol. 65, pp. 419-428, 1988.

[33] E. V. Zasypkin, M. A. Moiseev, E. V. Sokolov, and V. K. Yulpatov, "Effect of penultimate cavity position and tuning on three-cavity gyroklystron amplifier performance," *Int. J. Electron.,* vol. 78, pp. 423-433, 1995.

[34] G. S. Nusinovich, B. G. Danly, and B. Levush, "Gain and bandwidth in stagger-tuned gyroklystrons," *Phys. Plasmas,* vol. 4, pp. 469-478, 1997.

[35] G. S. Nusinovich, T. M. Antonsen, Jr., H. Guo, and V. L. Granatstein, "Theory of clustered-cavity gyroklystron," *Phys. Plasmas,* vol. 9, pp. 4032-4039, 2002.

[36] O. V. Sinitsyn, G. S. Nusinovich and V. L. Granatstein, "Comparison of two concepts: multi-cavity versus clustered-cavity gyroklystrons," *6-th Workshop on*

High Energy Density and High Power RF, Berkeley Springs, WV, 2003, AIP Conf, *Proc.*, vol. 691, pp. 378-385.

[37] Y. Miao, T. M. Antonsen, Jr., G. S. Nusinovich, A. N. Vlasov, H. Guo, and V. L. Granatstein, "Prebunching of electrons in harmonic-multiplying cluster-cavity gyro-amplifiers," *IEEE Trans. Plasma Sci.,* vol. 32, pp. 971-980, 2004.

[38] K. L. Felch, B. G. Danly, H. R. Jory, K. E. Kreischer, W. Lawson, B. Levush, and R. J. Temkin, "Characteristics and applications of fast-wave gyrodevices," *Proc. IEEE,* vol. 87, pp. 752-781, 1999.

[39] M. Thumm, "MW gyrotron development for fusion plasma applications," *Plasma Phys. Control. Fusion,* vol. 45, pp. A143-A161, 2003.

[40] G. S. Nusinovich, O. V. Sinitsyn, L. Velikovich, M. Yeddulla, T. M. Antonsen, Jr., A. N. Vlasov, S. R. Cauffman, and K. Felch, "Startup scenarios in high-power gyrotrons," *IEEE Trans. Plasma Sci.,* vol. 32, pp. 841-852, 2004.

[41] A. V. Gaponov, "Instability of a system of excited oscillators with respect to electromagnetic perturbations," *ZhETF*, vol. 39, pp. 326-331, 1960 (*Soviet Physics JETP,* vol. 12, pp. 232-236, Feb. 1961).

[42] V. Ya. Davydovskii, "On the possibility of accelerating charged particles by electromagnetic waves in a constant magnetic field," *Zh. Eksp. Teor. Fiz.,* vol. 13, pp. 886-888, 1962 (*Soviet Physics JETP,* vol. 16, pp. 629-630, 1963).

[43] A. A. Kolomenskii, and A. N. Lebedev, "Resonance effects associated with particle motion in a plane electromagnetic wave," *Zh. Eksp. Teor. Fiz.,* vol. 44, pp. 261-269, 1963 (*Soviet Physics JETP,* vol. 17, pp. 179-184, 1963).

[44] G. S. Nusinovich, P. E. Latham, and O. Dumbrajs, "Theory of relativistic cyclotron masers," *Phys. Rev. E,* vol. 52, pp. 998-1012, 1995.

[45] V. A. Flyagin, A. V. Gaponov, M. I. Petelin, and V. K. Yulpatov, "The gyrotron," *IEEE-MTT,* vol. 25, pp. 514-521, 1977.

[46] V. L. Bratman, N. S. Ginzburg, G. S. Nusinovich, M. I. Petelin, and P. S. Strelkov, "Relativistic gyrotrons and cyclotron autoresonance masers," *Int. J. Electron.,* vol. 51, pp. 541-568, 1981.

[47] G. S. Nusinovich and H. Li, "Large-signal theory of gyro traveling wave tubes at cyclotron harmonics," *IEEE Trans. Plasma Sci.,* vol. 20, pp. 170-175, 1992.

[48] G. S. Nusinovich and H. Li, "Theory of gyro-traveling-wave tubes at cyclotron harmonics," *Int. J. Electron,* vol. 72, pp. 895-907, 1992.

[49] G. S. Nusinovich and M. Walter, "Linear theory of multistage forward-wave amplifiers," *Phys. Rev. E,* vol. 60, pp. 4811-4822, 1999.

[50] H. R. Johnson, "Backward-wave oscillators," *Proc. IRE,* vol. 43, pp. 684-697, 1955.

[51] V. L. Bratman and M. A. Moiseev, "Conditions for self-excitation of a cyclotron-resonant maser with a non-resonant electrodynamic system," *Izv. VUZov Radiofiz.,* vol. 18, pp. 1045-1055, 1975 (*Radiophys. Quantum Electron.,* vol. 18, pp. 772-779, 1975).

[52] J. M. Wachtel and E. J. Wachtel, "Backward wave oscillation in the gyrotron," *Appl. Phys. Lett.,* vol. 37, pp. 1059-1061, 1980.

[53] V. L. Bratman, M. A. Moiseev, M. I. Petelin, and R. E. Erm, "Theory of gyrotrons with a nonfixed structure of the high-frequency field," *Izv. Vyssh. Uchebn., Zaved. Radiofiz.,* vol. 16, pp. 622-630, 1973 (*Radiophys. Quantum Electron.,* vol. 16, pp. 474-480, 1973).

[54] G. S. Nusinovich and O. Dumbrajs, "Theory of gyro-backward-wave oscillators with tapered magnetic field and waveguide cross section," *IEEE Trans. Plasma Sci.,* vol. 24, pp. 620-629, 1996.

[55] A. W. Fliflet, M. E. Read, K. R. Chu, and R. Seeley, "A self-consistent field theory for gyrotron oscillators: Application to a low Q gyromonotron," *Int. J. Electron.,* vol. 53, pp. 505-522, 1982.

[56] R. S. Symons, U. S. Patent, No. 4, 800, 322.

[57] R. S. Symons and J. R. M. Vaughan, "The linear theory of the clustered-cavity klystron," *IEEE Trans. Plasma Sci.,* vol. 22, pp. 713-718, 1994.

[58] E. V. Appleton and B. van der Pol, "On a type of oscillation-hysteresis in a simple triode generator," *Phil. Mag.,* vol. 43, p. 177, 1922.

[59] B. van der Pol, "On oscillation hysteresis in a triode generator with two degrees of freedom," *Phil. Mag.,* vol. 43, pp. 700-719, 1922.

[60] G. S. Nusinovich, "Mode interaction in gyrotrons," *Int. J. Electron.*, vol. 51, pp. 457-474, 1981.

[61] M. A. Moiseev, G. G. Rogacheva, and V. K. Yulpatov, Book of Abstracts, Session of Popov's NTORES, Gorky, U.S.S.R., p. 68, 1968.

[62] G. S. Nusinovich and R. E. Erm, "Efficiency of the CRM-monotron with a Gaussian axial distribution of the high-frequency field," *Elektronnaya Tekhnika, Ser. I, Elektronika SVCh.,* no. 8, pp. 55-60, 1972.

[63] G. S. Nusinovich, "Methods of voltage feeds for a pulsed gyromonotron which insure high efficiency in a single-mode operation," *Elektronnaya Tekhnika, Ser. I, Elektronika SVCh.,* no. 3, pp. 44-49, 1974.

[64] D. R. Whaley, M. Q. Tran, T. M. Tran, and T. M. Antonsen, Jr., "Mode competition and startup in cylindrical cavity gyrotrons using high-order operating modes," *IEEE Trans. Plasma Sci.*, vol. 22, pp. 850-860, 1994.

[65] L. A. Weinstein, General theory of resonance electron oscillators, in High-Power Electronics, Moscow, U.S.S.R., vol. 6, Nauka, pp. 84-129, 1969.

[66] W. E. Lamb, Lectures in "Quantum optics and electronics," Summer School of Theoretical Physics, Les Houches, University of Grenoble, 1964, ed. C. DeWitt, A. Blandin, and C. Cohen-Tannoudji. New York, London, and Paris: Gordon and Breach, 1965.

[67] V. E. Zapevalov and G. S. Nusinovich, "Self-modulation instability of gyrotron radiation," *Radiotekh. Electron.,* vol. 30, pp. 563-570, 1985 (*REEP*, vol. 30, pp. 101-108, 1985).

[68] T. M. Antonsen, Jr., B. Levush, and W. M. Manheimer, "Stable single mode operation in quasioptical gyrotron," *Phys. Fluids* B, vol. 2, pp. 419-426, 1990.

[69] B. Levush and T. M. Antonsen, Jr., "Mode competition and control in high-power gyrotron oscillators," *IEEE Trans. Plasma Sci.,* vol. 18, pp. 260-272, 1990.

[70] L. A. Weinstein and V. A. Solntsev, "Lectures on microwave electronics," p. 40. Moscow: "Sov. Radio," 1973.

[71] V. S. Ergakov and M. A. Moiseev, "Theory of synchronization of oscillations in a cyclotron-resonance maser monotron by an external signal," *Izv. VUZov Radiofiz.,* vol. 18, pp. 120-131, 1975 (*Radiophys. Quantum Electron.,* vol. 18, pp. 89-97, 1975).

[72] A. L. Goldenberg and M. I. Petelin, "The formation of helical electron beams in an adiabatic gun," *Izv. VUZov, Radiofiz.,* vol. 16, pp. 141-149, 1973 (*Radiophys. Quantum Electron.,* vol. 16, pp. 106-111, 1973).

[73] Sh. E. Tsimring, "Synthesis of systems for generating helical electron beams," *Radiophys. Quantum Electron.,* vol. 20, pp. 1550-1560, 1977.

[74] J. M. Baird and W. Lawson, "Magnetron injection gun (MIG) design for gyrotron applications," *Int. J. Electron.,* vol. 61, pp. 953-967, 1986.

[75] W. B. Herrmannsfeldt, SLAC Rep. 226, Stanford, CA, Nov. 1979.

[76] M. Yeddulla, G. S. Nusinovich, and T. M. Antonsen, Jr., "Start currents in the gyrotron," *Phys. Plasmas,* vol. 10, pp. 4513-4520, 2003.

[77] K. E. Kreischer and R. J. Temkin, "Single-mode operation of high-power, step-tunable gyrotron," *Phys. Rev. Lett.,* vol. 59, pp. 547-550, 1987.

[78] M. Blank, K. Felch, P. Borchard, P. Cahalan, S. R. Cauffman, T. S. Chu, and H. Jory, "Demonstration of a high-power long-pulse 140-GHz gyrotron oscillator," *IEEE Trans. Plasma Sci.,* vol.32, pp. 867-876, 2004.

[79] K. M. Felch, M. Blank, P. Borchard, et. al, "Progress update on CPI 500 kW and 1 MW, multi-second-pulsed gyrotorns," 3rd Int. Conf. IVEC-2002, pp. 332-333, April 23-25, 2002, Monterey, CA.

[80] M. Yeddulla, G. S. Nusinovich, A. N. Vlasov, T. M. Antonsen, Jr., K. Felch, and S. Cauffman, "Startup scenario in a 140 GHz gyrotron," in *Proc. 27th Int. Conf. Infrared Millimeter Waves*, R. J. Temkin, Ed., San Diego, CA, Sept. 22-26, 2002, pp. 9-10.

[81] O. V. Sinitsyn, G. S. Nusinovich, A. N. Vlasov, et. al., *2005 IEEE Int. Conf. on Plasma Sci., IEEE Conference Record-Abstracts*, June 20-23, 2005, Monterey, CA, paper 2X3, p. 111.

[82] G. Dammertz, S. Alberti, A. Arnold et al., "Experimental results on the 140 GHz, 1 MW, CW gyrotrons for the stellarator W7-X," *The Joint 30th Int. Conf. on Infrared and Millimeter Waves & 13th Int. Conf. on Terahertz Electronics*, Sept. 19-23, 2005, Williamsburg, VA, Conf. Digest, vol. 1, paper TA4-2, p. 235.

[83] A. Kasugai, R. Minami, K. Takahashi et al., "Development of a 170 GHz high-power and CW gyrotron for fusion application," *The Joint 30th Int. Conf. on Infrared and Millimeter Waves & 13th Int. Conf. on Terahertz Electronics*, Sept. 19-23, 2005, Williamsburg, VA, Conf. Digest, vol. 1, paper TB4-1, p. 287.

[84] G. Dammertz, O. Braz, C. T. Iatrou et al., *20th Int. Conf. on Infrared and Millimeter waves*, Dec. 11-14, 1995, Orlando, Fl., Conf. Digest, Ed. R. J. Temkin, paper T8.9, p. 285.

[85] B. Piosczyk, *15th Int. Conf. on Infrared and Millimeter Waves*, Dec. 10-14, 1990, Orlando, Fl., Conf. Digest, Ed. R. J. Temkin, SPIE vol. 1514, paper W8.3, p. 499.

[86] J. Felch, H. Huey, and. H. Jory, *J. Fusion Energy*, 9, 59, 1990.

[87] D. Dialetis and K. R. Chu, Ch. 10 in "Infrared and Millimeter Waves," vol. 7, part II, Ed. K. J. Button, Academic Press, New York, 1983.